InGaAsP/GaAs QUANTUM WELL LASERS: MATERIAL PROPERTIES, LASER DESIGN AND FABRICATION, ULTRASHORT-PULSE EXTERNAL-CAVITY OPERATION

By

STEVEN GERALD WALLACE, B.Sc., M.Eng.

A Thesis

Submitted to the School of Graduate Studies

in Partial Fulfillment of the Requirements

for the Degree

Doctor of Philosophy.

McMaster University

DOCTOR OF PHILOSOPHY (2001)
(Engineering Physics)

McMaster University
Hamilton, Ontario

TITLE: InGaAsP/GaAs Quantum Well Lasers: Material Properties, Laser Design and Fabrication, Ultrashort-Pulse External-Cavity Operation

AUTHOR: Steven G. Wallace, B.Sc. (Laurentian University)
M. Eng (McMaster University)

SUPERVISORS: Dr. H.K. Haugen and Dr. P. Mascher

NUMBER OF PAGES: xii, 177

Abstract

A detailed characterization of the $In_{1-x}Ga_xAs_yP_{1-y}$ quaternary material system lattice matched to GaAs, grown by gas source Molecular Beam Epitixy (MBE) has been performed. Photoluminescence, X-ray diffraction and Transmission Electron Microscopy (TEM) were used to study the lateral composition modulation (LCM) which was observed in this material system. Optimization of the growth process and the substrate orientation resulted in a significant reduction of the LCM. Additionally, a comprehensive analysis of the optical constants was performed which resulted in the first publication of wavelength and composition dependent index of refraction data for this material system. The combination of growth optimization and index of refraction data lead to the demonstration of efficient, low threshold operation of InGaAsP/GaAs based multiple quantum well lasers.

In order to efficiently couple the above laser diodes to an external cavity to facilitate the generation of ultrashort pulses, antireflection facet coatings were required. As such, optical interference filters have been fabricated using a plasma enhanced chemical vapor deposition system, based on the SiO_xN_y material system. High quality antireflection facet coatings, suitable for application to the InGaAsP/GaAs diode lasers have been designed and fabricated, resulting in modal reflectivities of 1-2$\times 10^{-4}$.

Finally, an ultrashort-pulse external-cavity diode laser system was designed and manufactured which allowed the laser diode to be wavelength tuned and emit mode-locked ultrashort optical pulses. Pulses with sub 2 ps duration and greater than 1 mW average output power have been achieved. A study of the novel application of an asymmetric quantum well structure to the generation of ultrashort optical pulses has been proposed and initiated.

Acknowledgements

I would like to thank my supervisors, Harold Haugen and Peter Mascher, for their support and encouragement during this thesis work. I am grateful for the trust they have shown in me, and the research freedom they have allowed.

I am also grateful for the MBE support of Scott McMaster, who performed all of the growths described in this thesis, and Brad Robinson, who was always available for technical discussions regarding MBE. Initial development of the ECR-PEVCD system was done by Marcel Boudreau, and I thank him for the instruction and support he provided during the first year of this thesis project. I would also like to thank Mike Brennan for his valued input to the short pulse work over the last two years and particularly for the data analysis and hardware control software. Thanks must go to the entire faculty, staff and students of the engineering physics department, for creating and maintaining an excellent environment for both personal and professional development.

Thanks is also due to Dan Dalacu and Ludvik Martinu, of the Ecole Polytechnique, Montreal, for allowing me access to their spectroscopic ellipsometer.

I must also thank my parents Bev and Gerry Wallace, for the over 29 years of support, encouragement and faith. Without their assistance, I would not have had the opportunity to pursue a higher education.

Finally, I would like to thank my wife, Dana, for the love and encouragement she has provided me with. She and our three children, Cameron, Connor and McKenna, have given my the inspiration and motivation to complete this thesis work. For that, I am forever grateful.

Contents

List of Figures

List of Tables

Chapter 1

Introduction

Since the first demonstration of laser action in a semiconductor pn junction in 1962 [1-4], diode lasers have been a topic of consistent and intense research. In the almost four decades since, many advances have been made, from improvements in design principles and operating characteristics, to the development of new materials from which a broad range of wavelengths can be achieved.

In recent years, many of the advancements in the field of diode lasers have been driven by the telecommunications industry as a result of its astonishing growth. Most of this research and development has been focussed on two different wavelength ranges. The first corresponds to that in the vicinity of 1.55 μm, which is used to transmit an optical signal along a fibre. The other wavelength range of interest is that in the vicinity of 980 nm (0.98 μm). This wavelength has become extremely important since the advent of the erbium-doped fibre amplifier. This type of fibre, when pumped with light at 980 nm, is able to amplify signals around 1.55 μm, which has greatly improved the capabilities of current telecommunication systems.

In more recent years, other applications have emerged for diode lasers, many of which have not yet reached a commercial level. The work to be described in this thesis has been driven by potential new applications of diode lasers which operate in the near-infrared (800-1000 nm), based on the InGaAsP material system, grown lattice matched to GaAs. Of

particular interest is the design, operation and optimization of such lasers when operated in a regime where they emit ultrashort optical pulses. The mechanism by which the ultrashort optical pulses are generated is known as mode-locking.

One of the more exciting applications for mode-locked diode lasers operating in the near IR wavelength range is that of two-photon fluorescence (TPF) microscopy. In recent years, this technique has been studied as a replacement for more mature techniques which rely on 'standard' fluorescence. Standard fluorescence refers to the process by which a single 'pump' photon excites a transition within the fluorescent material (molecule). When the excited molecule returns to its ground state, a photon is emitted with an energy slightly less than that of the energy of the absorbed pump photon. This is the fluorescence process. In the case of two-photon induced fluorescence (TPIF, or more simply TPF), the pump photon's energy is approximately equal to half of that of the 'standard' fluorescence pump photon. Therefore, the simultaneous absorption of two photons is required to excite the molecule, in order to generate a fluorescent signal. As a result of the second order nature of this process, ultrashort optical pulses, which have a very high instantaneous intensity, are required.

Most investigations into TPF microscopy have utilized Titanium:sapphire lasers, partly as a result of their commercial availability. Although such systems can readily produce 100 fs pulses with high average powers, they are relatively expensive and complex. As such, a compact and inexpensive lower power source of ultrashort optical pulses is desirable. In this thesis, the design of an ultrashort pulse laser system which may become suitable for this application, as well as numerous others, will be described.

As a result of the desire to use a range of different fluorescent materials, more commonly referred to as fluorophores, tunability of the pulse wavelength is also desirable, to maximize the efficiency of the fluorescence generation.

In this thesis, the development of an ultrashort-pulsed external-cavity quantum well laser system is discussed. All aspects of the system development, from the semiconductor laser material characterization and optimization, to the final implementation of the external cavity diode laser are described. The development approach is outlined in the flow chart in Fig. 1.1

As a result of the many applications for short optical pulses, such as two-photon fluorescence microscopy, as well as other emerging biological techniques, **the motivation of this work was to design, fabricate and characterize an ultrashort-pulsed external-cavity diode laser system,** suitable for such applications.

From the perspective outlined above, the work contained in this thesis can be separated into three individual core areas.

- InGaAsP/GaAs: Material characterization and laser fabrication.
- Antireflection Facet Coatings: Design and fabrication
- Short-pulse External-cavity Diode Lasers: Design and operation.

InGaAsP/GaAs: Material characterization and laser fabrication

Operating wavelengths in the vicinity of 800-1000 nm are desired in order to make use of the most common and most useful fluorophores available for two-photon fluorescence microscopy. The McMaster gas source molecular beam epitaxy (GSMBE) is able to provide indium (In), gallium (Ga), arsenic (As) and phosphorus (P) (as well as Si and Be which are used as dopants). As a result, the quaternary system containing the above four elements was utilized in the production of the diode lasers. $In_{1-x}Ga_xAs_yP_{1-y}$ can be grown lattice matched to both InP and GaAs, by appropriately varying x and y. The InGaAsP/InP system has been intensely studied for a number of years as it is the system on which most of the current telecommunication semiconductor components are based. However, since the

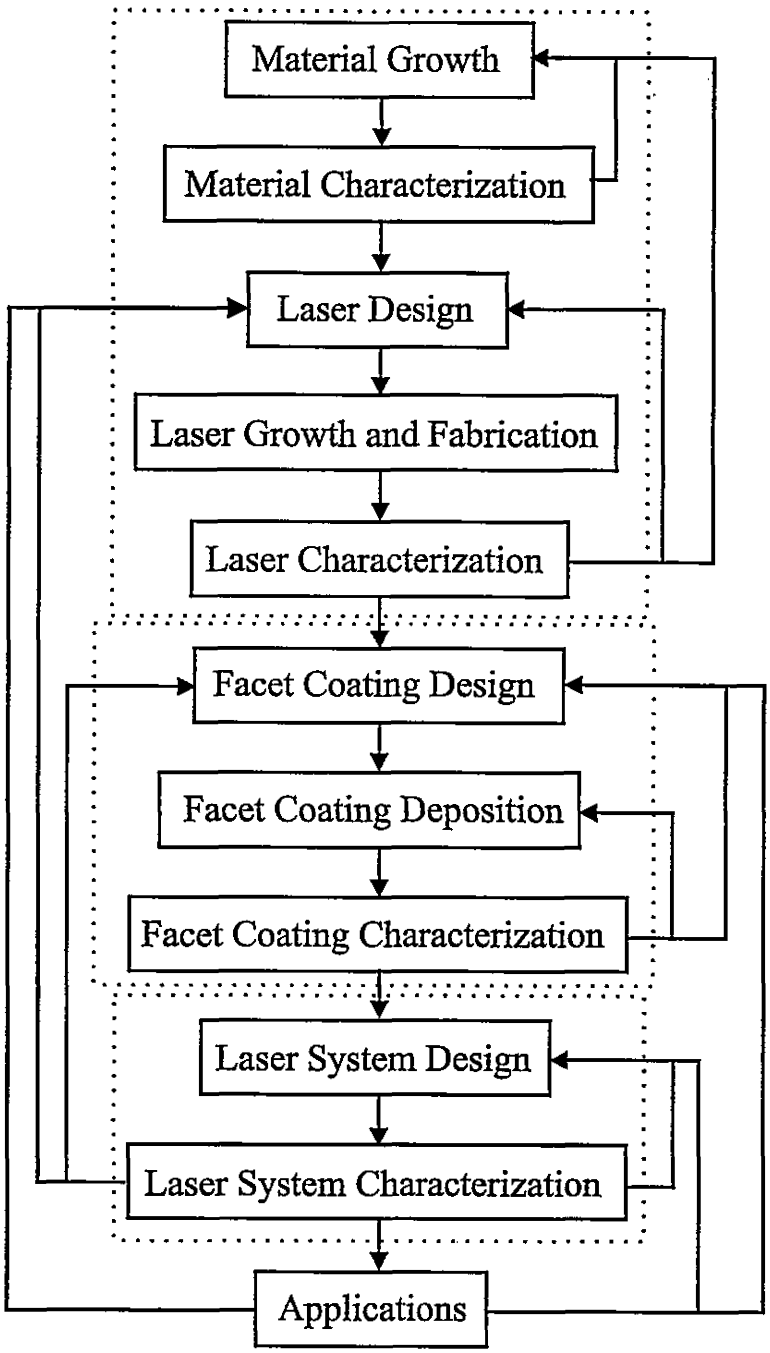

Figure 1.1: Engineering approach flow chart.

wavelength range of interest is outside of that available from InGaAsP/InP, the InGaAsP was instead grown lattice matched to GaAs. Band-gaps ranging from approximately 1.9 eV to 1.4 eV are available with the InGaAsP/GaAs system.

The InGaAsP/GaAs material system has not been studied in the same detail as the InGaAsP/InP material system, and thus optimization of the growth process was necessary in order to make fabrication of these diode lasers possible. In Chapter 2, the growth of InGaAsP by MBE will be described and a characterization of a lateral composition modulation (LCM) which was observed in this system, will be provided. For our applications this effect is undesirable, and investigations have been conducted with the goal of reducing its severity. A number of different techniques were explored and the potentials of each will be discussed.

Due to the fact that the InGaAsP/GaAs system has not been studied in great detail, experimental data on the index of refraction was not available. Thus, a complete study of the optical properties of InGaAsP/GaAs over the full composition range has been performed by variable angle spectroscopic ellipsometry, which is presented in Chapter 4. The optical constants were determined from 300 nm to 1600 nm, with particular emphasis on the wavelength range relevant to the operation of InGaAsP/GaAs based diode lasers. From this analysis, a semi-universal index of refraction relationship was established, which allows the index of refraction to be determined for an arbitrary material band-gap at any wavelength where the material is transparent.

The efficient design of a laser diode requires a knowledge of the index of refraction of the materials that make up the laser, at the wavelength at which the laser operates. Additionally, the design of an antireflection facet coating requires a characterization of the waveguide properties, and hence, requires this index of refraction data. For the above reasons, a full analysis of the previously uncharacterized index of refraction of InGaAsP/GaAs

was performed.

Antireflection Facet Coatings: Design and fabrication

In an external cavity configuration, feedback of the optical output of the diode laser is provided by an external optical element. Effective coupling of the solitary diode laser chip to the external cavity is achieved through the application of a high quality antireflection coating to at least one of the laser facets. This coating reduces the strength of the feedback within the laser chips itself and increases the coupling efficiency from the external element back into the diode laser cavity. This allows the laser to be operated in a manner that would not be accessible without the antireflection coating.

From the discussion above, it is clear that part of the work described in this thesis was devoted to the design and fabrication of antireflection facet coatings. These coatings are formed through the decomposition of SiH_4 in an electron cyclotron resonance plasma enhanced chemical vapour deposition system (ECR-PECVD). In Chapters 3 and 6 the deposition technique and the antireflection facet coating design procedure, respectively, will be outlined. In Chapter 6, the waveguide parameters of the laser diode on which the coating is deposited, and the required modifications to the coating to achieve the desired reflectivity profile, will be discussed.

Short-pulse External-cavity Diode Lasers: Design and operation

Once the growth process for the laser materials has been optimized, and diode lasers have been designed (based on the experimentally determined indices) and antireflection coated (based on the measured indices of the dielectrics and semiconductors), the key component of the external cavity mode-locked diode laser can be obtained. The remaining focus of this thesis is the design and optimization of the laser system, not only from the perspective of feedback to the other two core areas, but also with respect to the optimal operating conditions and configuration of the laser system.

In Chapter 7, the experimental results from a variety of mode-locking experiments will be described, and the application of such a system to TPF microscopy will be discussed. A number of exciting new initiatives have been explored, which indicate that a novel application of asymmetric quantum wells [1] may provide distinct advantages to a 'standard' quantum well structure, particularly from the perspective of versatility related to the application of two-photon fluorescence microscopy.

Finally, some insight into the direction in which this research should continue will be provided in Chapter 8, as well as a summary of the results contained within this thesis.

1.1 Project Contributors

The development of optoelectronic components and systems requires the use of an immense array of design, fabrication, and test and characterization tools. Since the successes outlined within this thesis were achieved within a collaborative environment, the contributions of others to these achievements must be identified.

- A characterization of InGaAsP grown lattice matched to GaAs was conducted, and optimization of the growth parameters was performed, with particular attention to the lateral composition modulation that was observed. All of the above MBE growths were performed by Scott McMaster, under the supervision of Brad Robinson. Brad also provided technical input on the growth optimization process as well as the vicinal substrate investigation. All TEM sample analysis was performed by A. Perovic, with sample preparation by Andy Duft.

- A full characterization of the optical constants of InGaAsP as a function of wavelength was conducted by the author at the Ecole Polytechnique Montreal. Initial setup and operation of the variable angle spectroscopic ellipsometer was demonstrated by Dan

[1] An asymmetric quantum well structure contains at least two wells with different transition energies.

Dalacu. Access to the ellipsometer was provided by Ludvik Martinu.

- Multiple quantum well diode lasers operating in the range of 800-1000 nm were designed, fabricated and characterized. Susan Nagy is credited with training the author in the processing of ridge waveguide lasers. James Roscoe and Mike Brennan are credited with writing the data acquisition and hardware control software used in some of the characterization of the above diode lasers.

- Practical state of the art antireflection facet coatings were designed and fabricated for the diode lasers described above. Process control and development on the ECR-PECVD system was performed to allow the fabrication of high quality antireflection and high reflectance facet coatings. Initial work on the development of the ECR system was performed by Marcel Boudreau, who also provided some technical input to system modifications and development performed by the author. The original modal reflectivity calculator was also written by Marcel.

- A versatile and compact external cavity laser system utilizing the InGaAsP/GaAs based diode lasers was developed to provide both wavelength tunability and ultrashort pulse generation. Pulses as short as 2 ps, with average output powers of 1 mW were generated and characterized. An investigation into the novel application of asymmetric quantum well structures to the generation of ultrashort pulses has been initiated, and a non-standard laser structure designed to improve 'access' to the enhanced gain bandwidth of the asymmetric quantum well structure has been proposed. Andrzej Borowiec was instrumental in the design and assembly of the autocorrelator used to characterize the ultrashort pulses. Mike Brennan has worked closely with the author on the recent advancements of the short pulse system, and he has contributed to this project through his daily involvement. He is currently continuing this work as his PhD research project.

Chapter 2

InGaAsP: Growth and Characterization

To design and fabricate efficient diode lasers to be used to generate ultrashort optical pulses, the growth of InGaAsP lattice matched to GaAs was studied, and the growth parameters where optimized. In this chapter, Molecular Beam Epitaxy (MBE) growth of InGaAsP/GaAs will be described, and the results of a characterization of this material system will be provided.

2.1 MBE of III-V Compound Semiconductors

Molecular beam epitaxy is an ultra high vacuum deposition technique whereby atomic or molecular beams, impinging on a heated substrate, react to form epitaxial layers. In gas source MBE (GSMBE), which was used to produce all of the materials described here, the group V species are supplied by thermal cracking of the hydrides, arsine (AsH_3) and phosphine (PH_3), which results in the formation of As_2, P_2 and H_2. The flux of group III species (as well as the dopants) are provided by heating effusion cells containing a molten charge of indium and gallium. By controlling the flow of the gases and the temperature of the cells, precise control of the layer composition and thickness is achieved.[1]

Since the mean free path of the atoms or molecules in the beam is larger than

[1] A detailed description of molecular beam epitaxy can be found in [5].

the cell to substrate distance, the reaction of species in the gas phase does not occur. Therefore, surface chemical reactions are responsible for the formation of the epitaxial layers. Impinging In and Ga atoms stick to the substrate surface due to their low vapor pressures at typical growth temperatures (500 °C), where they are available to react with the arriving group V species. In the absence of surface group III elements, the sticking coefficient for arriving group V elements is zero. Alternatively, the sticking coefficient becomes nearly unity on a surface whose group III coverage is complete. Therefore, the growth rate is determined by the arrival rate of group III elements, provided a sufficient flux of group V elements is supplied. In this way, an overpressure of group V elements is normally provided to ensure complete reaction of the surface group III elements.

Prior to incorporation into the epitaxial layer via chemisorption, the surface species exist in a weakly bound physisorbed state, provided by the Van der Waals interaction with the surface. In this state, the surface species are relatively mobile, with a binding energy on the order of 0.25 eV, which is low in comparison to a binding energy of 1-5 eV for the chemisorbed state. For normal growth conditions, this implies that diffusion at the growing surface is dominant, whereas bulk diffusion can normally be neglected. This aspect of MBE will be shown to be very important.

2.2 InGaAsP/GaAs: Growth and Characterization

In this section, the growth and characterization of InGaAsP lattice matched to GaAs will be discussed. In particular, the observation of a strong lateral composition modulation (LCM) will be provided, and the mechanisms by which it can be reduced, will be outlined.

Lateral Composition Modulation

The quaternary material, $In_{1-x}Ga_xAs_yP_{1-y}$, can be viewed as an alloy of the four compounds, InAs, GaAs, InP, and GaP, and as such, many of its characteristics can be modeled

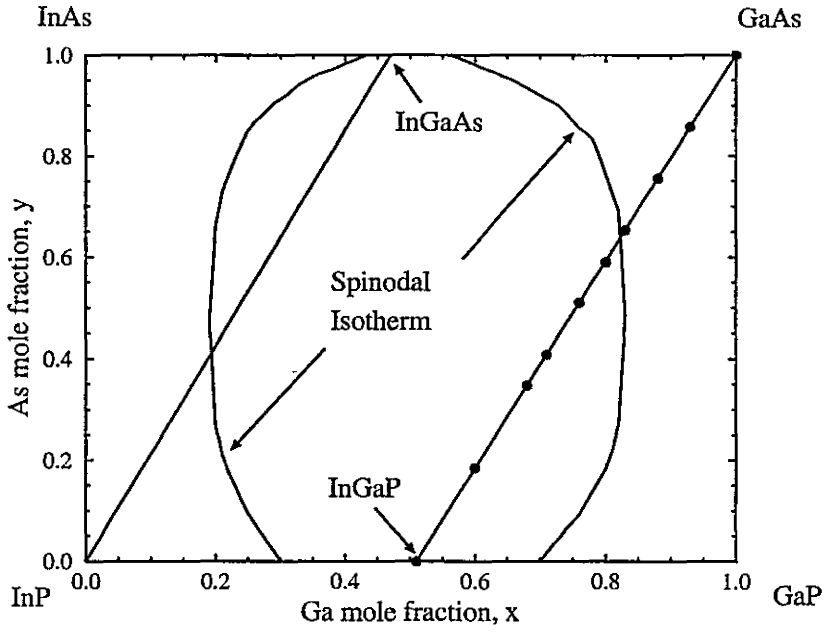

Figure 2.1: Spinodal isotherm

from a treatment of the binaries. This quaternary material may be grown lattice matched to either InP or GaAs, by changing the compositions x and y, while maintaining a fixed relationship between the two. In Fig. 2.1, the approximate compositions required to achieve lattice matching to InP and GaAs are provided. The line extending from InP diagonally to InGaAs (x$\sim$0.5) corresponds to those compositions lattice matched to InP. Similarly, InGaAsP compositions lattice matched to GaAs are approximately given by the line extending from GaAs to InGaP (x$\sim$0.5).

Growth of this quaternary on both InP and GaAs, however, is problematic as a result of a miscibility gap which exists for a certain range of compositions. Such compositions are energetically unstable, the effect of which is to form alternating regions which are InAs and GaP rich. The compositions for which this lateral composition modulation (LCM) is expected to occur can be predicted by the spinodal isotherm, which can be calculated by a thermodynamic treatment of the alloy [6]. This isotherm is illustrated in Fig. 2.1

for a growth temperature of 480 °C. LCM is expected to occur for compositions inside the isotherm.

Thermodynamically, the alloy can be described by consideration of the four binaries from which it is formed. Mathematically, the surface free energy, F, can be written as

$$F = H - TS \tag{2.1}$$

where H is known as the enthalpy of mixing, and TS is the product of the growth temperature and the entropy, which collectively is referred to as the entropy of mixing. Two different approaches have been described to evaluate the enthalpy of mixing, namely the strictly regular solution approximation model [6, 7] and the delta lattice parameter model [8]. In the first model, the enthalpy is calculated from interaction parameters based on bulk chemical potentials of the four binaries. In the latter model, the difference in the lattice constants, which are provided in Table 2.1, and the associated strain energies, are used to

Compound	$a[\AA]$
GaP	5.4506
GaAs	5.6535
InP	5.8688
InAs	6.0584

Table 2.1: Binary lattice constants.

determine the enthalpy of mixing.

When the surface free energy can be reduced by a deviation in the local composition from that of a homogeneous alloy, phase separation will occur. The spinodal isotherm represents the boundary between compositions for which phase separation is favored, and those for which it is not, for a given growth temperature. This isotherm is effective in predicting the compositions for which phase separation occurs.

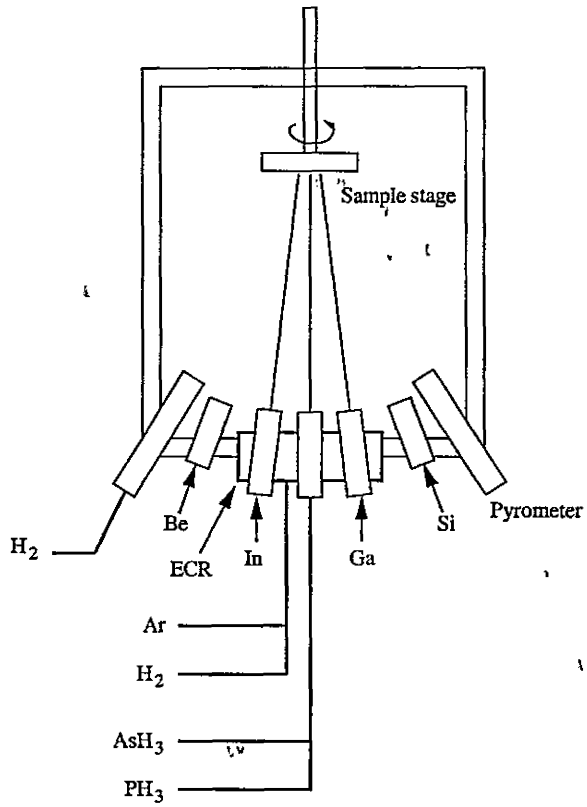

Figure 2.2: McMaster GSMBE system.

2.2.1 The McMaster GSMBE System

A schematic of the GSMBE system used to produce the epitaxial layers discussed in this thesis is given in Fig. 2.2. The deposition chamber is made of stainless steel and is pumped with a high capacity diffusion pump through a cold trap, capable of achieving base pressures of approximately 10^{-10} Torr. Liquid nitrogen cooled baffles provide isolation between the individual effusion cells. Panels within the chamber are also cooled with liquid nitrogen to reduce outgassing and to provide additional contaminant reduction. A standard load-lock provides for short sample loading times while maintaining the ultra high vacuum conditions.

Prior to being transferred to the deposition chamber, substrates are degassed at 450 °C for approximately 30 minutes. The native oxide on the substrate surface is removed by exposing the surface to an ECR (Electron Cyclotron Resonance) hydrogen plasma gen-

erated by 200 Watts of microwave power in the presence of a group V (As) overpressure, to maintain proper surface stoichiometry. The surface temperature is monitored throughout all processes by an infrared pyrometer.

2.2.2 Characterization Techniques

Numerous techniques are used to characterize the epitaxial layers, some of which are standard and routine, while others are more specialized, and are applied only to specific samples.

Photoluminescence

Photoluminescence (PL) is a standard non-destructive technique whereby the band-gap of direct gap semiconductors can easily be determined. In this thesis, the band-gap, E_g, is defined as the peak in the PL spectrum. This definition of band-gap requires further discussion. From a theoretical perspective, the band-gap does not correspond to the peak in the PL spectra, but rather to a slightly smaller energy. To accurately determine this band-gap from the PL spectra, a theoretical curve would need to be fit, from which the band-gap could be extracted. Due to the complexity of the PL spectra as a result of the lateral composition modulation, such a curve fit is impractical. The true theoretical band-gap, which refers to the difference in energy between the lowest energy level in the conduction band and the highest energy in the valence band, will be referred to in this thesis as the fundamental gap, and will be denoted by E_0. A similar convention has been adopted by other semiconductor laboratories.

The experimental system used to measure the PL is illustrated in Fig. 2.3. The absorption of the 488 nm photons from the argon-ion laser, generates electron-hole pairs within the semiconductor sample. These electron hole pairs thermalize, and as such, occupy the lowest energy states available, which in the case of bulk samples, corresponds to band edge states. In a quantum well, the carriers will occupy the lowest allowed energy level within the well. The recombination of the electron hole pair will produce a photon of

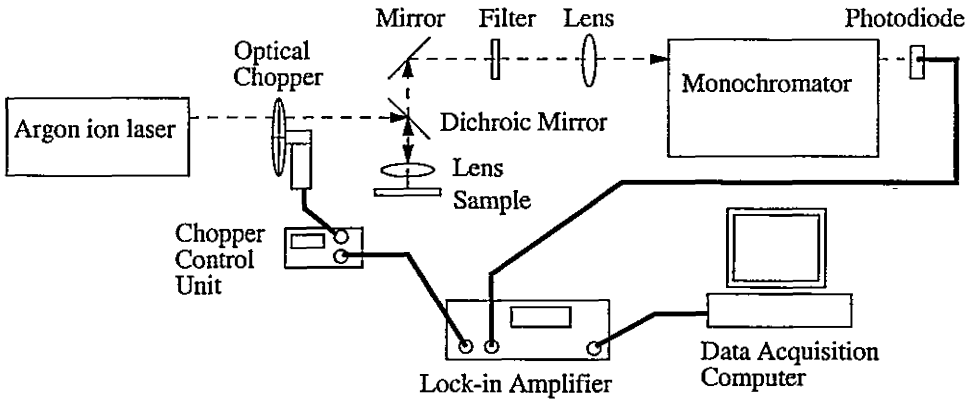

Figure 2.3: Photoluminescence system.

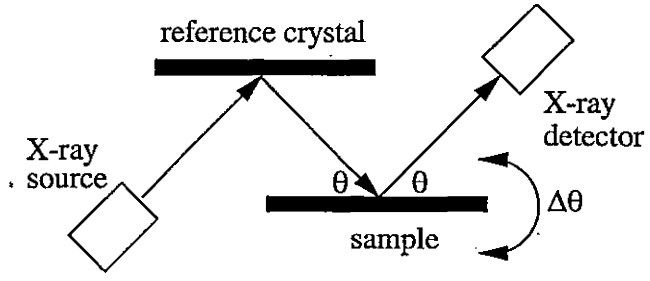

Figure 2.4: Schematic of the X-ray diffraction system.

energy equal to the difference of the energy levels of the electron and hole in the conduction and valence bands respectively. PL wavelength, intensity and linewidth are routinely used to characterize the semiconductor layers.

X-ray Diffraction

X-ray diffraction is another technique which is routinely used to characterize the MBE grown material. The system used in this work is a Bede Scientific Instruments QC1 double-crystal diffractometer, utilizing the 004 reflection. Figure 2.4 illustrates the basic configuration of the X-ray diffraction system. A highly monochromatic beam of X-rays is incident on the sample at approximately the Bragg angle. The sample is then tilted, or 'rocked' through the Bragg angle, producing the rocking curve, as illustrated in Fig. 2.5. As the sample is tilted, the Bragg condition will be satisfied for the lattice constant associated with the substrate

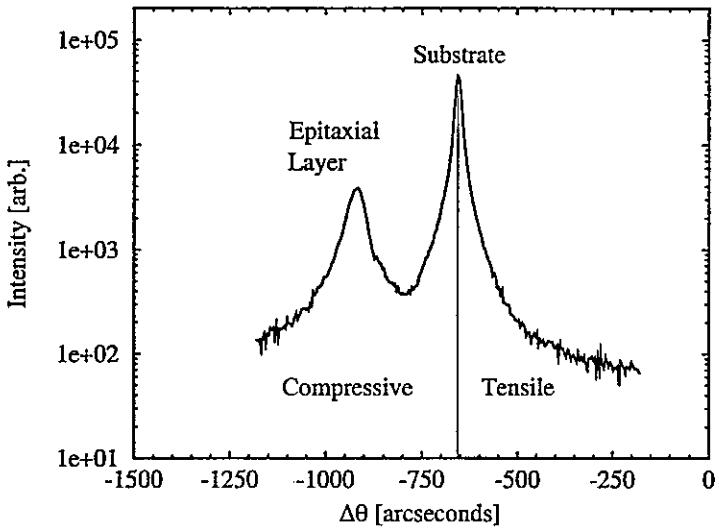

Figure 2.5: Typical X-ray rocking curve of an approximately lattice matched epitaxial layer on GaAs.

and with the epitaxial layer. The separation, in arc-seconds, of the peaks originating from the substrate and epi-layer is easily converted into Δa, which is the difference in the lattice constants, perpendicular to the sample surface.

From the combination of X-ray and PL analysis, the sample composition can be determined provided a relationship between band-gap and composition, and lattice constant and composition, is available. For InGaAsP lattice matched to InP, numerous relationships have been obtained from experimental data, and are available in the literature. However, for the quaternary lattice matched to GaAs, such a full and rigorous set of experimental data does not exist, making a compositional determination from X-ray and PL measurements difficult. A compilation of the limited experimental data that is available [9] has been used to relate the band-gap to the As content (y) for quaternaries ($In_{1-x}Ga_xAs_yP_{1-y}$) lattice matched to GaAs. A polynomial fit was applied to the y versus E_g data, yielding the expression in Eq. 2.2, from which Eq. 2.3 was derived. This band-gap arsenic concentration

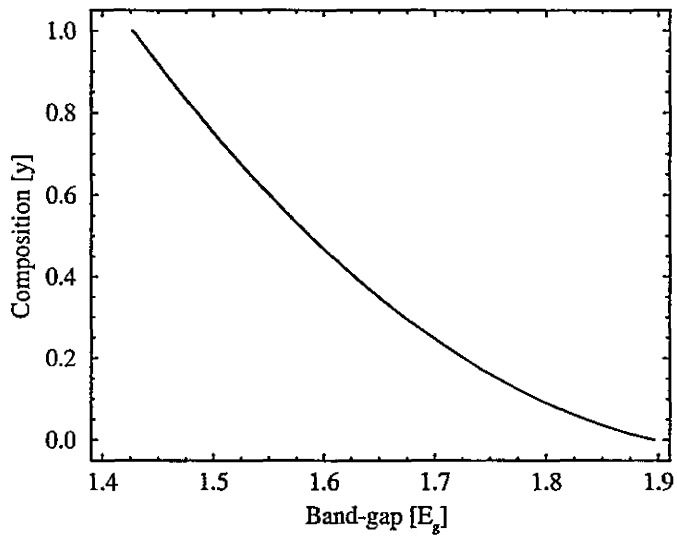

Figure 2.6: Graphical representation of the band-gap composition (y) relationship.

relationship is plotted in Fig. 2.6.

$$y = 12.689 - 12.752E_g + 3.196E_g^2 \tag{2.2}$$

$$E_g = 1.995 - \sqrt{0.3129y + 9.724 \times 10^{-3}} \tag{2.3}$$

The relationship relating x and y to obtain lattice matching to GaAs is provided in Eq. 2.4 [9].

$$x = \frac{0.215 + 0.192y}{0.415 - 0.013y} \tag{2.4}$$

The above relationships are intended to be used only as a rough guide to relate the band-gap to composition for InGaAsP lattice matched to GaAs.

Transmission Electron Microscopy

Cross-sectional TEM is a very sensitive technique that can be used to study the crystallography of semiconductor samples. For extensive details regarding the TEM analysis of

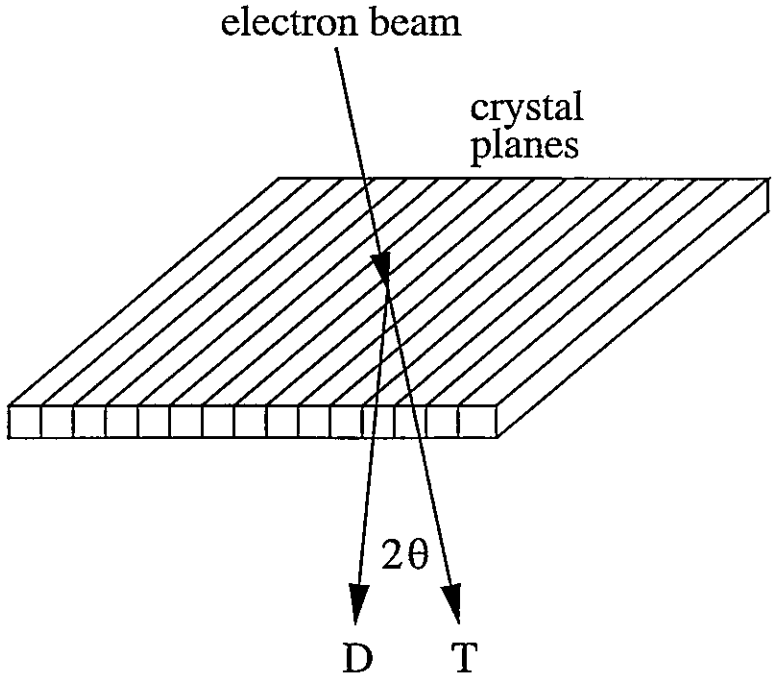

Figure 2.7: Schematic of TEM diffraction.

LCM, as well as more general aspects of TEM, the interested reader should refer to the work of R.R. Lapierre [10, 11] and the text by Williams and Carter [12] respectively. The samples were mechanically polished and subsequently thinned to approximately 2000 Å by an ion milling apparatus. The TEM system used in this research was a Phillips CM12 TEM, operating at 120 keV.

In TEM, a diffraction pattern and a corresponding image can be obtained by appropriate orientation of the incident beam and the detector with respect to the sample crystallographic axis. A schematic illustrating the transmitted and diffracted electron beams upon interaction with a crystal sample is provided for reference in Fig. 2.7. As has been described in detail previously [10], LCM in InGaAsP is best observed under two beam conditions along the $[0\bar{1}1]$ direction using diffraction vectors of g = 022 and g = 400. Under these conditions, the lateral composition modulation is seen as bright and dark contrast in the TEM image. This differentiation is a direct result of the strain fields associated with

the InAs-rich and GaP-rich regions, which relax at the foil surface.

Atomic Force Microscopy (AFM)

AFM is a technique which can be used to study the surface of relatively smooth samples. A small cantilever, whose deviation from a predetermined reference level is monitored by the simultaneous deflection of a laser beam incident on the cantilever surface, is allowed to interact with the sample surface as it passes below the cantilever. Depending on the mode of operation, the cantilever is either in direct physical contact with the sample, which is appropriately known as contact mode, or is maintained at a slight distance from the sample, where the cantilever position oscillates as a result of Van der Waals interaction between the surface and the cantilever. This latter mode of operation, which was used in all AFM analysis discussed here, is known as tapping mode.

Variable Angle Spectroscopic Ellipsometry

Variable angle spectroscopic ellipsometry is an extremely powerful technique for determining the optical constants of a wide range of materials, and in particular, for semiconductors. Ellipsometry, which is a well established technique, measures the change in the state of polarization of a monochromatic beam of light upon reflection from the surface of a sample.

The ratio of the two Fresnel reflection coefficients for p and s polarized light is given by ρ

$$\rho = \frac{R_p}{R_s} = \frac{|R_p|}{|R_s|} e^{i(\delta_p - \delta_s)} = \tan(\psi) e^{i\Delta} \tag{2.5}$$

Equation 2.5 is the fundamental equation of ellipsometry, and Δ and ψ are known as the ellipsometric angles. Chapter 4 contains a more detailed discussion of ellipsometry, and the analysis of semiconductor samples.

2.3 InGaAsP/GaAs: Experimental Results

In this section, the experimental details of the growth of InGaAsP will be provided, as well as a characterization of this material, based on photoluminescence (PL), X-ray diffraction, atomic force microscopy (AFM) and cross-sectional transmission electron microscopy (TEM) measurements.

The quality of the quaternary layers, as evaluated by PL, AFM, X-ray diffraction and cross-sectional TEM, is a strong function of both the growth temperature and the composition of the epitaxial layer. For compositions of InGaAsP with band-gaps in the vicinity of 1.75 eV (x=0.55 to 0.75) a significant increase in the PL linewidth was observed, in agreement with the phase separation model discussed previously.

2.3.1 Composition

The composition (x,y) of $In_{1-x}Ga_xAs_yP_{1-y}$ grown lattice matched to GaAs can be varied from GaAs to $In_{0.48}Ga_{0.52}P$. As mentioned above, over a certain range of compositions between the two end points, lateral composition modulation (LCM) occurs, which manifests itself as a broadening of the photoluminescence linewidth. Assuming only a deviation in the group III composition, the maximum range of the composition modulation is estimated to be $\Delta x = \pm 0.01$, for growths at 480 °C. For higher growth temperatures, this deviation in composition is substantially larger.

Photoluminescence

A series of lattice matched samples ranging in composition from GaAs to $In_{0.48}Ga_{0.52}P$ (InGaP) were grown at a temperature of 480 °C. These growths allowed an analysis of the films as a function of composition, as well as providing a useful calibration for future growths of laser structures utilizing these materials.

The sample structures grown for the purpose of PL analysis consisted of 3000 Å of

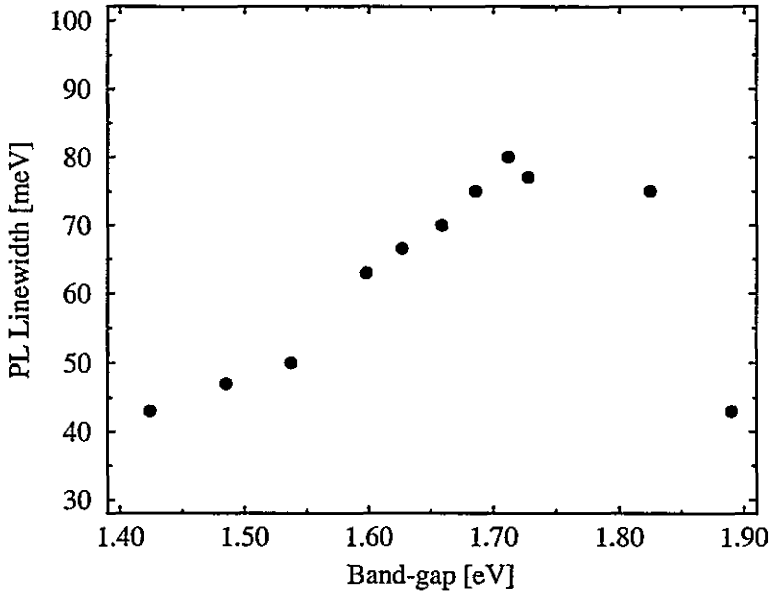

Figure 2.8: Photoluminescence linewidths as a function of material band-gap.

the quaternary layer surrounded by 250 Å InGaP layers, all of which were deposited on a 2000 Å GaAs buffer layer, on n-type [100] GaAs. The measured PL linewidths are plotted in Fig. 2.8 as a function of the samples band-gap. (Recall that the band-gap here is defined as the peak in the PL spectrum.) As is clearly illustrated in this figure, the PL linewidth is a function of the composition of the quaternary layer, with increased linewidths in the range from x=0.53 to x=0.75 (E_g=1.85 to 1.6 eV). As was illustrated in Fig. 2.1, this composition range lies within the spinodal isotherm, indicating that LCM should occur. Compositions which lie deeper within this isotherm will experience a stronger driving force towards phase separation. This would result in a larger composition difference between the InAs-rich regions and the GaP-rich regions, which would produce a larger PL linewidth. From the above, a strong correlation is observed between the compositions for which lateral composition modulation should be most severe, and the extent of the resultant linewidth broadening.

From the perspective of laser design, information regarding the compositions for which LCM occurs is very useful, allowing the designer the ability to avoid compositions for which the LCM is most severe, since it has been shown that LCM can negatively influence the performance of diode lasers [13, 14].

2.3.2 Effect of Growth Temperature

A number of InGaAsP samples were prepared at temperatures ranging from 460 °C to 525 °C in order to investigate the impact of growth temperature on the resultant film quality. Photoluminescence and X-ray diffraction were used to evaluate the films, and the observed characteristics could be related to the lateral composition modulation.

In general, a decrease in growth temperature was found to result in a reduction in lateral composition modulation, as was indicated by PL, X-ray and TEM measurements. It was also observed that the general trend of the PL linewidth as a function of composition, provided in Fig. 2.8, was obtained for other growth temperatures. However, the linewidth broadening resulting from LCM was much more pronounced at the higher growth temperatures.

Transmission Electron Microscopy

As further verification that lateral composition modulation is occurring in the InGaAsP/GaAs system and to correlate the temperature dependence of the PL to the LCM, three different samples grown at temperatures of 525 °C, 500 °C and 480 °C were analyzed. The resultant TEM images are shown in Fig. 2.9. These cross-sectional TEM images were taken along the $[0\bar{1}1]$ direction, under two beam conditions using diffraction vector g=022. In each of these samples, a GaAs quantum well was grown within the InGaAsP layer, as a frame of reference.

The dark-bright contrast modulation which is clearly observable in these images is a direct result of lateral composition modulation. As has been studied in detail for growth

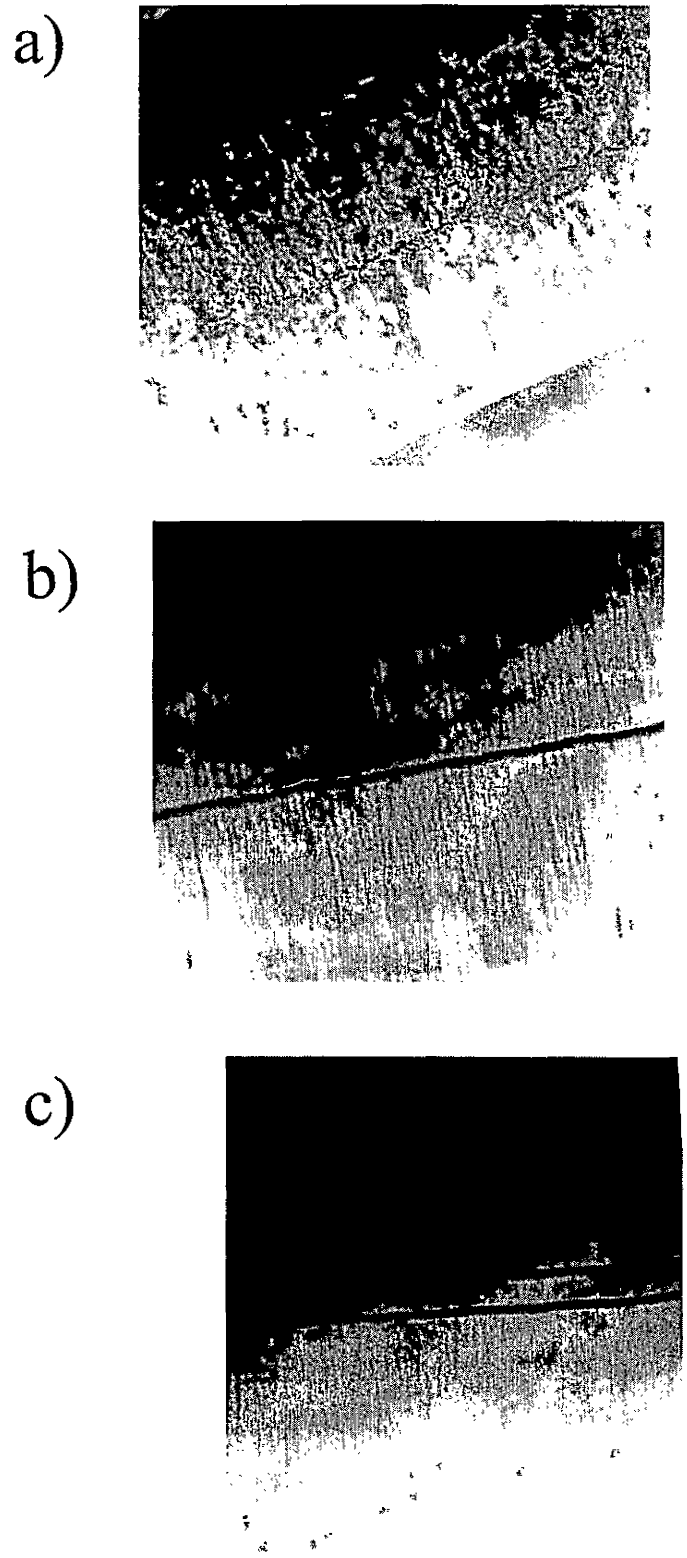

Figure 2.9: Cross-sectional TEM image illustrating the lateral composition modulation for growth temperatures of a) 525 °C, b) 500 °C and c) 480 °C.

of InGaAsP on InP [11], this contrast is due to elastic relaxation of the (022) lattice planes at the free surface of the foil, as a result of the strain associated with the InAs-rich and GaP-rich regions. Higher growth temperatures have been observed to produce more severe LCM, which results in a larger dark-light contrast. A similar relationship between the severity of LCM determined by TEM, and sample composition, consistent with the phase separation model, has also been observed [15].

The compositionally differentiated regions within the sample can be viewed structurally as platelets or discs. The diameter of the disc is approximately 10 times its thickness. These platelets are oriented with their two larger dimensions in the [100] and [0$\bar{1}$1] directions. In Figure 2.9, the cross section of this structure is clearly observed, with one of the longer axes approximately vertical, in the growth direction ([100]) and the short axis direction approximately horizontal, in the plane of the growing surface ([011]).

In Fig. 2.9a), which shows the TEM image of the 525 °C sample, a distinct transition from a relatively 'ordered' LCM to an almost turbulent structure is observed approximately half way from the start of the quaternary layer growth (lower part of Fig. 2.9a) to the quantum well. This transition has not been reported previously, and will be studied in more detail in the future. The photoluminescence spectra from the GaAs quantum wells were measured, with the narrower PL linewidths corresponding to the lower growth temperature (460 °C). For fabrication of quantum well laser diodes, this provided further reasoning for growth of the quaternary layers at 480 °C.

It should be noted that although the thermodynamic phase separation model is effective in predicting the compositions over which LCM should occur, it has been observed that the temperature dependence of the LCM for MBE growth of InGaAsP/GaAs predicted by the model is incorrect. Based on the above thermodynamic arguments, an increase in growth temperature should result in a reduction of the LCM, as a result of the surface

free energy being dominated by the entropy term, favoring the formation of a disordered (homogeneous) alloy. However, this has not been observed in the work described here. This apparent contradiction between theory and experiment can be explained by considering the limitations of the theory. Important growth related processes, such as surface kinetics and surface reactivity, are not considered in the thermodynamic model. In particular, the temperature dependence of surface mobility can be used to explain the difference in the theoretical predictions and the experimental observations.

An increase in temperature results in a decrease of the area within the spinodal isotherm, as a result of the entropy term. As such, a stronger driving force to a random alloy results. However, the above does not consider the surface kinetics, which in MBE, have been shown to have a significant impact on the growth process [16, 17]. It is believed that the reduction in LCM observed as the growth temperature is decreased is a direct result of the decrease in surface mobility associated with the reduced temperature. A similar observation for the growth of InGaAsP/InP has been reported previously [15]. This phenomenon can be explained as follows. As the growth temperature is decreased, the surface mobility is also decreased. For a fixed growth rate, this results in a decrease in the mean diffusion length on the growing surface. The thermodynamic driving force 'pulls' the diffusing surface species to those regions where the surface free energy will be minimized. This results in the InAs and GaP rich regions. However, if the diffusion length is reduced, thermodynamic equilibrium will not be reached, and indeed, the extent to which it will not be achieved is limited by the surface kinetics. (At typical MBE growth temperatures, bulk diffusion can be ignored.) The growth process may now be viewed as a competition between thermodynamics and surface kinetics, whereby kinetic limitations of the surface mobility of the adatoms limits the ability of the system to achieve thermodynamic equilibrium.

Photoluminescence

Samples grown at 525 °C had significantly lower PL intensities compared to those grown at 500 °C. This difference was more pronounced in samples grown within the spinodal isotherm. The surfaces of thicker samples ($E_g \simeq 1.7$ eV) grown at 525 °C, as observed under illumination with short wavelength visible light, were determined to be very rough, as indicated by significant non-specular reflections. This is in contrast to the mirror-like surfaces achieved at lower growth temperatures.

Samples grown at 500 °C had high PL intensities and very large PL linewidths. The PL linewidths of 500 °C samples were as large as 100 meV, which represents a linewidth broadening (relative to the 480 °C samples) of 40 meV, or by a factor of almost 2. Growths at 460 °C resulted in a further linewidth reduction, however, at the expense of PL intensity. This reduction in PL intensity at reduced growth temperatures is associated with grown-in defects, which act as non-radiative recombination centers [18]. As a compromise between PL linewidth and PL intensity, a growth temperature in the vicinity of 480 °C was selected as the 'optimal' growth temperature. It should be noted that the 'optimal' growth temperature is dependent on the details of the intended application of the epitaxial layer.

AFM

From the TEM analysis of the dependence of the film properties on growth temperature, significant surface roughening was observed. To further characterize this phenomenon, three samples were analyzed by AFM, the results of which are summarized in Table 2.2. Consistent with the TEM analysis, higher growth temperatures result in a significant increase in surface roughness.

T_g [°C]	RMS Roughness [Å]
525	35
500	2.17
480	1.56

Table 2.2: RMS surface roughness as a function of growth temperature.

2.3.3 Growth on Vicinal Surfaces

As discussed above in the context of growth temperature, the extent to which thermodynamic equilibrium is achieved can be affected by the mobility of the surface species. To this end, four GaAs vicinal surfaces, as listed in Table 2.3, were used as substrates for the deposition of InGaAsP. In Table 2.3, the surface angle relative to the standard 100 surface

Vicinal Surface Name	Angle	Away from	Fig.
9A	9°	[011]	2.10
311A	25.2°	[011]	2.11
9B	9°	$[0\bar{1}1]$	2.12
311B	25.2°	$[0\bar{1}1]$	2.13

Table 2.3: Vicinal surface data.

is provided, along with the direction from which this angle is measured. (For example, sample 9A has a surface which is rotated by 9° around the $[0\bar{1}1]$ direction, away from the [011] direction.) A schematic of each of these surfaces is provided in the Figures listed in the right hand column of the table. For the 9° surfaces, the surface is viewed looking down the [100] direction, as well as along the cross-section whose surface normal is the axis of rotation. The various crystallographic directions are also provided in the figures to assist in their visualization.

These substrates are interesting for growth of samples where LCM occurs on [100]

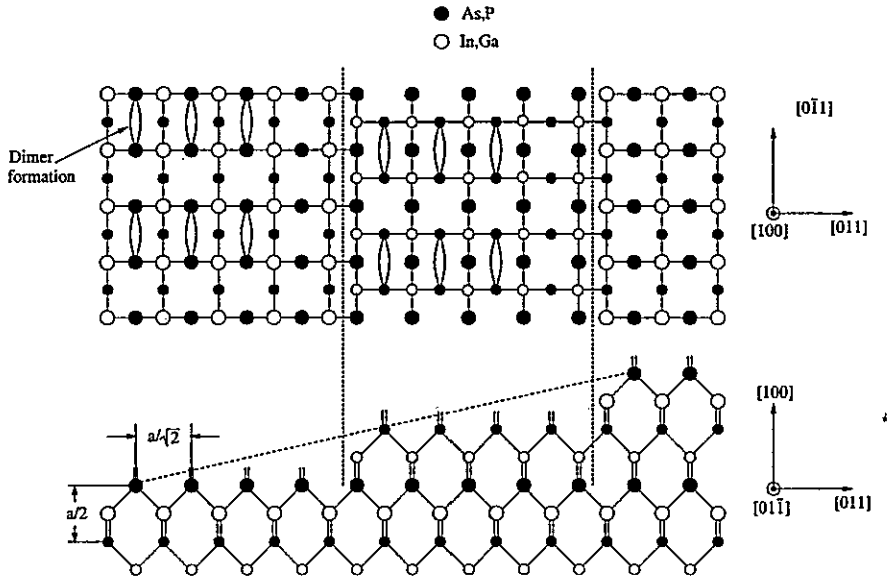

Figure 2.10: 9° A surface.

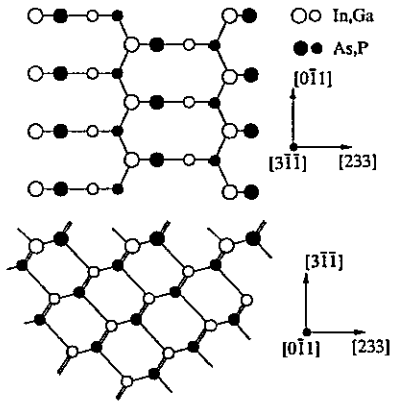

Figure 2.11: 311 A surface.

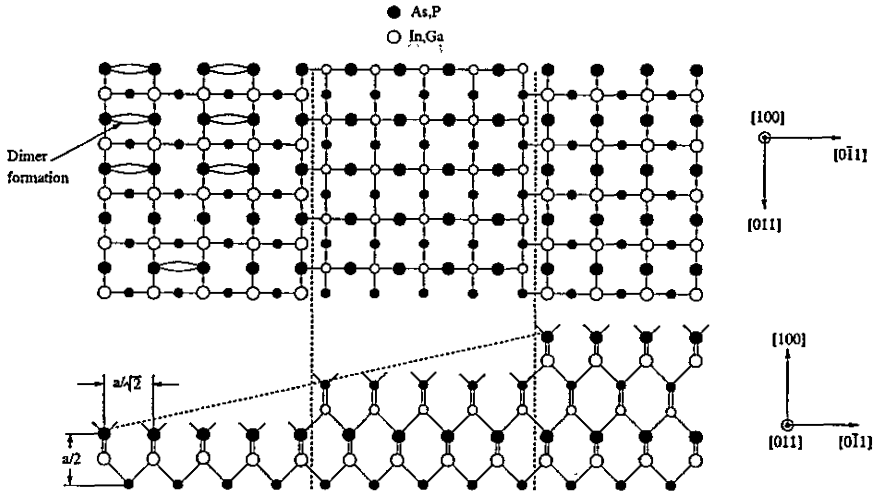

Figure 2.12: 9° B surface.

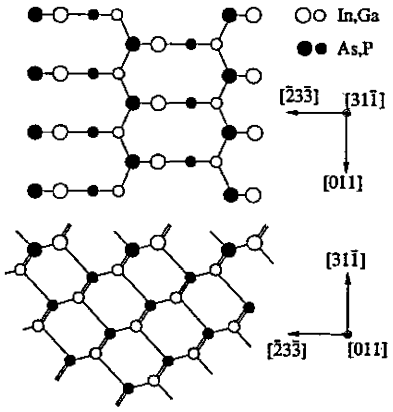

Figure 2.13: 311 B surface.

oriented substrates, as a result of the very different growth surfaces that they provide. In particular, these surfaces have very different properties, as seen by the diffusing adatoms, in the two orthogonal directions in the plane of the surface. Since a strong anisotropy is observed in the LCM structure, such controllable, direction dependent surface properties allow otherwise unattainable insight into the understanding and reduction of the lateral composition modulation phenomenon.

Experimental Results

The standard sample structure, consisting of 3000 Å of InGaAsP sandwiched between 250 Å of InGaP, was grown on the above substrates, at a temperature of 480 °C. All samples were lattice matched to within 1×10^{-3} as determined by X-ray diffraction measurements. It was observed that the incorporation of As and P on these samples was significantly different from that observed on [100], the details of which were not studied.

In general, samples grown on A-type surfaces had narrower linewidths than those grown under identical conditions on [100] substrates. The reduced linewidth for growth on A-type substrates occurred for samples with compositions for which LCM is predicted. It was also observed that the decrease in PL intensity, which has been associated with a reduction in PL linewidth did not occur, and in a few cases, the PL intensity was found to increase. In the case of growth on B-type surfaces, an increase in the PL linewidth and a decrease in the PL intensity was observed. The above results may be explained by correlation of the surface mobilities to the observed LCM structure.

The physical characteristics of the LCM can be described by platelets, which are elongated in the [100] and $[0\bar{1}1]$ directions, compared to the [011] direction, as determined by TEM analysis. As such, in the [011] direction, a surface species has a shorter distance to go to reach its thermodynamically favored site than it has in the $[0\bar{1}1]$ direction. Therefore, in order to reduce the LCM, a reduction of the mobility in the [011] direction is desirable.

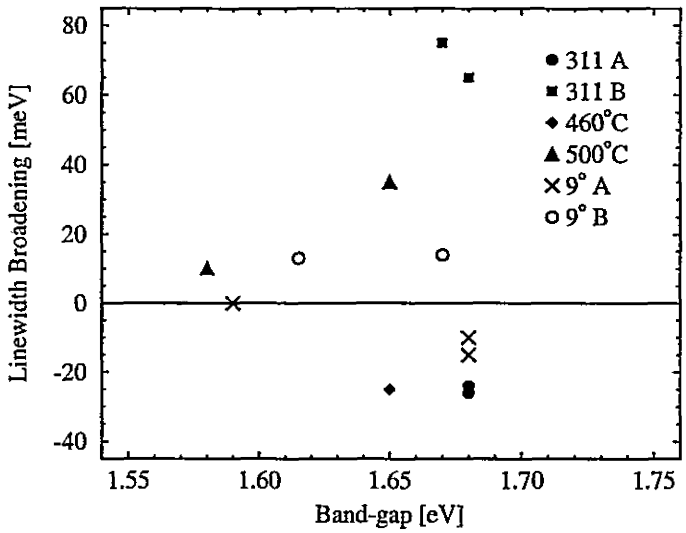

Figure 2.14: Summary of the results of growth on vicinal substrates.

This was the motivation for the use of the A-type vicinal substrates, which contain steps running perpendicular to the [011] direction, which should result in a reduced mobility. Based on the above PL analysis, these substrates provided the desired mobility reduction, and hence LCM reduction.

It was found that the B-type surfaces produced quaternary layers with significantly increased photoluminescence linewidths. The results observed for growth on the B-type surfaces are somewhat surprising, and would require a much more detailed investigation to determine the exact mechanism responsible for this phenomenon.

A comparison of the linewidths obtained on vicinal substrates, relative to those of the 'nominal' samples (grown on 100 GaAs substrates at 480 °C) has been performed, the results of which are illustrated in Fig. 2.14. A negative linewidth broadening corresponds to a narrower PL linewidth relative to the nominal growth. For comparison, the impact of growth temperature is also illustrated in this figure.

As was discussed above, both B-type surfaces resulted in an increase in the linewidth

relative to the nominal samples. The broadening for the 9B samples was approximately 15 meV, whereas that for the 311B samples exceeded 60 meV. The 9A samples resulted in an average decrease in the PL linewidth of between 10 and 15 meV for samples with compositions where LCM is the most severe, and resulted in little or no linewidth reduction where the LCM is only weak. Deposition on 311A samples produced the largest decrease in linewidth, averaging almost 30 meV.

In the range of 460 °C to 500 °C, increased growth temperatures resulted in increased linewidths. However, the higher growth temperatures also resulted in a larger PL intensity. Therefore, reduction in PL linewidth through growth temperature was done at the expense of PL intensity. In the case of growth on the A-type vicinal surfaces, the reduced linewidths did not correspond to a reduction in PL intensity, and in at least two cases, both a reduction in linewidth and an increase in intensity were observed compared to the standard growth on (100) substrates. These results are very promising from the perspective of improved device performance, and will be investigated in more detail in the future.

2.4 Chapter Summary

In this chapter, growth of InGaAsP lattice matched to GaAs by gas source MBE was described. The difficulties associated with the growth of this material were clearly outlined, and the mechanisms responsible for the resultant material properties were identified. A method to improve the material characteristics, through a reduction of the mobility of the surface species was provided, which clearly holds great promise. Additionally, from this growth optimization and an optical constant analysis, to be described in Chapter 4, efficient diode lasers could be designed and fabricated, as will be described in Chapter 5.

Chapter 3

Deposition of SiO_xN_y

As outlined in the introduction, the realization of an ultrashort-pulsed external-cavity diode laser system requires the deposition of a high quality antireflection coating on one or both of the laser diode's facets. This is required to efficiently couple the diode laser to the external cavity. The antireflection coatings described in this thesis were deposited by electron cyclotron resonance plasma enhanced chemical vapor deposition (ECR-PECVD) [19, 20]. In this chapter, the theory of operation and experimental details of the thin film deposition system will be discussed.

3.1 ECR-PECVD

In an ECR-PECVD deposition system, the primary function of the plasma is to provide reactive species for the formation of a film, either through direct excitation within the plasma, or by downstream ion bombardment. The plasma is excited by the resonant coupling of microwave energy to the free electrons in the gas. This resonance condition is obtained through the application of a strong magnetic field (B) which satisfies Eq. 3.1

$$\omega_c = \frac{eB}{m_e} \tag{3.1}$$

where e and m_e are the charge and mass of an electron respectively. The frequency, ω_c is known as the cyclotron frequency, and it is the characteristic frequency of oscillation of

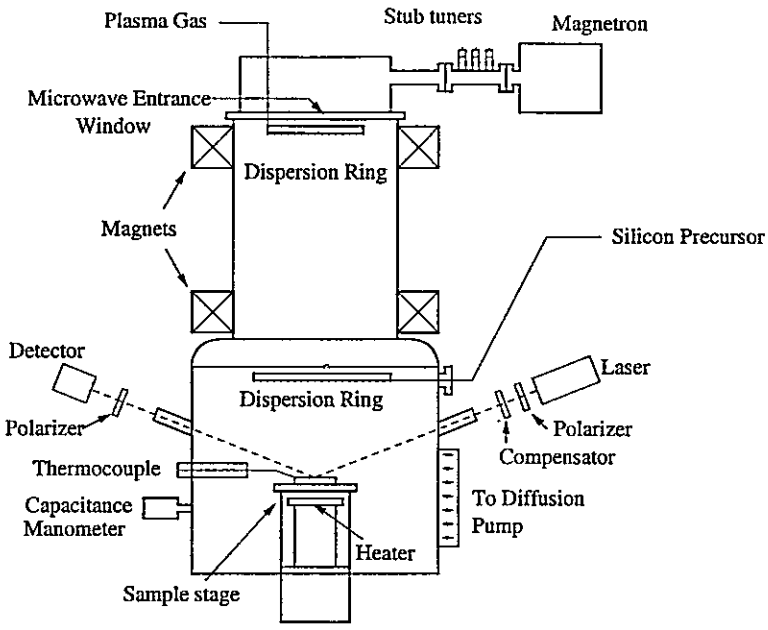

Figure 3.1: Schematic of the McMaster ECR-PECVD system.

an electron in a magnetic field of strength B. Electromagnetic energy will be resonantly absorbed if its frequency is equal to that of the cyclotron frequency.

For a microwave frequency of 2.45 GHz, this resonant condition is achieved by the application of a magnetic field of 875 Gauss. Under these conditions, electrons will absorb energy from the applied electric field, resulting in an increase in the radius of their circular motion. As a result, the probability of collision with the gas species in the chamber will increase, the effect of which may be the liberation of an additional electron, which will absorb energy and continue the process. It is this mechanism that is responsible for the creation of the plasma.

3.1.1 The McMaster CVD System

A schematic of the deposition system used in this work is presented in Fig. 3.1. The chamber is made of stainless steel, and is pumped through a liquid nitrogen cold trap by a diffusion pump, which is backed by a large mechanical roughing pump. A load-lock, which

is pumped with a small turbo pump, is used to reduce the sample transfer time and to reduce chamber contamination during transfers.

The microwave energy used to create the discharge is coupled from the magnetron source, capable of providing 1000 W of power, through a waveguide coupler and stub tuner, as illustrated in Fig. 3.1. The stub tuner is used to reduce the reflected power and increase the power delivered to the chamber by impedance matching the load to the source. The microwaves are transmitted through a quartz window.

The plasma gases, namely Ar, O_2 and N_2 are introduced into the upper part of the chamber, through a small dispersion ring which is located on the bottom flange of the microwave entrance window, at the top of the chamber. Two large circular electromagnets are located at the top and bottom of the upper portion of the chamber, as illustrated in Figure 3.1. This is the region where the plasma is created and maintained.

The lower portion of the chamber houses the sample holder and the manipulation stage. At the top part of this lower chamber is a second dispersion ring through which silane (SiH_4) is introduced. Below the dispersion ring is the sample, which is mounted to a sample holder that is placed on the top of the manipulation stage. Immediately below the sample holder is a heater, which allows the substrate to be heated during depositions. A retractable thermocouple is used to monitor the substrate temperature, and a capacitance manometer is used to monitor the deposition pressure.

Mounted on either side of the deposition chamber are the detector and analyzer assembly of the Rudolph I1000 in-situ ellipsometer. The ellipsometer, which operates at a wavelength of 623.8 nm, provides real-time thickness and index of refraction data. When properly calibrated, and after corrections for various sources of error are applied[1], this ellipsometer is capable of providing index measurements with accuracies of ± 0.003 and a

[1] A discussion of the sources of error encountered in our system, and the approach taken to minimize them is described in [21].

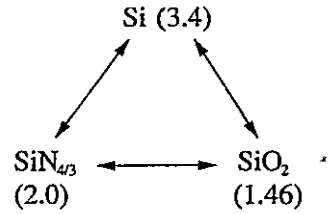

Figure 3.2: Available material composition and index range.

thickness accuracy of ±10 Å.

3.1.2 Thin Films

The films used in this work are formed by the decomposition of SiH_4 in a mixed plasma of argon, oxygen and nitrogen. The properties of the resultant film are a function of the microwave power used to excite the discharge, the magnetic field profile, the deposition pressure and the composition of the plasma gases, as well as the substrate temperature. With the combination of Ar, O_2, N_2 and SiH_4, films ranging in composition from amorphous silicon (a-Si) to either silicon nitride (Si_3N_4) or silicon dioxide (SiO_2), as well as the full range of silicon oxynitrides (SiO_xN_y) can be achieved. These compositions, and the corresponding indices, are illustrated in Fig. 3.2.

A typical calibration curve, describing the dependence of the index of refraction on the relative gas flows is illustrated in Fig. 3.3. In this graph, the index of refraction, which is the film parameter of interest for designing interference filters, is plotted against the relative concentration of O_2 to Ar, in a mixed argon-oxygen plasma, for a deposition pressure of 2.5 mTorr. Similar curves are obtained for mixed plasmas of argon-nitrogen, and argon-oxygen-nitrogen. In all of the above cases, and in particular for SiO_xN_y with the end points being Si_3N_4 and SiO_2, a rapid decrease in the index of refraction as a function of oxygen concentration is observed, especially in the low oxygen content (higher index) regime. By using a 10% mixture of O_2 in Ar (and likewise N_2 in Ar), significantly improved control over the oxygen and nitrogen flows was obtained, which translated directly into

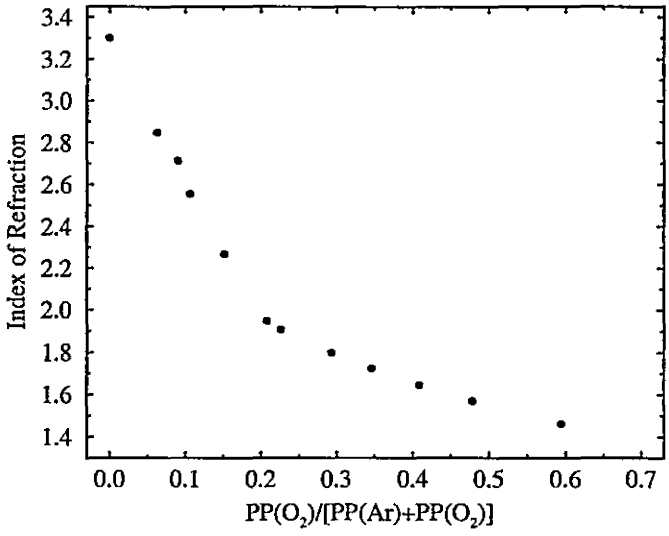

Figure 3.3: Index of refraction versus relative concentration of O_2.

improved index of refraction control.

It should be noted that the index of refraction obtained under given conditions was found to be dependent on the 'history' of the chamber, particularly for the higher index films. To eliminate this history effect, critical depositions were always performed after the chamber had been cleaned for approximately one hour with a 1000 W Ar plasma, and was allowed to pump down over night. It was found that the residual oxygen in the chamber, which was responsible for a reduction in the film index, was effectively removed by this process.

3.2 Material Characterization

To evaluate and improve the quality of the thin films used in this work, a wide range of materials analysis techniques were employed, the details of which are described elsewhere [22, 23].

3.2.1 Compositional Analysis

A complete compositional analysis of the SiO_xN_y thin films has been performed by elastic recoil detection (ERD)[22]. More recently, other ion beam techniques have been employed to study the composition of such films [24], as well as the impact of high temperature rapid thermal annealing. Structural and compositional analysis has also been performed using Fourier transform infrared spectroscopy (FTIR), the details of which can be found in [23]. The details of the above studies have provided insight into the impact of the deposition parameters on the resultant film properties, and have allowed the deposition of controlled, stable and uniform films to both planar substrates and laser facets.

3.2.2 Reflectometry

For application of the above films to interference filters, characterization of the reflectivity as a function of wavelength is required. For planar substrates, these measurements were performed on a modified Perkin-Elmer dual beam absorption system. This system allows the absorption of a given sample to be determined, as a function of wavelength, by measuring the ratio of the detected intensity along two different optical paths, one of which contains the sample. In order to measure reflectivity, a mount was built using a simple optical mirror mount and two gold coated prisms. The first prism reflected the light by 90°, towards the sample mounted on the mirror mount. The reflected light was then redirected along its original path by the second prism. Using such a system, and a known sample such as silicon for reflectance normallization, the reflectivity as a function of wavelength could be measured on an arbitrary sample.

3.2.3 Ellipsometry

Precise control of the index of refraction can be obtained through the control of the deposition conditions, particularly the gas flows. For the fabrication of interference filters, both

the index of refraction and the film thickness must be accurately monitored. As such, an in-situ monitoring technique is essential to the fabrication of such interference filters. However, the application of interference filters to operating wavelengths other than that of the in-situ ellipsometer (632.8 nm) requires knowledge of the index of refraction as a function of wavelength. The wavelength dependent index of refraction information is obtained from an ex-situ spectroscopic ellipsometer.

3.3 Experimental Results

3.3.1 Deposition Conditions

For all of the experiments to be discussed in this thesis, the chamber pressure was maintained between 2.5 and 3.5 mTorr. The total gas flow rate was typically between 15 and 20 sccm, depending on the gas mixture and desired chamber pressure. A base pressure of less than 10^{-7} Torr was maintained before all depositions. The currents in the upper and lower magnets were set at 180 A and 115 A respectively, with microwave powers between 400 and 500 Watts. Typical deposition rates were between 1 and 2 Å/s. These parameters, through a variety of experiments, were determined to be ideal for deposition on sensitive III-V semiconductor laser facets.

The substrate temperature, which is another important deposition parameter, was maintained at approximately 120 °C, which corresponds to the surface temperature that would be achieved as a result of plasma ion bombardment. This temperature was monitored by a shielded tungsten-rhenium thermocouple which could be manipulated within the chamber and placed in contact with the sample surface during a deposition. It was found that a change in temperature during deposition was detrimental to the film quality, as well as the ability of the ellipsometer to accurately monitor index and thickness [21], as a result of the temperature dependence of the optical constants of the substrate. For films that were grown on initially unheated substrates, poor adhesion of the film to the substrate was

observed, as indicated by a simple 'scotch tape' test.

3.3.2 Interference Filters

A wide range of optical filters were deposited using the McMaster ECR-PECVD system, each of which was designed for a different application [21, 25]. Included in the above are broad-band high reflection coatings and antireflection coatings, both of which are relevant to this work. Reflectivities greater than 95% have been demonstrated both on bare substrates, and more importantly, on InGaAsP/GaAs laser facets. However, since the focus of this work requires the application of antireflection coatings, only this type of filter will be discussed in detail. Also, with respect to process control, obtaining a high quality AR coating requires significantly more effort than does a broad-band HR coating.

The standard single layer antireflection coating is based on the quarter wavelength layer where the index of refraction of the film is dependent on the substrate on which it is to be deposited. These relationships are

$$t_f = \frac{\lambda}{4n_f} \tag{3.2}$$

$$n_f = \sqrt{n_s} \tag{3.3}$$

where n_f and n_s are the index of refraction of the film and substrate respectively, t_f is the film thickness and lambda is the wavelength.

An example of a high quality antireflection coating deposited on a GaAs wafer, designed to be antireflecting at 980 nm is illustrated in Fig. 3.4. This coating was later measured using the spectroscopic ellipsometer described in Chapter 4, and was determined to have an index of refraction, at 980 nm, of 1.872 $\pm$0.005, and a thickness of 1315 Å $\pm$10 Å. The theoretical values of the index of refraction and thickness of a perfect antireflection coating on GaAs (n_s=3.523) at a wavelength of 980 nm are 1.877 and 1309 Å respectively. These are in excellent agreement with the experimentally obtained values. As is clearly

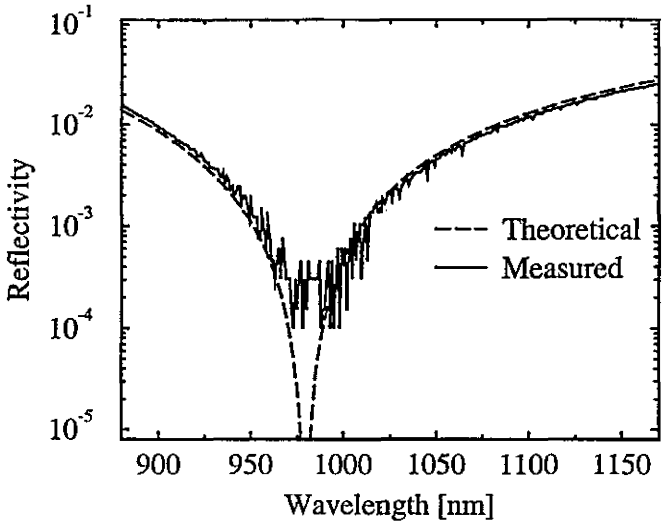

Figure 3.4: Antireflection coating on GaAs.

illustrated by comparison of the experimental data with the target reflectivity curve, precise control over the deposition parameters enables the fabrication of very low reflectivity coatings. The minimum measurable reflectivity with this system has been determined to be approximately 1×10^{-4}. (All experimental values less than 1×10^{-4} were replaced with 1×10^{-4}.) The absolute reflectivity at 980 nm was measured independently with a tunable diode laser, which is a much more intense source, and hence provided a better signal to noise ratio. A reflectivity in the mid to high 10^{-5} range was determined.

3.4 Laser Facet Coatings

Antireflection facet coatings are an integral part of the external-cavity mode-locked diode laser system, and as such, a system with the flexibility to coat a wide range of different laser structures is required.

The facet coatings were applied to lasers that were unmounted, and in bar format, a schematic of which is provided in Fig. 3.5. Light is emitted from the laser facet which is labeled in the figure. The top contact pads for the individual ridge waveguide lasers are also

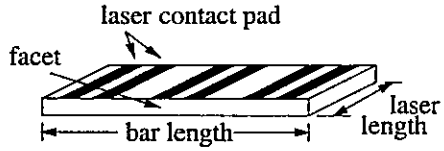

Figure 3.5: Typical laser bar structure.

illustrated. A full laser bar contains 13 pairs of lasers. For ease of mounting, only partial laser bars were coated, usually containing at least 5 laser pairs.

To ensure that the coating is uniform, the laser bar must be attached to the sample holder in such a way that the facet is fully exposed. At the same time, deposition on either laser contact is undesirable, and should be avoided. These criteria were satisfied by placing the laser bar between two silicon wafers that were placed on the smooth surface of the stainless steel sample holder. The larger of the two pieces was rigidly secured to the holder by tungsten pins. The smaller piece was gently pushed flush against the bar, effectively clamping it between the two silicon samples. The smaller sample was clipped to the holder with flexible molybdenum foil to prevent mechanical damage to the laser, and to reduce the potential introduction of stresses due to the temperature cycling during deposition.

The thickness of the wafer against the n-type contact (bottom) of the laser was chosen to be between 10 and 50 μm thicker than the laser length. This was done to ensure that the bottom contact was not coated, while at the same time ensuring that the active region was not shadowed by the silicon piece. The silicon wafer adjacent to the top contact was chosen to be proportionately thinner, to ensure that the active region, which is located approximately 1 μm from the top contact, is not shadowed, while at the same time preventing significant coating of the top contact. Since contact is made to the p-side with a sharp electric probe, some coating to this contact can be tolerated.

After the laser has been mounted to the sample holder, the holder is loaded into the chamber via the load lock. The in-situ ellipsometer is aligned and the sample is heated to a temperature of approximately 120 °C, as measured by the thermocouple which is placed

on the silicon witness sample. The gas flows are then set to the appropriate values which are determined from the gas flow-index of refraction calibration data. After the gas flows have stabilized, the plasma is initiated. During this time the sample is shuttered, such that it is not directly exposed to the plasma. After the plasma has stabilized and a preset time has elapsed, the shutter is opened, and deposition begins. It should be noted that even when the shutter is closed, the deposition rate is non-zero. It has been found that exposure to the plasma immediately after it has been created tends to result in films with poorer adhesion. This could be attributed to potential compositional fluctuations during the initial plasma generation. Additionally, the deposition that does occur on the laser facets when the sample is shuttered is done under a much reduced ion bombardment, which is a gentler process, which may then produce a better surface on which to grow the remaining film. The deposition is terminated after the desired thickness, as measured by the ellipsometer, has been achieved.

3.5 Chapter Summary

Through the optimization of the deposition process described above, and the index and thickness control provided by the in-situ ellipsometer, high quality antireflection coatings have been demonstrated. A system that can facilitate the deposition of such coatings on laser facets, which is scalable to higher throughput volumes, has been developed. Details of the experimental results of antireflection coated diode lasers are provided in Chapter 6.

Chapter 4

Optical Constants

The efficient design of semiconductor optical devices requires precise knowledge of the optical constants [1] of the materials to be utilized. The most common material systems used to manufacture diode lasers are the InGaAsP/InP system and the AlGaAs/GaAs system, both of which have been thoroughly studied from the perspective of their optical constants. This is evidenced by the large number of publications [26-31]. In the case of the InGaAsP/InP system, the enormous interest in this material stems from its use in fabricating emitters and detectors used in current fiber optic transmission systems. The AlGaAs/GaAs system has also been heavily studied since the first demonstration of laser action in GaAs, and subsequently in AlGaAs. Recent applications, such as in compact disc players, and perhaps more importantly in erbium doped fiber amplifier modules, have maintained interest in this system. Alternatively, to date, there is no experimental data available on the optical constants of the InGaAsP/GaAs system, except for that recently published by the author [32]. In this chapter, the analysis of InGaAsP samples by variable angle spectroscopic ellipsometry will be discussed, and the resultant indices as a function of both material band-gap and wavelength will be provided.

[1] The use of the term 'optical constants' is at times misleading, since the 'optical constants' are usually not constant, particularly with respect to wavelength. However, this term is well established in the literature, and as such is used throughout this thesis.

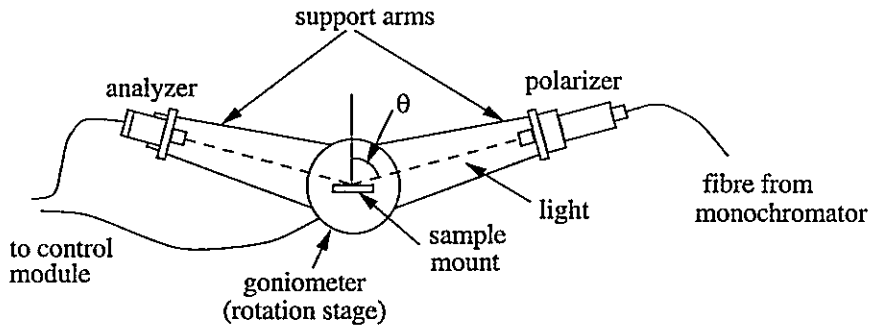

Figure 4.1: Overhead view of the variable angle spectroscopic ellipsometer.

4.1 Variable Angle Spectroscopic Ellipsometry

Variable angle spectroscopic ellipsometry is an extremely powerful technique which can be used to determine the optical constants of a wide range of materials. As was mentioned briefly in Chapter 2, ellipsometry measures the change in the polarization state of a monochromatic beam of light upon reflection from the surface of a sample. In variable angle spectroscopic ellipsometry, measurements are made at a number of different angles, for a variety of wavelengths. This approach has the ability to accurately determine the wavelength dependence of the optical constants, which is required for many applications.

The spectroscopic ellipsometer used in this work is a variable angle spectroscopic ellipsometer manufactured by J.A. Woolam Co. Inc. known as the VASE. This ellipsometer is able to measure Δ and ψ for wavelengths ranging from 300 to 1600 nm, and angles ranging from essentially 0 to 90 degrees, relative to the surface normal. Schematics of the ellipsometer are provided in Figs. 4.1 and 4.2.

The xenon lamp is a bright broad spectrum source from which a narrow wavelength range is selected by the monochromator. The light is transferred to the polarizer via an optical fibre. The polarizer is used to provide a fixed polarization state of the light incident on the sample. The reflection from the sample is then detected by a semiconductor detector, after it passes through the analyzer, which is also a polarizer. Since the polarization state

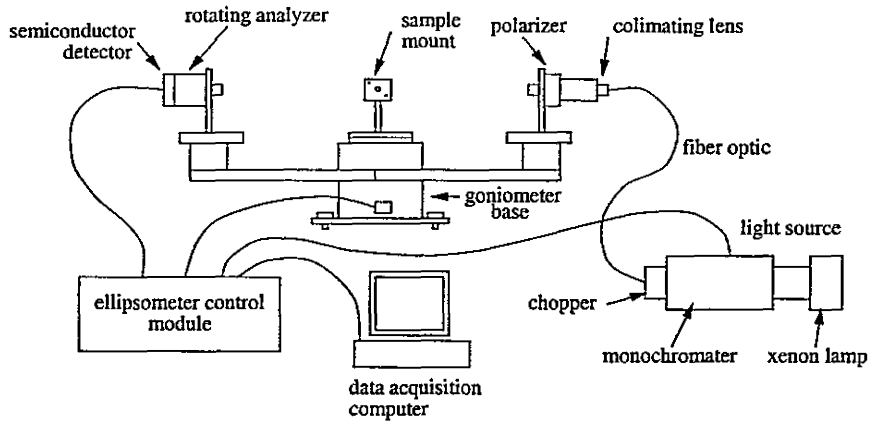

Figure 4.2: Side view of the variable angle spectroscopic ellipsometer.

of the light is known prior to reflection from the sample, and the polarization state at the detector, after reflection from the sample is measured, the effect of the sample is fully characterized.

This ellipsometer is a rotating analyzer ellipsometer, which means that the analyzer is rotated to analyze the polarization state of the reflected light. The analyzer is rotated at a fixed frequency, allowing a Fourier analysis of the detector signal intensity to be performed, from which the ellipsometric angles can be determined.

The computer and the control unit are used to control the ellipsometer configuration and operation, and for data acquisition. User specified parameters, such as wavelength range, wavelength step size, acquisition angles, and integration times are input in a data acquisition file that the ellipsometer control unit uses to automatically acquire the specified data.

An optional component of the ellipsometer that does not appear in Fig. 4.1 or Fig. 4.2 is the 'autoretarder'. This component, which is placed on the sample side of the polarizer, is used to increase the sensitivity of the ellipsometer. Rotating analyzer ellipsometers have reduced sensitivities when the light entering the detector is nearly linearly polarized (Δ=0°, 180°). The sensitivity is a maximum when Δ is near 90°. The autoretarder is a computer

controlled device that consists of two rotation stages that rotate and tilt a birefringent crystal. This allows control over the polarization state of the light that is incident on the sample. As such, the resultant polarization state at the detector can also be controlled and maintained in a regime with maximum sensitivity. The autoretarder was in place for the analysis of all of the semiconductor samples studied here.

4.2 Optical Constants: Mathematical Representation

The electronic excitation spectrum of a material can be described by either its frequency-dependent complex dielectric constant $\epsilon(\omega)$ or its complex index of refraction, N(E) which are given by Equations 4.1 and 4.2 respectively.

$$\epsilon(\omega) = \epsilon_1(\omega) - i\epsilon_2(\omega) \tag{4.1}$$

$$N(E) = n(E) - ik(E) \tag{4.2}$$

In this thesis, the optical constants are presented in the form of the complex index of refraction only. The real part of N (n) is referred to as the index of refraction and the imaginary part (k) is referred to as the extinction coefficient.

The propagation of plane waves in an isotropic absorbing medium can be described by the complex index of refraction, as given in Eq. 4.2. The full expression for a plane wave propagating in a material described by N is

$$\vec{E} = Re\left(\vec{E_0}\, e^{i\omega t+\delta}\, e^{-i\omega Nz/c}\right) = \left(\vec{E_0}\, e^{i\omega t+\delta}\, e^{-i\omega nz/c}\, e^{-(2\pi k/\lambda)z}\right) \tag{4.3}$$

where $\vec{E_0}$ defines both the polarization and amplitude of the field, c is the speed of light in vacuum and δ is a constant phase term. From above, the phase velocity of the wave in the medium is c/n, and the amplitude decays exponentially at a rate of ωk/c (2πk/λ).

Recall that the ellipsometer measures the two angles, Δ and Ψ, which are related

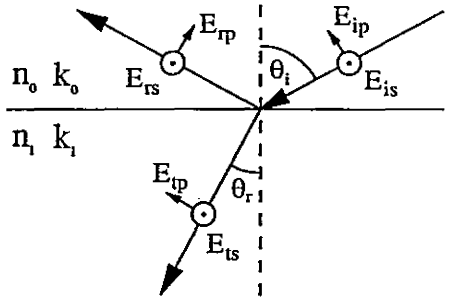

Figure 4.3: p and s polarization states.

to the material properties through the Fresnel reflection coefficients, as given below.

$$\rho = \frac{R_p}{R_s} = \frac{|R_p|}{|R_s|} e^{i(\delta_p - \delta_s)} = \tan(\psi) e^{i\Delta} \tag{4.4}$$

R_p and R_s are the Fresnel reflection coefficients for p and s polarized light.

The simplest situation for which the above expression may be applied corresponds to that of reflection of a monochromatic plane wave at the discontinuity between two semi-infinite media. This case is referred to as the two phase model, where N_0 and N_1 are the complex indices of refraction of material '0' and '1' respectively. The electric field and material notation are illustrated in Fig. 4.3.

A simple expression relating the index of refraction of medium 1 to the index of medium 0, the angle of incidence and ρ can be derived, and is provided in Eq. 4.5.

$$N_1 = N_0 \tan(\theta_i) \sqrt{(1 + \frac{4\rho}{(1+\rho)^2} \sin^2(\theta_i))} \tag{4.5}$$

The angle of incidence relative to the surface normal is given by θ_i, as illustrated in Fig. 4.3. Provided the complex index of refraction, N_0 is known, N_1 can be determined directly from the ellipsometric angles.

In the case of reflection from a semi-infinite substrate with an overlayer, a significantly more complicated relationship between the ellipsometric angles and the physical parameters (thickness, optical constants) can be derived. However, as above, provided the complex index of refraction of the substrate is known, the thickness and index of refraction

of a transparent film can be determined. Likewise, the substrate complex index of refraction can be determined provided the thickness and optical constants of the overlayer are known.

For a practical analysis of the above situation, as well as for more complex cases, a straightforward matrix approach is taken [33]. The effect of each interface and layer on the propagating plane wave is written in matrix form as a function of the optical constants and thicknesses of the respective layers. This allows the contribution of each layer and interface to be treated separately .

4.2.1 Kramers-Kronig Relations

The real and imaginary parts of the index of refraction are not independent, but rather are related through the well known Kramers-Kronig relations, given in Equations 4.6 and 4.7.

$$n(E) = 1 + \frac{2}{\pi}\int_0^\infty \frac{E'k(E')}{(E')^2 - E^2}dE' \tag{4.6}$$

$$k(E) = -\frac{2}{\pi}\int_0^\infty \frac{n(E') - 1}{(E')^2 - E^2}dE' \tag{4.7}$$

Similar relationships exist for the dielectric constants, ϵ_1 and ϵ_2, which are related to the complex index of refraction through Eq. 4.8.

$$\epsilon_1 = n^2 - k^2 \qquad \epsilon_2 = 2nk \tag{4.8}$$

For an analysis of optical constants, the above relationships provide a constraint on the potential values of n(E) and k(E), or alternatively, ϵ_1 and ϵ_2. A model for the evaluation of optical constants, which requires that the above KK relationships be satisfied, is said to be Kramers-Kronig consistent. For an analysis of samples where absorption is non-negligible over the wavelength range of interest, a Kramers-Kronig consistent model must be applied to obtain physically meaningful optical constants.

4.3 Material Dispersion

The variation of the index of refraction with wavelength is referred to as dispersion. A wide range of optical constant dispersion models have been developed in order to calculate and characterize the optical response observed experimentally in real materials. Since the optical constants of the InGaAsP/GaAs and SiO_xN_y systems are described within this chapter, only those models which are applicable to these materials for visible and near IR wavelengths (300-1600 nm) will be discussed.

4.3.1 Semiconductors

In the analysis of semiconductors, a number of different models have been proposed to describe the relatively strong dependence of the optical constants on wavelength. In the near IR and visible wavelengths, these models are based on a fundamental description of the band structure of the given semiconductor.

The electronic structure of III-V semiconductors can be described in terms of energy bands. An energy band represents a range of energies over which an allowed electron energy level exists. In terms of the interaction of a semiconductor with optical frequencies, the two most relevant bands are the conduction and valence band. The smallest energy separation between these two bands is known as the fundamental energy gap, and is designated E_0. There are a number of other important electronic transitions which in many respects are similar to the E_0 transition, however, they have a larger energy separation. In order of increasing energy, they are known as the E_1, E_2 etc. gaps. These transitions are responsible for peaks in the absorption spectra as a function of photon energy.

The relationship between the band structure of the semiconductor and ϵ_2 is given in Eq. 4.9 [34]

$$\epsilon_2(E) = \frac{4e^2\hbar^2}{\pi\mu^2 E^2} \int \mid P_{cv}(k) \mid^2 \delta[E_c(k) - E_v(k) - E]dk \tag{4.9}$$

where μ is the combined density of states effective mass and E is the photon energy. P_{cv} is the momentum matrix element of the valence and conduction band states. $\delta[E_c(k) - E_v(k) - E]$ is the Dirac delta function representing the spectral joint density of states (DOS) between the valence band and the conduction band, with an energy separation given by E. The ϵ_1 spectra is then expressed as a function of ϵ_2 through the appropriate Kramers-Kronig relation.

This expression, which relates the absorption spectra to the semiconductor band structure, requires further discussion. The presence of the Dirac delta function implies that if an energy separation E, between the valence and conduction bands does not exist, then there will be no contribution to $\epsilon_2(E)$ at that energy. This implies that there will be no absorption, which is observed for photons of energy less than the semiconductor energy gap (E_0). The momentum matrix element in Eq. 4.9 also plays an important role in determining the $\epsilon_2(E)$ spectra. This is a result of the fact that $\mid P_{cv}(k) \mid^2$ determines the probability of a transition occurring between the two states $E_c(k)$ and $E_v(k)$.

Wavelength Regions

The optical spectra of III-V semiconductor materials can be separated into several wavelength regions, each of which has a substantially different optical response as a result of the different physical mechanisms of the field-material interaction.

For very low energy photons, less than approximately 0.1 eV, the material interaction with the field occurs via lattice vibrations and in general the absorption is small. The exception is in the vicinity of specific frequencies which correspond to those of the transverse and longitudinal optical phonons.

For higher energy photons, approaching those of the fundamental energy gap (E_0) of the semiconductor, lattice vibration interactions with the field are negligible, and the optical constants are determined by the electronic band structure of the material. In this

wavelength range, where the photon energy remains less than E_0 the material is approximately transparent.

For energies at or above the band-edge (E_0) absorption becomes non-negligible. At the band-edge, the extinction coefficient (k) rises rapidly from zero to a value in the range of 0.1. For larger photon energies, the absorption continues to increase, until it reaches a local maximum. The energy of this absorption peak corresponds to that of the E_1 energy gap. Further increase in photon energy results in a decrease in the absorption, until the photon energy approaches that of the next major electronic transition.

The wavelength range that is most relevant to materials to be used in lasers is that corresponding to photon energies from the band-edge to hundreds of meV below the band-edge. For quantum well lasers in particular, the material forming the waveguide core and cladding, and the barrier layers is transparent to the photon emitted from the well. As such, for the design of quantum well lasers, the index of refraction of the materials for photon energies smaller than their band-gap are the most relevant.

4.3.2 Dielectrics

In the context of optical constants, the term dielectric is commonly used to describe a material which is optically transparent, and is usually electrically insulating. The SiO_xN_y films deposited in this work are considered dielectrics. Unlike the situation described above, the wavelength dependence of the optical constants of a dielectric is rather uninteresting, particularly in the wavelength range relevant to these studies. For visible to near infrared wavelengths, only a weak dependence on wavelength is observed.

4.4 Dispersion Models

Based on the band-structure, several analytical models have been developed to explain the $\epsilon(E)$ (N(E)) spectra of semiconductors. These include the harmonic oscillator approxima-

tion (HOA) [35], the standard critical point model (SCP) [36] and the model dielectric function (MDF) [37], as well as a number of other models which represent minor variations of those above. One of the models which was used to extract the optical constants from the ellipsometric angles is the Parametric Semiconductor Model, developed by J.A. Woollam Inc. [38, 39]. The starting point of this model is based on the critical points [2] of the semiconductor band structure, whereby the total number and energy of the critical points is left as a fit parameter, as well as a number of parameters which characterize each of the critical points individually. This model is based very closely on that of a modified critical-point parabolic-band model described by Kim and Garland [40, 41]. The details of these models will not be provided here, however, the interested reader may refer to the references provided above.

For the analysis of semiconductors for photon energies below the band-gap, or for the analysis of dielectrics, a number of different empirical models can be used to describe the relatively simple wavelength dependence of the refractive index which is observed experimentally. The three most common dispersion relationships are the Sellmeier, Cauchy and Single Effective Oscillator, which are provided in Equations 4.10, 4.11 and 4.12 respectively.

$$n^2(\lambda) = A + \frac{B\lambda^2}{\lambda^2 - C} \tag{4.10}$$

$$n(\lambda) = A + B/\lambda^2 \tag{4.11}$$

$$n^2 - 1 = \frac{E_0 E_d}{E_0^2 - E^2} \tag{4.12}$$

Provided the probe wavelength is sufficiently far from the band-gap of the semiconductor material, all three of the above relationships have been shown to effectively portray the dispersion observed in semiconductors [42-46]. However, it has been observed previously [47], as well as in this work [32], that the Cauchy relationship and the single effective oscillator model deviate from the experimental data at energies much further from the band-edge

[2] The critical points refer to peaks in the absorption spectra, which result from the band structure of the semiconductor.

than does the Sellmeier relationship. Improvement in the fitting can be obtained for the Cauchy relationship with the addition of terms of even power in $1/\lambda$. A modified single effective oscillator model has been proposed [44, 47], which also provides a better fit to experimental data, particularly approaching the band-edge.

4.5 Experimental Approach

Practical analysis of optical constants requires the development of a physical model which accurately describes the system being studied. Once a model is developed, Δ and Ψ can then be calculated as a function of the angle of incidence and wavelength, based on the given model parameters. A best fit can then be determined by minimizing an error function which is a measure of the deviation of calculated Δ and Ψ values from those determined experimentally. This minimization is performed by incrementally changing parameters in the model, such as thickness and index of refraction until a best fit is obtained.

The model may be as simple as that of a single, continuous substrate, where only the optical constants (n,k) are unknown. Conversely, the model developed to describe the experimental results may contain a large number of different layers, with unknown optical constants and thicknesses. Such a model may also include parameters such as surface roughness, index grading or material inclusions, in any or all of the layers. The general approach in the development of a model is to begin with a relatively simple one, which can be made more complex as required. However, only when the model has been shown to be deficient, based on poor agreement between the generated and experimental data, should a more complex model be considered.

The simplest model consists of a single, homogeneous infinite substrate with an atomically abrupt air/substrate interface. Such a model is referred to as a two phase model, the two phases being that of the ambient and the sample. This model is often insufficient in describing the situation encountered experimentally, particularly for the analysis

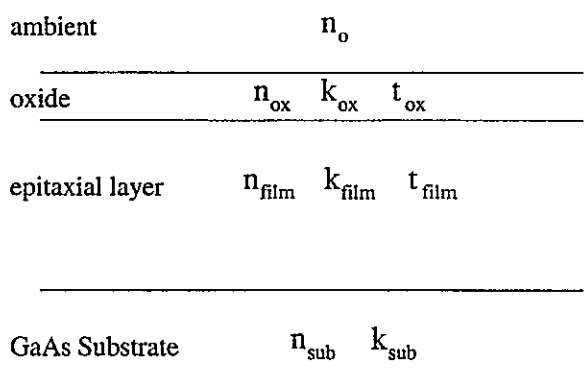

Figure 4.4: Physical model used in the analysis of all InGaAsP samples described here.

of semiconductor samples, where a native oxide layer exists at the ambient/semiconductor interface. As such, overlayers must often be included in the physical model to provide accurate optical constants.

4.5.1 Analysis of InGaAsP/GaAs

In the case of the analysis of bulk semiconductor samples, the situation becomes more complicated than the simple two phase model discussed above, as a result of the native oxide which forms on all III-V semiconductor surfaces. Although this oxide is easily removed by chemical etching, it very quickly regrows after exposure to the atmosphere. As a result, a true oxide-free analysis could only be performed under vacuum conditions, which is not very practical. Given some knowledge of the physical limits of the system, an accurate analysis can still be performed, however, the model must now include the optical constants and thickness of the overlayer.

For analysis of the InGaAsP epitaxial layers on GaAs, the physical model used is that of the four phase model, as illustrated in Fig. 4.4. The resultant ellipsometric angles, Δ and ψ are dependent on the optical constants and dimensions of the three materials in the model, namely those of the oxide layer (t_{ox}, n_{ox}, k_{ox}), the epitaxial layer (t_{film}, n_{film}, k_{film}) and the substrate (n_{sub}, k_{sub}). Unfortunately, the system of equations governing the above relationships is not fully determined, unless additional information on some of the

above parameters is provided, or some appropriate assumptions can be applied. Therefore, in order to determine the optical constants of the InGaAsP epitaxial layers on GaAs, the optical constants of the GaAs substrate must first be determined. To this end, GaAs substrates were analyzed, the details of which are provided in the following section.

GaAs Substrate Optical Constants

Analysis of the optical constants of the GaAs substrate was based on the three phase model, consisting of air, a thin oxide overlayer, and a semi-infinite GaAs substrate. Atomically abrupt interfaces were assumed. The oxide was also assumed to be homogeneous, and non-absorbing in the wavelength range of 300-1600 nm. The index of refraction of the oxide layer was taken from [48], and in the transparency regime of both the substrate and the oxide, the thickness of the oxide was determined from direct inversion of the ellipsometric angles. Using the oxide index of refraction and thickness from above, the optical constants of the substrate could then be determined over the full wavelength range from inversion of the ellipsometric angles. The Herzinger-Johs parametric semiconductor model [38, 39] was also used to fit the full wavelength range of the complex index of refraction. Ellipsometric measurements were made at 5 angles between 70°and 80°, from 300 nm to 1600 nm in 5 nm intervals.

Two different GaAs samples were analyzed, and the resultant index of refraction values agreed to within approximately 0.001 for the transparent region, and to approximately 0.003 for the absorbing region. The largest discrepancy was 0.005, which occurred at the band-gap of GaAs. This is likely a result of the slightly different doping in the two samples which were not derived from the same crystal boule. Doping has been found to affect the measured optical constants predominantly in the near band-edge regime [34, 49].

InGaAsP Optical Constants

After determining the optical constants of the GaAs substrate, a number of assumptions regarding the oxide on InGaAsP are required to obtain the optical constants of the InGaAsP layer. As in the case of the GaAs oxide, the InGaAsP oxide was assumed to be homogeneous and non-absorbing for all wavelengths studied here. The transparency assumption is supported by the data provided in [48], and has been used by others [31].

Secondly, it was assumed that the index of refraction of the oxide layer was independent of the composition of the quaternary layer on which it grows. Since the composition of the oxide will likely be dependent on the composition of the underlying epitaxial layer, this assumption may at first appear inappropriate. However, it has been shown that the index of refraction of the oxide on InP is almost equal to that of GaAs, both of which are only very weakly dispersive. Gallium oxide (Ga_2O_3) has been reported to have an index of refraction of 1.9 [50], whereas indium oxide (In_2O_3) has been reported to have an index in the range of 1.9 to 2.1. The oxide on InGaP, which is the end point ternary of the InGaAsP/GaAs system, has been reported to be 2.0 [51]. In the range of 1.8 to 2.1, the choice of oxide parameters had minimal impact on the resultant substrate/epitaxial layer optical constants. In the final analysis, the optical properties of the oxide of GaAs as determined by Zollner [48], were used, and the oxide thickness was left as a fit parameter. The oxide thickness was determined by analysis of wavelengths well above the band edge, where absorption in the epitaxial layer is zero. A second order Cauchy parametric model was applied to fit the wavelength dependence of the epitaxial layers index of refraction, such that the oxide thickness and layer thickness could be determined. The parametric semiconductor model described previously was also used in the data analysis, which produced essentially identical oxide thicknesses, film thickness and optical constants for all samples studies here. In all cases, the oxide thickness was in the range of 15 to 30 Å, which is in agreement with those

reported elsewhere [31, 51].

This analysis approach resulted in a measurement uncertainty in the index of refraction of a given quaternary sample, in the transparent regime, of approximately ± 0.01. The contribution of the statistical uncertainty in the data, as well as model assumption errors and systematic errors are included in the above.

4.6 Experimental Results

A series of ten samples of InGaAsP with compositions ranging from GaAs to InGaP were grown for the purpose of analysis of the optical constants. Measurements from 300 to 1600 nm, in steps of 5 nm, were made for angles of 70°, 75°, and 80°. All of the samples were nominally undoped and approximately 1800 Å in thickness. They were deposited on [100] n-type GaAs wafers, at a controlled growth rate of 1 μm/h. The growth temperature was maintained at 480 °C as measured by a pyrometer. The lattice mismatch ($\Delta a/a$) of all samples was less than 5×10^{-4} as measured by a double crystal x-ray diffractometer.

4.6.1 Index-Material Representation

The majority of the index of refraction data of III-V semiconductors is usually provided as a function of material composition [28, 46], as opposed to a more easily determined parameter such as band-gap. For various reasons, relating the index of refraction to the band-gap is advantageous. First, the uncertainties associated with the determination of the composition of semiconductor epitaxial layers are often much greater than the uncertainty associated with either the band-gap measurement or the index of refraction measurement [26]. As such, the use of composition introduces a significant source of error. Secondly, measurement of the composition of epitaxial layers is a tedious and complicated process, requiring very specialized equipment. Thirdly, since band-gap and index are the two properties of a semiconductor relevant to laser design, directly relating the two quantities is preferable

to the introduction of a third variable (x, composition). The band-gap of a semiconductor sample is readily determined through standard photoluminescence measurements, which are routinely performed in most epitaxial growth laboratories. In addition, as discussed previously, the index of refraction of a semiconductor sample is intimately related to its band-structure, of which the band-gap is a measure.

Recently, the index of refraction of AlGaAs samples was provided as a function of band-gap, as opposed to composition [26]. The authors of this article made similar arguments for adopting the above convention. They also found a significant discrepancy in the optical constants of AlGaAs as a function of composition. However, significantly better agreement was obtained when the index was related to composition by applying a *single* band-gap composition relationship. This is a result of different groups using slightly different band-gap composition relationships, as is not uncommon.

4.6.2 InGaAsP Index of Refraction

The three most common wavelengths of operation for GaAs based lasers are 808 nm, 850 nm and 980 nm. Wavelengths of 808 nm and 980 nm are important because of their use in pumping Nd:YAG crystals and Erbium-doped fibre amplifiers, respectively. Lasers operating at 850 nm are also important due to their increasing use in short-haul optical communications systems, as well as in numerous other applications, such as free space optical interconnects. As such, the index of refraction of InGaAsP at these wavelengths is plotted as a function of band-gap in Figs. 4.5, 4.6 and 4.7. It should be noted that only those samples whose band-gap is larger than the corresponding probe wavelength are included in the figures.

Also illustrated in Figs. 4.5, 4.6 and 4.7 are the best fit 2^{nd} and 3^{rd} order polynomials, which are given in Equations 4.13, 4.14 and 4.15.

$$n_{i=2}(808) = 11.56 - 8.78E_g + 2.337E_g^2 \tag{4.13}$$

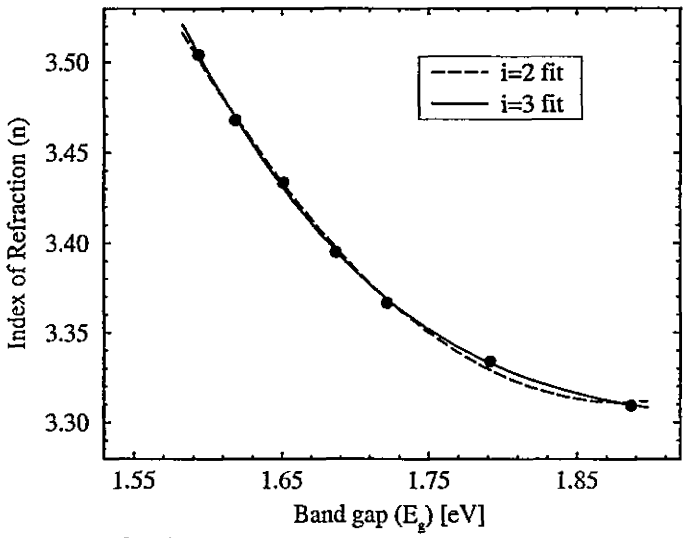

Figure 4.5: Index of refraction at 808 nm as a function of material band-gap.

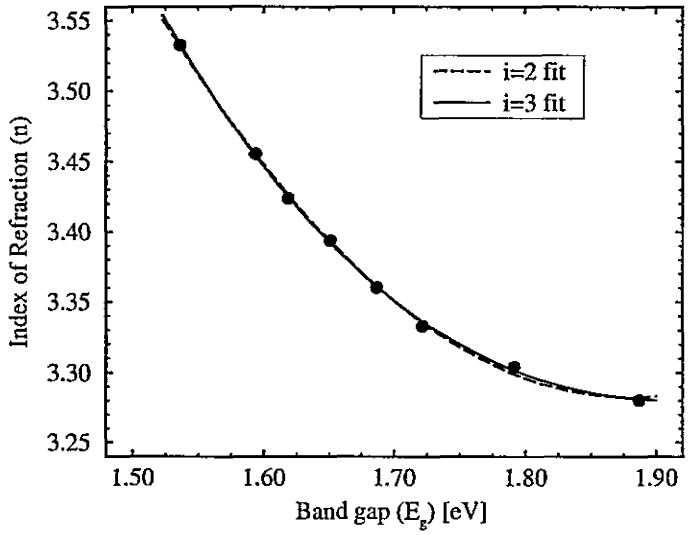

Figure 4.6: Index of refraction at 850 nm as a function of material band-gap.

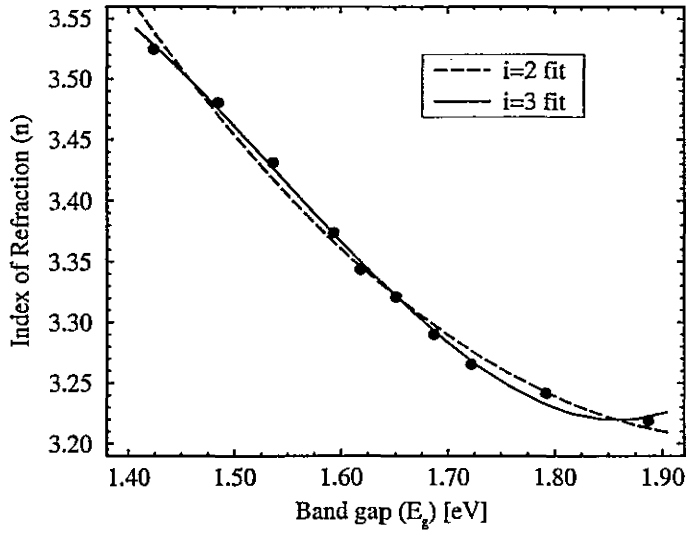

Figure 4.7: Index of refraction at 980 nm as a function of material band-gap.

$$n_{i=3}(808) = 30.77 - 42.06E_g + 21.52E_g^2 - 3.68E_g^3$$

$$\begin{aligned} n_{i=2}(850) &= 10.714 - 7.906E_g + 2.102E_g^2 \\ n_{i=3}(850) &= 17.987 - 20.75E_g + 21.52E_g^2 - 1.469E_g^3 \end{aligned} \tag{4.14}$$

$$\begin{aligned} n_{i=2}(980) &= 7.409 - 4.237E_g + 1.067E_g^2 \\ n_{i=3}(980) &= -6.904 + 21.95E_g - 14.828E_g^2 + 3.20E_g^3 \end{aligned} \tag{4.15}$$

The quality of the polynomial fits, expressed through the adjusted correlation coefficient R^2_{adj} and the standard deviation of the fit (σ) for the above examples is provided in Table 4.1.

As is clear from the figures and Table 4.1, the 2^{nd} order polynomial fit is quite good for both the 808 nm data and the 850 nm data. In these cases, all of the data points lie within the 95% confidence interval of the fit. In both of these plots, the 3^{rd} order fit does not provide a significant improvement. However, the situation is somewhat different for 980

Data, Fit	R^2_{adj}	σ
λ=808 nm, i=2	0.9975	0.003
λ=808 nm, i=3	0.9989	0.002
λ=850 nm, i=2	0.9987	0.003
λ=850 nm, i=3	0.9991	0.002
λ=980 nm, i=2	0.9896	0.010
λ=980 nm, i=3	0.9968	0.006

Table 4.1: Quality of the fits described in Equations 4.13, 4.14 and 4.15.

nm, which corresponds to a photon energy smaller than the band-gap of all of the InGaAsP samples. In the 980 nm data, only the third order polynomial fit's 95% confidence interval contains all of the data points. The requirement for the higher order fit can be explained by considering the difference in the composition ranges which are sampled in the three figures, based on the LCM discussion in Chapter 2.

Since only those samples whose band-gaps are sufficiently larger than the photon energies are plotted, the index data for 808 and 850 nm does not include the full composition range of samples. As was discussed in Section 2.2, lateral composition modulation (LCM), which has been observed in the InGaAsP/GaAs material system, is composition dependent, and manifests itself in the PL spectra as an increased linewidth, as was illustrated in Fig. 2.8. A result of the LCM is the determination of an artificially small band-gap (as determined by PL) due to the enhanced electron-hole pair recombination in the smaller band-gap regions. Thus, for a given composition, the measured band-gap will be smaller than that of the compositionally uniform sample, with the difference in the two values being dependent on the severity of the LCM, and thus, on the sample composition or band-gap. Therefore, for the 980 nm data, the full composition range is sampled. For quaternaries with high As concentrations (small band-gap), the LCM is weak. However, it does increase more rapidly with band-gap at an energy of approximately 1.55 eV, reaching a maximum between 1.7 and

1.8 eV. At higher energies, the linewidth decreases until reaching the composition of InGaP, which has a PL linewidth approximately equal to that of GaAs, for which no LCM occurs. As such, samples which experience the transition from essentially no LCM, to maximum LCM, back to essentially no LCM, are sampled in the 980 nm index data. In the case of the 808 nm and 850 nm index data, those small band-gap samples with minimal LCM are not measured and only the transition from LCM back to no LCM is measured. It should be noted that for any wavelength where all of the InGaAsP samples are transparent, the above trend was observed.

4.6.3 Universal Parameterization

One of the goals of this index of refraction analysis was *to provide a single relationship which would allow the index of refraction of an arbitrary InGaAsP sample, characterized only by its band-gap, to be determined at any wavelength for which the sample is transparent.* In order to obtain such a 'universal' formula, a Sellmeier fit was performed on each of the InGaAsP samples to describe their wavelength dependent index of refraction. This fit was applied to the refractive index at photon energies smaller than the band-gap, by approximately 80 meV. For wavelengths approaching the band-edge, deviation of the experimental data from the dielectric based models has been shown to occur, and has been observed in this work.

The three fit parameters of the Sellmeier relationship (Eq. 4.10) obtained from all of the InGaAsP samples were then fit with a 2nd order polynomial as a function of band-gap, the results of which are provided in Eq. 4.16. The wavelength dependence of the index of refraction of *any* InGaAsP sample is described by the Sellmeier relationship (wavelength in microns). The specific information of a *particular composition* of InGaAsP, as characterized by its band-gap (E_g), is contained in the three Sellmeier fit parameters. Therefore the combination of Eqs. 4.10 and 4.16 provide a full characterization of the index of refraction of InGaAsP lattice matched to GaAs for photons of energy less than the

material band-gap.

$$\begin{aligned} A &= 58.25 - 56.74(E_g) + 15.50(E_g)^2 \\ B &= -27.35 + 35.04(E_g) - 10.02(E_g)^2 \\ C &= 3.72 - 3.87(E_g) + 1.066(E_g)^2 \end{aligned} \tag{4.16}$$

The motivation of this procedure was to establish a universal relationship capable of accurately describing the given experimental data. As such, the quality of the universal relationship was determined by evaluating the root mean square error, as provided in Table 4.2. As a demonstration of the effectiveness of the above fitting procedure, the index of

Wavelength Data	RMSE
λ=808 nm	0.0086
λ=850 nm	0.0088
λ=980 nm	0.0080

Table 4.2: Root mean square error.

refraction at 808 nm, 850 nm and 980 nm, as a function of band-gap, as calculated from the above formulae, are compared to the corresponding experimental data. These results are plotted in Figs. 4.8, 4.9 and 4.10.

As is clearly illustrated in the above figures, the combination of Eqs. 4.10 and 4.16 allows the index of refraction at any wavelength below the material band-gap, for an arbitrary InGaAsP composition (band-gap) to be accurately determined. This represents the first such data set for InGaAsP lattice matched to GaAs.

4.6.4 Experimental Data: Comparison with Published Data

GaAs

The experimentally determined optical constants of GaAs were compared to those which have been published previously, as a measure of the effectiveness of both the variable angle

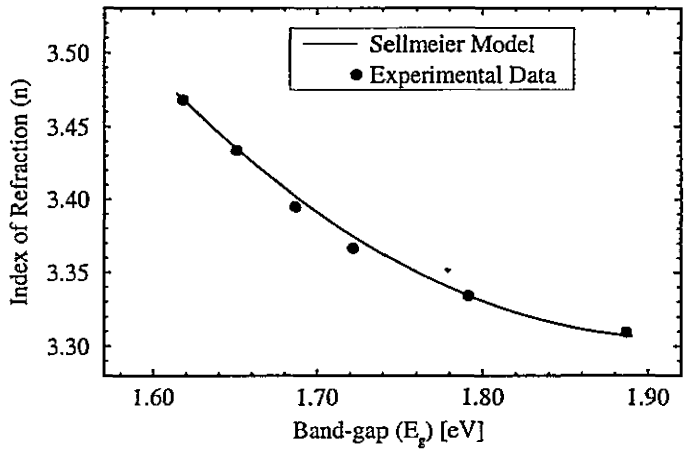

Figure 4.8: Index as a function of band-gap at 808 nm.

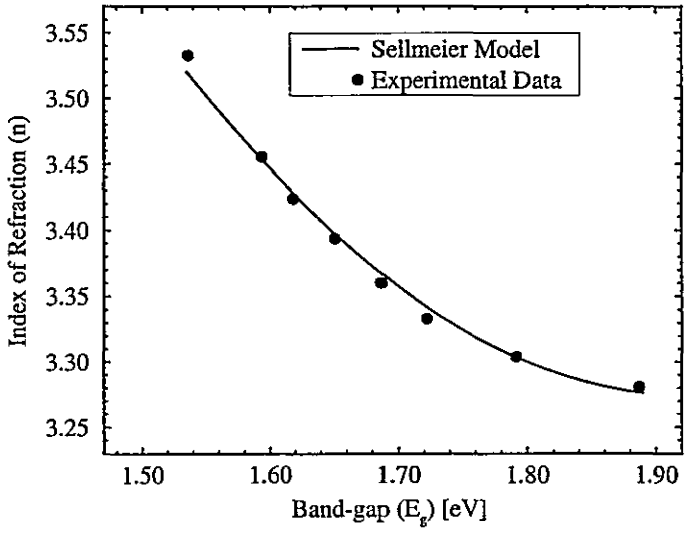

Figure 4.9: Experimental index data and Sellmeier fit index as a function of band-gap at 850 nm.

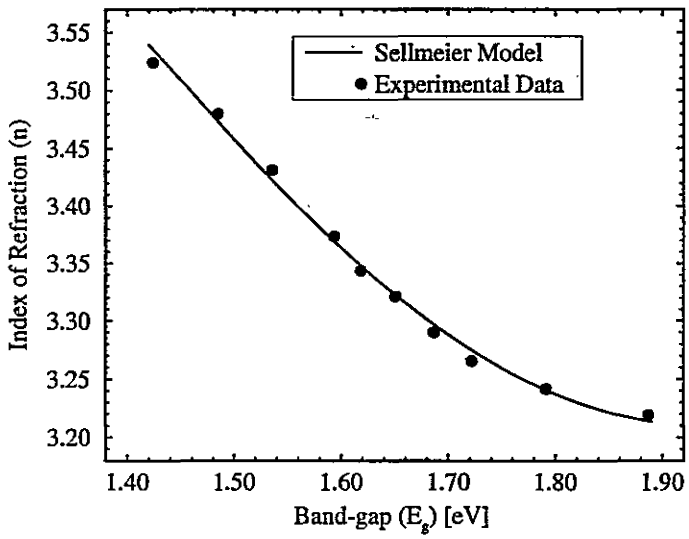

Figure 4.10: Experimental index data and Sellmeier fit index as a function of band-gap at 980 nm.

spectroscopic ellipsometer and the model fitting routines, as illustrated in Fig. 4.11. The author's data corresponds to the Sellmeier fit, and is labeled Sellmeier. Also illustrated in this figure is a fit to the experimental data of Pikhtin *et al* [52] as well as various data points from Adachi *et al* [53] and Palik [54]. As can be seen, excellent agreement of all of the experimental index of refraction data in the transparent regime is obtained. The maximum deviation in the index of refraction within all four data sets is 0.003.

InGaAsP

Since there is no experimental data available for InGaAsP grown lattice matched to GaAs, only the data for InGaP, which has been obtained here will be compared to data available in the literature. Figure 4.12 illustrates the direct Sellmeier fit to the author's experimental data. Also included in the figure are the best fits obtained by Adachi *et al.* [43], Tanaka *et al.* [46] and Roberts *et al* [55]. As is dramatically clear from Fig. 4.12, a very large discrepancy in the experimental data exists. The index of refraction for InGaP obtained by

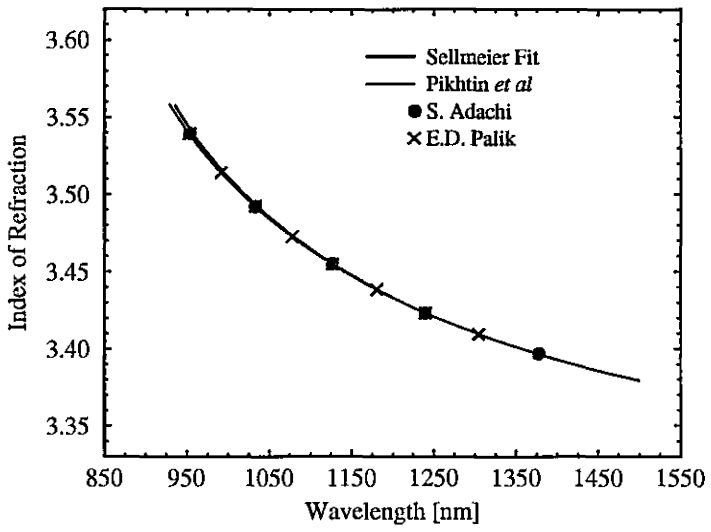

Figure 4.11: Comparison of our index of refraction data in the transparent regime of GaAs with other published data.

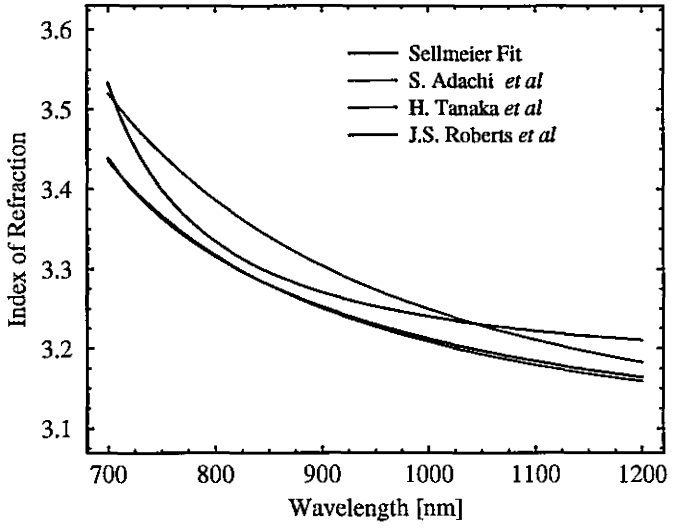

Figure 4.12: Comparison of InGaP index of refraction with other published data.

the author of this thesis is almost identical to that obtained by Adachi *et al*, with an RMS Error of 0.003. However, this data deviates from those of both Tanaka *et al* and Roberts *et al*, with RMS Errors of 0.047 and 0.036, both of which are well outside of the estimated uncertainty of ± 0.01.

It should be noted that the InGaP data provided by the author of this thesis is the average from three InGaP samples of different thicknesses, ranging from approximately 1800 Å to approximately 3500 Å. The different thickness samples allowed an excellent assessment of any potential correlation of the sample index of refraction with the thickness, which could result from an insufficient modeling approach. The largest absolute difference in the index of refraction of the three samples occurred in the vicinity of the band-gap. This difference was less than 0.005. In the longer wavelength regime, the maximum difference was less than 0.003. These results indicate that a measurable correlation between the modeled index of refraction and thickness does not exist.

The data of Roberts *et al* was obtained through reflection measurements. Oxide corrections were not applied in this analysis, and the measured index of refraction was based on an assumed index of refraction at 1000 nm, being given by interpolation of the binaries' (InP and GaP) optical constants. As such, the accuracy of the data obtained by Roberts is believed to be low. It is also generally accepted that the reflectivity technique is not as sensitive as ellipsometry, hence, more precise index of refraction measurements are obtained with ellipsometry [34, 54].

Tanaka *et al*'s indices are also based on reflection measurements. Oxide corrections were not applied, however, the samples were cleaned in a buffered HF solution prior to measurement. This approach has been shown to be inadequate due to the rapid reformation of the oxide. Experimental investigations using spectroscopic ellipsometry have shown that an oxide thickness of approximately 1 nm will be produced almost immediately upon

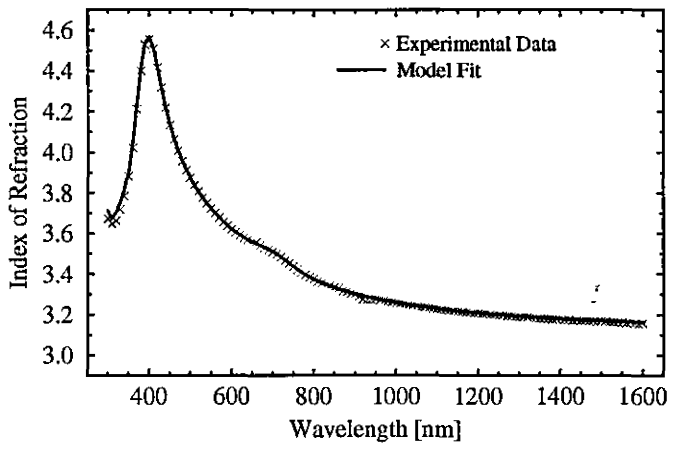

Figure 4.13: Experimental data and the results of the semiconductor parametric model fit.

exposure to air [51]. Secondly, only seven data points (for photon energies from 0.6-1.3 eV) were obtained for the InGaP sample, on which a single effective oscillator fit was performed. Therefore, the experimental uncertainty of the data provided by Tanaka *et al* is believed to be much larger than that reported in this thesis.

The optical constants of Adachi *et al* were determined by spectroscopic ellipsometry. The data from 1.2 eV to the InGaP band-edge were fit using a Sellmeier model, the results of which were plotted in Fig. 4.12.

Considering the above, poor agreement with the data of Roberts *et al* and Tanaka *et al* is not surprising, and the excellent agreement with the data obtained by Adachi is likely indicative of the absolute accuracy of both of these measurements.

Semiconductor Parametric Model Fitting

In order to demonstrate the effectiveness of the semiconductor parametric model's fitting capabilities, the index data for one of the InGaAsP samples (E_g in the vicinity of 1.77 eV) is provided in Fig. 4.13, along with the fit obtained using the model. As can be seen, and is indicated by the RMS error of 0.005, this physically realistic model is also very effective

at fitting the experimental data.

4.6.5 Uncertainties

The absolute uncertainty in the index data for photon energies below the band-gap has been estimated to be approximately ±0.01 (corresponding to one standard deviation). This uncertainty value is based on the observed change in the measured refractive index as a result of changes to model parameters, such as oxide index or thickness, and epitaxial layer thickness, as well as substrate optical constants. Also, the optical constants in the long wavelength regime were determined by fitting this region with functions known to be accurate at modeling the optical constants of semiconductors. Additionally, a parametric semiconductor model which is based on the band structure of semiconductors was also applied. This model derives its accuracy from fitting the absorption (ϵ_2) of the sample, from which the real and imaginary parts of the dielectric function are determined. Both of the above approaches yielded optical constants that were, in all cases, within ± 0.009 of each other.

4.7 SiO_xN_y Optical Constants

For the application of thin film dielectric interference filters on semiconductor laser facets, knowledge of the index of refraction of the dielectric film, as a function of wavelength, is required. The index of the ECR-PECVD deposited dielectrics is routinely measured at 632.8 nm, which is significantly different than the wavelengths at which a given filter is designed to operate. For the work discussed here, filters designed to operate in the same wavelength range as the InGaAsP lasers are required, namely from approximately 800 to 1000 nm.

The most important filter type is the antireflection coating, which is required to facilitate coupling of the light from the laser to the external cavity. The index of a single

layer antireflection coating, in the plane wave design, must be equal to the square root of the index of the substrate on which it is deposited. This means that films with indices around 1.85 are of particular importance. As such, a number of samples were analyzed in order to relate the index of refraction at the desired operating wavelength to that measured by the in-situ ellipsometer operating at 632.8 nm.

All SiO_xN_y samples were analyzed at angles of 65, 70 and 75 degrees, for wavelengths from 600 to 1600 nm, although data from 600 nm to 1000 nm was the main focus. Since InGaAsP/GaAs based lasers can operate in the range of 800 nm to 1000 nm, antireflection (and high reflectance) coatings are required for these wavelengths; hence the index of refraction of SiO_xN_y must be known in this range.

A Cauchy dispersion model (Eq. 4.11) was used to fit the experimental data over the above wavelength range. The optical constants of the silicon substrate were determined experimentally, following a procedure similar to the one described for the GaAs substrate. A two component model (three phase), consisting of the SiO_xN_y layer on Si was used for all analysis. The SiO_xN_y layers were assumed to be homogeneous, and non-absorbing, with planar and abrupt interfaces. The substrate was assumed to be semi-infinite in thickness.

Two SiO_xN_y samples with indices in the vicinity of the ideal AR coating were analyzed, and a simple linear interpolation of the two Cauchy parameters (A and B) derived from this analysis was performed, the results of which are used to relate the index of refraction (for AR coatings with indices in the range of 1.7 to 1.9), at a specific wavelength to that measured at 632.8 nm. These relationships are provided in Eqs. 4.17 and 4.18 below, where λ is in nm, and $n_{632.8}$ is the index of refraction measured at 632.8 nm.

$$A = 0.205 + 0.87(n_{632.8}) \tag{4.17}$$

$$B = -82000 + 52000(n_{632.8}) \tag{4.18}$$

Again, as a result of fit uncertainties of the two samples, interpolation validity and sys-

tematic errors, it is estimated that the uncertainty (standard deviation) is slightly below ± 0.01.

4.8 Chapter Summary

In this chapter, the optical constants of InGaAsP grown lattice matched to GaAs were provided for compositions ranging from GaAs to InGaP. This represents the first comprehensive study of the refractive index of this material system. These indices are necessary in order to design and optimize laser diodes based on this material system. Also, as will be discussed in more detail, the optical constants of the laser diode waveguide are required in the design of antireflection facet coatings, both aspects of which will be described in the following two chapters.

Chapter 5

Semiconductor Diode Lasers

Since the semiconductor diode laser is one of the key elements in the ultrashort-pulse laser system, a brief background on the design and practical realization of a diode laser will be provided. Particular attention will be paid to those properties which are most relevant to the short pulsed external cavity operation to be described in Chapter 7.

5.1 Diode Lasers: A Review

In a diode laser, the laser resonator is formed by the cleaved facets of the semiconductor material, which provide a reflectivity of about 30%. A population inversion, which is required to achieve gain and hence laser action, is achieved by the application of a forward bias to the 'pn' junction, which represents the 'heart' of the laser. The forward bias results in the injection of electrons and holes from the n and p sides of the junction respectively. These injected carriers may then be stimulated to recombine, resulting in laser action.

A variation of the above basic concept, known as the separate confinement heterostructure quantum well laser, is illustrated in Figure 5.1. In a simple single quantum well laser, the laser consists of three different materials.

1. Quantum well (E_{g-1})

2. Quantum barrier, or waveguide core (E_{g-2})

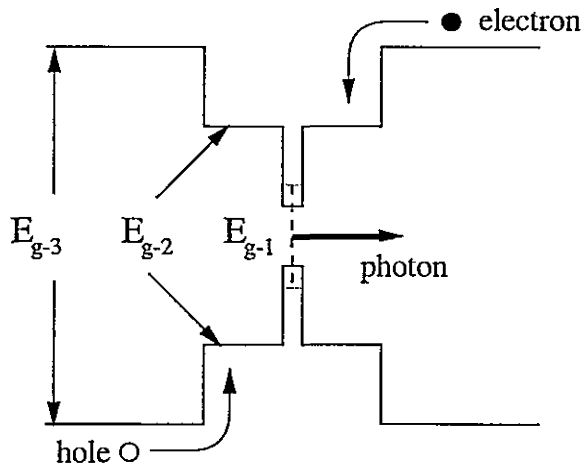

Figure 5.1: Simplified illustration of a quantum well laser.

3. Waveguide cladding (E_{g-3})

The smallest band-gap material is the quantum well, which is typically less than 100 Å in thickness. On either side of the quantum well is the barrier material or waveguide core material, which has a larger band-gap. The barrier or waveguide core material, as the two names suggest, has two primary functions. The first function is to provide confinement of the electrons and holes within the quantum well. The second function is to provide optical confinement, through the formation of a waveguide. The high index of refraction core of the waveguide consists of the small band-gap quantum well and barrier materials, and the lower index of refraction cladding layers are formed by the large band-gap (E_{g-3}) layers. Both optical and electronic confinement can be achieved with the same materials as a result of the very fortunate property that higher band-gap III-V semiconductors have lower indices of refraction.

5.2 GaAs based Lasers

Lasers designed for operation in the 800 nm to 1000 nm regime can be manufactured from two different material systems; AlGaAs/GaAs and InGaAsP/GaAs. All of the lasers described within this thesis are fabricated from the 'aluminum-free' InGaAsP system.

A number of researchers have been investigating the use of the InGaAsP as a replacement for the AlGaAs system [56, 14, 57, 58, 59]. Numerous advantages of InGaAsP over AlGaAs, such as reduced reactivity to oxygen [60] and higher electrical and thermal conductivity [61] have been cited. These advantages have lead some researchers to believe that higher power operation should be attainable in the InGaAsP system prior to the onset of catastrophic optical damage. The advantages of InGaAsP over AlGaAs will also prove relevant in this work, as future laser systems capable of higher output powers will be investigated. Additionally, as optical amplification schemes are investigated, higher thresholds to optical damage will become necessary.

5.2.1 Laser Design: Desired Properties

Prior to beginning the laser design process, the intended application and its impact on the required laser characteristics must be fully understood. The lasers described in this thesis were designed to be suitable for the generation of short optical pulses. This application imposes some of the same generic laser performance criteria as other applications, with the addition of some relatively unique criteria. The desired characteristics are outlined below.

- Low threshold current (and current density)
- High efficiency
- Large differential gain
- Low loss
- Small divergence angle
- Moderate output power

In general, all lasers benefit from high efficiency and low threshold current, as well as low loss. This is also true for the application of lasers to the generation of short optical

pulses. Since all three of these criteria are readily obtained in quantum well lasers, this is the laser structure of choice. Quantum well lasers also provide the added benefit of flexibility associated with different quantum well materials and thicknesses, such that a broad range of wavelengths are accessible. In terms of tailoring the accessible operating wavelength range, quantum well lasers have great potential, as will be discussed in Chapter 7.

Since the lasers used in this work are mounted in an external cavity, a small output divergence angle (far field) is also very important. This improves the coupling efficiency of the field from the laser to the external cavity, as well as the inverse, from the external cavity back into the laser. In the second case, a large waveguide active region is also beneficial, provided this is not done at the expense of the far-field angle.

In two of the three possible 'mode-locking' configurations (Chapter 7) both an rf current and a dc current are applied to the laser. Since the peak of the rf current is large, both high efficiency and low threshold are important. High frequency operation of diode lasers can also benefit greatly from high differential gain. In general, a high differential gain leads to a high modulation response, as well as more stable laser operation. The high modulation response allows efficient coupling of the high frequency source to the laser.

GaAs Laser Designs

Initial designs of 980 nm lasers, which have received significant attention in recent years, were based on the three materials: InGaP, GaAs and InGaAs. A typical design of such a laser, as provided through illustration of the conduction band, is shown in Figure 5.2. The InGaAs quantum well layer is compressively strained, as a result of the In concentration, which is approximately 20%. The addition of In is required to lower the band-gap in order to provide a quantum well energy level transition at 980 nm. GaAs acts as both the barrier material, used to provide electron confinement in the quantum wells, as well as the waveguide core, providing optical confinement between the InGaP cladding layers. For

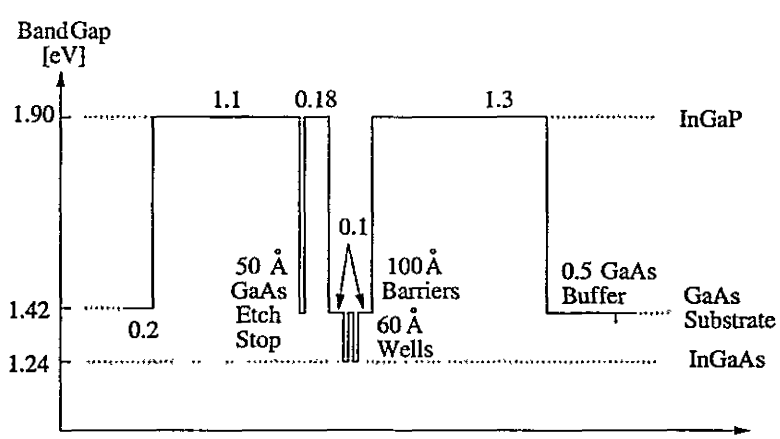

Figure 5.2: Energy band diagram of a 980 nm InGaAs/GaAs/InGaP laser.

reasons related to these roles, lasers utilizing a GaAs waveguide core are not ideal.

The effectiveness of a particular layer, from the perspective of electron/hole confinement, can be assessed by analysis of the energy gap difference between the barrier material and the well transition energy. For a λ=980 nm (E_g=1.265 eV) quantum well, and the E_g=1.42 eV GaAs, a difference of 155 meV is obtained. Assuming a band gap offset of 40:60 [1](i.e. $\Delta E_c = 0.4 \times \Delta E$, $\Delta E_v = 0.6 \times \Delta E$) results in an electron confinement of 62 meV, or 2.5×kT. This confinement is weak, and will result in poor temperature and high power performance, as has been observed in this work, as well as in the work of others [65, 66].

The other role played by the GaAs is that of optical confinement [2]. As a result of the large index contrast between GaAs and InGaP, the optical mode will be tightly confined to the GaAs core. From the perspective of high power operation, whereby facet damage occurs as a result of high power density, such a device would suffer premature failure, provided such high power levels were even achievable given the electron/hole confinement limitations discussed above. A third consequence of the high index contrast is the onset of multimode

[1]The band-gap offset of the InGaAsP/GaAs system is currently not very well known. Therefore, 40:60, which represents an intermediate value within those that have been reported [62, 63, 64], was assumed.

[2]A summary (with references) of the waveguide problem is provided in Appendix A.

operation. The maximum thickness for which single mode operation may still be achieved will be considerably smaller than that of other more ideal designs.

Finally, as a result of the desired low output divergence angle, such that coupling to an external cavity can be made as efficient as possible, this device design is further limited. Reasonable divergence angles can be achieved provided the active region is made extremely thin (600 Å), which is undesirable, both from the perspective of coupling to an external cavity and that of threshold current and optical loss. As a result of the limitations of the use of GaAs as both the optical and electrical confinement material, the InGaAsP material system was explored.

InGaAsP Laser Designs

Due to the freedom in selection of the band-gap and hence the index of refraction of InGaAsP by the appropriate choice of composition, optimization of the waveguide core to effectively alleviate the problems described above is possible. To this end, computer code was written by the author to perform both the waveguide and far-field analysis.

In Figure 5.3, the basic features of an InGaAsP/GaAs ridge waveguide laser, such as those used in this work, are illustrated[3]. Lasers were made with ridge widths (w) in the range of 2 to 5 μm. The ridge height (h_R) is usually about 1 μm, but may be slightly larger. The SiO_2 dielectric layer, which provides electrical isolation between the p-metal layer and the semiconductor surface, is approximately 1000 Å thick. The distance between the top of the waveguide and the etch stop which is labeled d_c in the above figure, is usually in the vicinity 0.2 μm.

The waveguide core can range in thickness from anywhere between about 800 Å up to greater than 1 μm. Usually, thin waveguide designs are employed where a large index contrast between the core and the cladding exists, such that reduction of the output

[3]A summary of the laser processing procedure is provided in Appendix B.

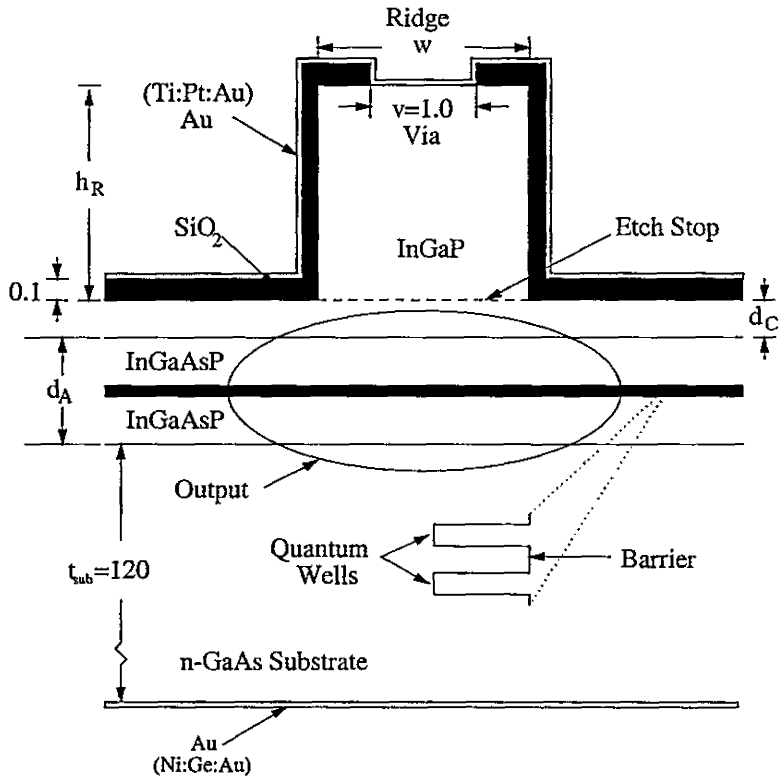

Figure 5.3: Cross-sectional (facet) view of a ridge waveguide laser.

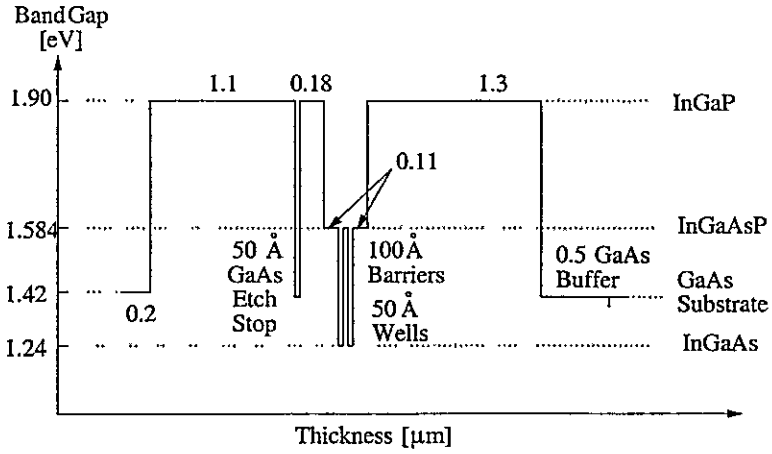

Figure 5.4: Improved 980 nm diode laser, utilizing InGaAsP.

divergence can be obtained. The larger waveguide cores are employed mainly in high power operation [58, 61], where the maximum output power is limited by facet damage. Since facet damage is dependent on the field density, increasing the waveguide core, for fixed intensity, decreases the field density, and hence increases the damage threshold.

Lasers which were investigated in this work contained two quantum wells. As will be described in a later section, lasers with two quantum wells with different transition energies resulting from different well compositions, were also fabricated.

Utilizing the above described laser design tools, a number of different 980 nm lasers were designed and tested, one of which is illustrated in Figure 5.4. Lasers with ridge widths of 4 μm and lengths of 500 μm had threshold currents ranging from 12 mA to about 25 mA, and differential quantum efficiencies in the 0.6 to 0.7 W/A range. These values are comparable to those obtained by others [67]. It should also be noted that performance improvements are expected from a more detailed growth optimization analysis. Growth parameters, such as temperature for the different layers and layer transition interruption times, as well as slight doping level adjustments can result in noticeable performance improvements.

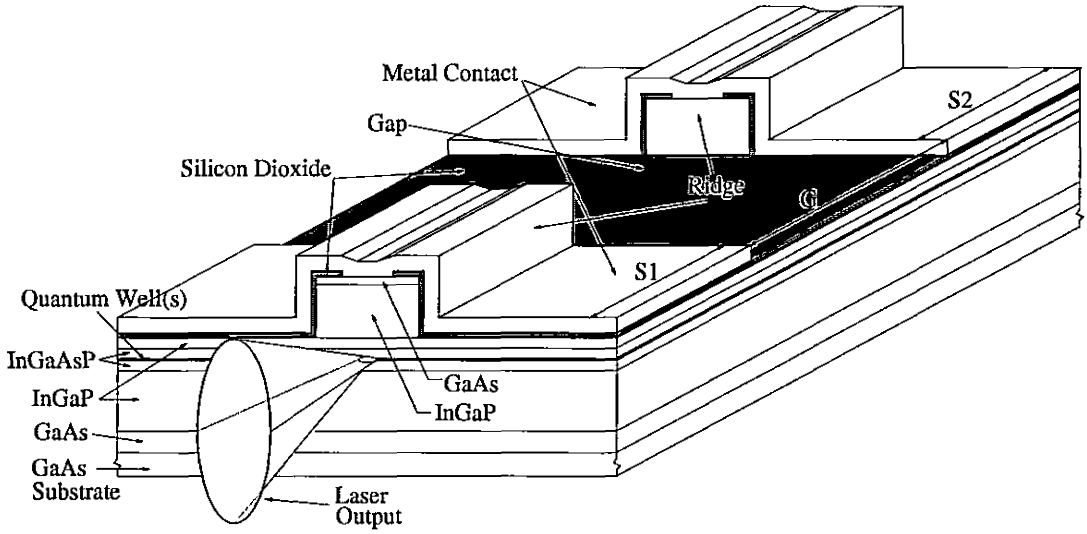

Figure 5.5: Split contact ridge waveguide laser.

5.3 Multi-electrode Devices

Lasers with two electrically isolated contacts can be used to passively mode-lock a diode laser, resulting in the emission of short optical pulses. These 'split contact' devices are also employed in a hybrid mode-locking configuration, whereby gain is provided by one section, and pulse shaping is achieved in the other section. The property of the split contact device which is useful in the above applications is that of saturable absorption, which can be obtained in sections biased below threshold. The saturable nature of the split contact devices will be described in more detail in Chapter 7, and only the relevant design aspects of the device will be discussed here.

A schematic of a split contact laser is provided in Figure 5.5. With respect to the standard ridge waveguide laser discussed previously, the split contact device is very similar, differing only in the gap which is etched through the ridge. The metallization is then applied to only the area with a ridge, and not to the gap region. This provides the ability to control the bias of each section separately. The design of split contact devices thus requires more care in the determination of the optimal waveguide structure, as well as

the optimal dimensions for the gap length and depth.

Multi-electrode Laser: Design Issues

Since a negative bias may be applied to one of the sections, namely the absorber section, a large resistance between the two contacts is desirable. This can be achieved by either increasing the gap length or by reducing the thickness and doping level of the material below the etch stop and above the waveguide core material. Increasing the gap length results in a decrease in the optical coupling between the two sections, which effectively contributes an additional loss to the laser. The effect of the gap length on the optical coupling was studied using a beam propagation method (BPM) software package, as well as by direct experimentation.

For a fixed gap length, the extent of the gap loss is dependent on the waveguide structure as well as the proximity of the waveguide core to the etch stop. The distance from the edge of the waveguide to the etch stop, which is given by d_c, is illustrated in Fig. 5.3. As d_c increases, the gap loss decreases. However, since the waveguide core is undoped, conduction between the two sections is dominated by the thickness and conductivity of the InGaP material between the etch stop and the waveguide core. Hence increasing d_c results in a decrease in the gap resistance.

The optical loss associated with the gap is also dependent on the confinement of the mode by the waveguide. If the mode is tightly confined to the waveguide core as a result of the index contrast between the core and cladding, removal of part of the cladding may result in a significant change in the modal profile, and hence a large effective loss.

Determination of the optimal value for d_c thus requires an assessment of the impact of d_c on three very important characteristics.

1. Electrical isolation between the sections

2. Optical confinement provided by the laser ridge

3. Optical loss associated with the gap

Reducing d_c results in a larger gap resistance, as well as a larger difference in the effective indices below and beside the ridge. This produces stronger lateral optical confinement. However, with stronger confinement comes a reduction in the ridge width at which single spatial mode operation is maintained. Also, as d_c is reduced, the gap loss is increased. Consideration of these effects must be included in the design of a split contact device.

To provide more flexibility in the design of such split contact lasers, additional etch stops [4] could be grown into the InGaP layer. This would allow the gap to be defined *independently* from the ridge. In this way, the impact of the split contact gap could be completely decoupled from the waveguiding provided by the ridge. Although this procedure requires additional processing steps, future optimization of these lasers will incorporate this dual etching technique.

5.4 Chapter Summary

Based on the material characterization and optimization described in Chapter 2 and the InGaAsP/GaAs optical constants provided in Chapter 4, low threshold, efficient diode lasers with moderate divergence angles were designed and fabricated. After the application of a high quality antireflection coating to the diode laser's facet, the primary component of the ultrashort-pulse external-cavity laser system is complete. In the next chapter, antireflection coatings on the facets of these InGaAsP/GaAs based lasers will be described.

[4] A brief summary of the laser processing procedure used in this work is given in Appendix B.

Chapter 6

Diode Laser Facet Coatings

High quality antireflection facet coatings are required for the ultrashort-pulsed external-cavity diode laser system, as has been outlined in previous chapters. In this chapter, the design and fabrication of such coatings will be discussed, along with the experimental techniques used to evaluate the facet reflectivity.

Thin dielectric filters which are applied to a diode laser's facet(s) can result in a significant modification in the operating characteristics of the laser compared to the characteristics of the uncoated device. Parameters such as efficiency, output power, wavelength tunability, reliability and spectral properties can be significantly altered by the application of a relatively simple facet coating. For example, the application of an AR (few %) and HR (>90%) coating to opposite facets can greatly reduce the threshold and increase the usable output power of a device. In the case of very low reflectivities, it has been shown that lasing can be completely suppressed.

Of central interest to the goals of this research is the antireflection coating, which is necessary to allow strong optical coupling of the diode laser to an external cavity. From many perspectives, the AR coating can be viewed as an enabling technology, without which accomplishing the goals of this thesis would not be possible. As outlined in this chapter, although the AR coating is simple in principle, achieving reflectivities in the low 10^{-4} range or better is a non-trivial task, particularly on laser facets.

The application of a high quality AR coating ($R<10^{-3}$) to a diode laser facet can produce a superluminescent diode (SLD) as a result of a suppression of laser oscillations, due to the increased loss associated with the coated facet. When both facets are coated in order to obtain low reflectivities, the laser diode can be transformed into a semiconductor optical amplifier (SOA). Fabrication and implementation of semiconductor optical amplifiers is another area of relatively intense research, once again focussed on the telecommunications industry. In this context, development of high quality antireflection coating fabrication and characterization capabilities is highly relevant to emerging technologies.

6.1 Evaluation of Antireflection Coatings

To evaluate the suitability of a coated device for the above operating regimes, the reflectivity of the coated facet must be determined. The ideal method used to evaluate the reflectivity is strongly dependent on the order of magnitude of the reflectivity itself. Reflectivities at or above approximately 2×10^{-3}, where the device still lases and the threshold has not increased by more than about a factor of two, can be evaluated with reasonable accuracy by measurement of the ratio of the power emitted from the two facets, when the laser is operated above threshold. The ratio of the power out of the left facet, P^- to that out of the right facet, P^+ is a function of the reflectivities of the left and right facets, R^- and R^+, respectively. This ratio is given in Eq. 6.1 [68].

$$\frac{P^+}{P^-} = \sqrt{\frac{R^-}{R^+}}\left(\frac{1-R^+}{1-R^-}\right) \tag{6.1}$$

From Eq. 6.1, the reflectivity of the coated facet can be determined, provided the reflectivity of the uncoated facet is known. As is discussed in Section 6.2, accurate assessment of the reflectivity of the cleaved facet is non-trivial. However, most III-V laser devices have facet reflectivities in the 0.25 to 0.35 range, depending on their operating wavelength and waveguide structure.

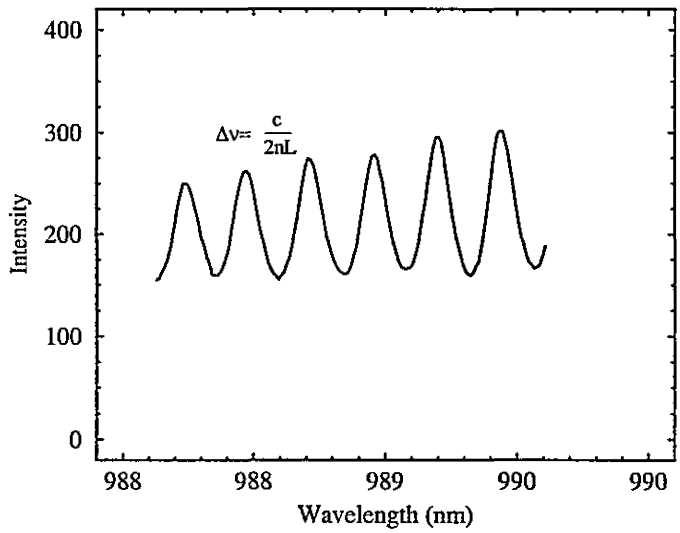

Figure 6.1: Fabry-Perot modes of a diode laser.

For coatings with reflectivities lower than 10^{-3}, which normally prevent the device from lasing, a different measurement technique must be applied to determine the reflectivity of the coated facet. This second technique is based on a well known method developed to measure the gain of a diode laser, which relies on measurement of the spontaneous emission below threshold . The original technique, to be referred to as the HP method, was described by Hakki and Paoli [69]. A modified version of the above technique was later described by Cassidy [70] which is referred to as the DTC method. A clear explanation of these techniques is aided by reference to Fig. 6.1.

In the Fabry-Perot model of a diode laser, the steady-state output intensity $I_1(\nu)$ at a frequency ν, from facet #1 is given by [70].

$$I_1(\nu) = \frac{B(1 + R_2G(\nu))(1 - R_1)}{(1 - \sqrt{R_1R_2}G(\nu))^2 + 4\sqrt{R_1R_2}G(\nu)\sin^2(kL)} \tag{6.2}$$

where R_1 and R_2 are the reflectivities of facet #1 and #2 respectively and $G(\nu)$ is the single pass intensity gain at a frequency ν. (It should be noted that G is a function of, among other things, current and temperature.) The ratio of the maximum to the minimum

intensity, denoted by h, is given in Eq. 6.3.

$$h = \frac{I_{max}}{I_{min}} = \frac{(1+\sqrt{R_1 R_2}G)^2}{(1-\sqrt{R_1 R_2}G)^2} \tag{6.3}$$

In Fig. 6.1 an example of the amplified spontaneous emission described by Eq. 6.2 is provided, which illustrates the modulation of the spontaneous emission and hence the maximum and minimum intensities.

Using the above relationship, the single pass gain can be determined for a given facet reflectivity. Provided the indices of the laser materials are known, the cleaved facet reflectivity, R (R=$\sqrt{R_1 R_2}$), can be calculated. From measurement of the amplified spontaneous emission (ASE) of the device before coating, the reflectivity of the coated facet, R′, (which will be either R_1 or R_2 above) can then be determined by measurement of the coated lasers intensity ratio, h′. For operation at identical drive currents and temperatures, the coated facet reflectivity becomes a function of h, h′ and R only.

6.2 Design of Diode Laser AR Coatings

In the case of plane wave illumination of a substrate with index of refraction, n_s, an antireflection coating's index, n_f, and thickness, t_f must satisfy Eqs. 6.4 and 6.5 respectively, as was also described in Chapter 3.

$$n_f = \sqrt{n_s} \tag{6.4}$$

$$t_f = \frac{\lambda}{4n_f} \tag{6.5}$$

For the application of a coating on a laser facet, the above situation does not rigorously apply. In this case, the divergent nature of the elliptical beam emitted from the waveguide structure must be considered. Figure 6.2 illustrates this situation, where the waveguide core and cladding index of refraction are given by n_A and n_C, respectively. The core thickness is d_A, and n_f and t_f are the index and thickness of the coating, respectively. The coating properties must be such that the total field reflection from the interface between

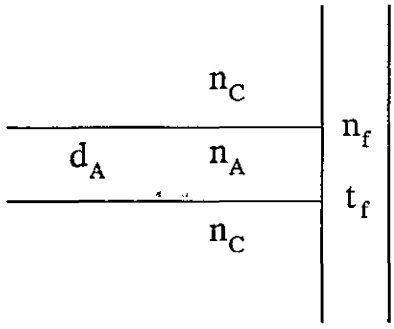

Figure 6.2: Dielectric layer deposited on the facet of a diode laser.

the waveguide and the film, and the film and air, *coupled back into the mode*, equals zero. This is the antireflection criterion.

A rigorous description of the reflection at the waveguide facet requires a full three dimensional solution of Maxwell's equations at this boundary. To make this problem more tractable, numerous assumptions and simplifications regarding the exact laser structure and its properties are made.

The first approximation concerns the guiding conditions of the waveguide. Since the mode is typically more strongly guided in the direction perpendicular to the plane of the junction (y direction in Fig. A.1, in Appendix A), guiding in the plane of the junction is neglected. This assumption, which reduces the problem to two dimensions (y and z), is often valid, particularly for ridge waveguide structures.

A complete discussion of this situation is presented in the works of Vassallo [71, 72, 73] as well as those of others [74, 75, 76]. In reference [71], an approximate method, based on the simplified two dimensional structure described above, is provided for the solution of the reflectivity of a diode laser facet containing any number of dielectric layers. This solution was shown to be sufficiently accurate for the design and evaluation of realistic antireflection coatings. The error in such a calculation is approximately 1×10^{-5}, which, as will be discussed in Section 6.3, is below the reflectivity which can be obtained in practice.

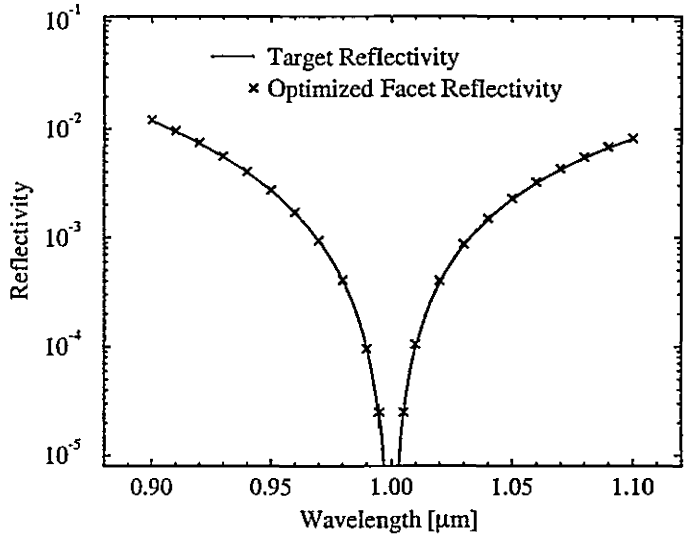

Figure 6.3: Demonstration of the modal reflectivity calculation and optimization.

It is this approximate technique which has been used to calculate the reflectivity of both coated and uncoated diode laser facets presented in this thesis.

In order to perform the calculations based on the approximate method, a computer program was written [77] which determines the reflectivity of an arbitrary coating on a user defined waveguide structure. This program can also compare the calculated facet reflectivity profile to a user-defined plane-wave-based reflectivity profile. The facet coating thickness and index can then be iterated until an error term, representing the difference between the two profiles, is minimized. This allows a simple plane wave filter to be designed, with a reflectivity profile that could be duplicated on a laser facet through modification of the 'on facet' filter's index of refraction and thickness.

A demonstration of this optimization process is presented in Fig. 6.3. In this figure, the reflectivity of a plane wave AR coating, designed for operation at 1000 nm and deposited on a substrate with an index given by Eq. 6.6, is illustrated.

$$n_{sub} = \frac{n_{clad} + n_{core}}{2} \tag{6.6}$$

The cladding index, n_{clad}, is 3.23 and the core index, n_{core} is 3.35. Also illustrated in Fig. 6.3 is the facet reflectivity of the *optimized* coating applied to the laser structure with a 0.2 μm waveguide core, with core and cladding indices given above. The properties of these films are provided in Table 6.1. As is clearly illustrated in Fig. 6.3, the reflectivity

Film	t [Å]	n_f
Target	1378	1.814
Optimized	1424	1.803

Table 6.1: Properties of the films illustrated in Fig. 6.3.

profile of a plane wave designed filter can be obtained on a laser facet, through appropriate modification the filter's index and thickness.

Now that the ability to optimize a given film's properties to obtain the desired reflectivity profile has been demonstrated, the 'need' for such an optimization procedure should be illustrated. To this end, the modal reflectivity of the films given in Table 6.1, for the waveguide structure described above, is provided in Fig. 6.4.

In Fig. 6.3 the reflectivity profile for the 'target' reflectivity structure, corresponds to plane wave illumination. In Fig. 6.4, it is the modal reflectivity profile obtained for deposition on the waveguide structure described above. As is clearly illustrated in Fig. 6.4, the structure of the waveguide must be accounted for in order to obtain a reflectivity of less than 10^{-3}.

To further the discussion, one could imagine that a more intelligent choice of the 'substrate' index from which to base the plane wave model could be selected. The most obvious choice would be the effective index (n_{eff}), determined from the solution of the guiding conditions of the waveguide. For the waveguide structure above, this index is 3.255, which would then require a film thickness and index of 1386 Å and 1.804 respectively,

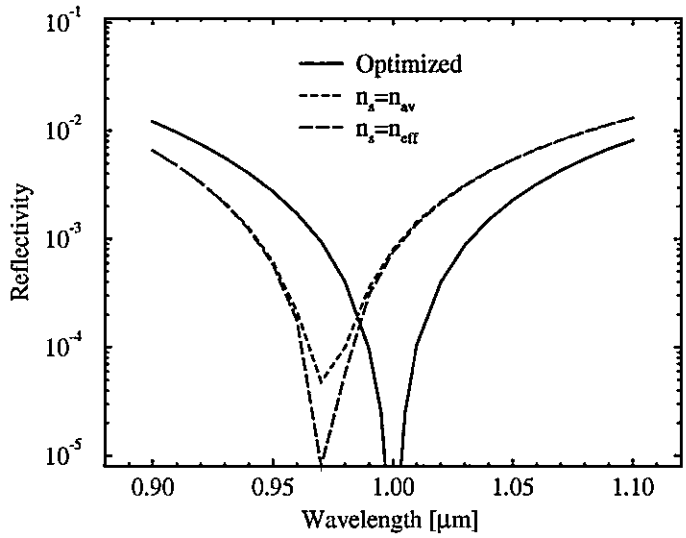

Figure 6.4: Modal reflectivity of different 'effective' substrates for a plane wave analysis.

based on plane wave illumination. The modal reflectivity of this filter is also illustrated in Fig. 6.4. Once again, it is clear that the plane wave model is inadequate in determining the parameters necessary to achieve facet reflectivities below approximately 10^{-3}. The parameters of the three coatings illustrated in Fig. 6.4 are provided in Table 6.2.

Film	t [Å]	n_f
Optimized	1424	1.803
Effective Index	1378	1.814
Average Index	1386	1.804

Table 6.2: Properties of the films illustrated in Fig. 6.4.

6.3 Experimental Interference Filters

Through the application of the approximate method for the calculation of the modal reflectivity and the experimental index of refraction data (Chapter 4), high quality antireflection

coatings could be designed for the InGaAsP lasers described in Chapter 5. Employing the optimized deposition parameters outlined in Chapter 3 to deposit the desired thin films allowed state of the art reflectivities, as low as 1-2 $\times 10^{-4}$ to be achieved. Reflectivities in the mid to low 10^{-4} can be routinely achieved on a variety of different laser structures.

6.3.1 Experimental Implementation

For quantum well lasers, as used in this work, the operating wavelength is such that the waveguide core and cladding layers are transparent. This makes assignment of the optical constants to these layers relatively easy, provided the optical constant data exists. However, assigning an appropriate index of refraction to the quantum wells is a much more complicated task. The approach used in this work to account for the quantum wells is described below.

The quantum wells provide gain when current is injected into the laser. This gain is given by the imaginary part of the complex index of refraction, k(E). Through the Kramers-Kronig relations, any change in the extinction coefficient, k(E), must be accompanied by a change in the index of refraction, n(E). Since the gain in the laser is a function of current, both the real and imaginary parts of the index of refraction are also functions of current. Modeling of the optical constants of the quantum wells thus becomes very complicated, and as such, approximate methods would be preferred compared to a full rigorous description [1]. Since the method which is used to determine the optimal antireflection coating properties is based on a simple three layer slab waveguide, approximation of the real structure by a three layer structure must be performed.

In this work, the index of refraction of the quantum wells was determined by a simple interpolation between the end point binaries of InGaAs (InAs and GaAs) as given in [53]. Gain and absorption in the quantum wells were neglected. Three approaches were

[1] More importantly, based on the uncertainties of the complex index of refraction of an operating laser, a full rigorous analysis remains impractical.

then used to approximate the real laser structure by that of a three layer slab waveguide.

- Case #1: In the first approach the quantum wells' optical constants are assumed to be identical to those of the surrounding material (i.e., the wells are essentially neglected, except for their contribution to the total waveguide core thickness).

- Case#2: In the second approach, an average core index of refraction was calculated based on a weighting of the relevant indices by the corresponding layer thickness.

- Case #3: In the third approach (case #3), the effective index of the complete waveguide structure, including the quantum wells, was first calculated. The index of refraction of a single layer material, *which would produce the same effective index as the complete structure*, was determined. This index was then used as the waveguide core index. The optical constants of the quantum wells used in the calculation of the complete structure were calculated from the optical constants of the two binary constituents.

In Table 6.3, the resultant waveguide core index and the effective index, as well as the index and thickness of the optimized AR coating, are provided. The modal reflectivities of the

Case	n_A	n_{eff}	n_f	t_f Å
#1	3.368	3.260	1.813	1446
#2	3.375	3.264	1.820	1444
#3	3.390	3.274	1.825	1448

Table 6.3: Waveguide modeling assumptions and the required antireflection parameters.

three coatings given in Table 6.3 are illustrated in Fig. 6.5.

To assess the impact of the above assumptions, it is useful to compare the experimental uncertainties in the various thin film properties, as well as the semiconductor optical

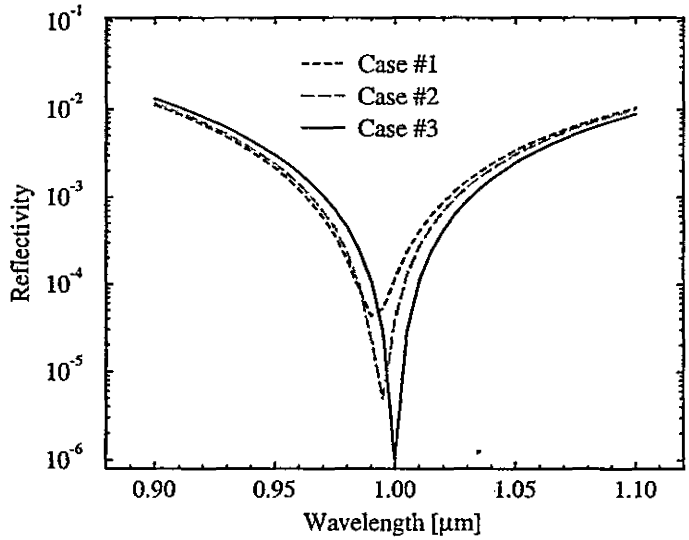

Figure 6.5: Modal reflectivity of the three filters given in Table 6.3, when deposited on the facet of the waveguide structure in Case #3.

constants, to the differences in the waveguide modeling approach parameters, and the resultant optimal AR coating parameters. The experimental uncertainties, and the impact of these uncertainties on the calculated modal reflectivities, are provided in Table 6.4. The

Parameter	Uncertainty	R $\times 10^{-5}$
n_A	± 0.01	2.5
n_C	± 0.01	1.5
n_f	± 0.01	8
t_f	± 25	35

Table 6.4: Effect of experimental uncertainty on modal reflectivity.

uncertainties for each parameter are provided in the table. It should be noted that the uncertainties for the thin film parameters are different from those given previously in Chapter 3. The values provided previously were those based on the ellipsometer measurements. In the deposition of facet coatings, the ellipsometer measurement is performed on a silicon

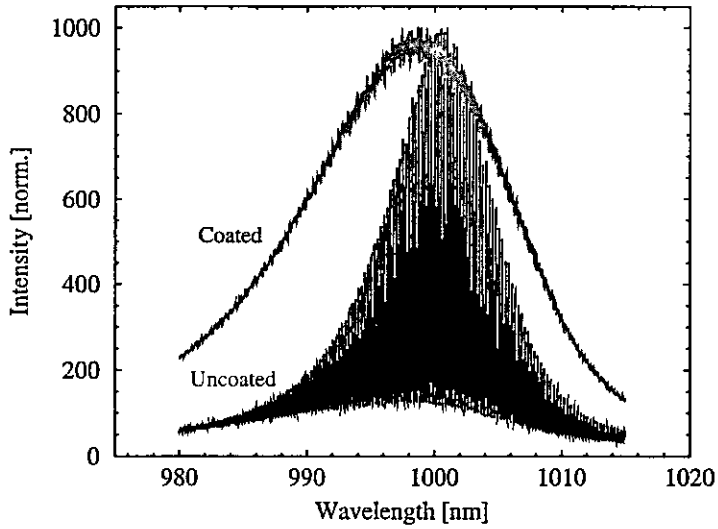

Figure 6.6: Amplified spontaneous emission before and after the application of an antireflection coating.

witness sample. As a result, an added uncertainty based on both the different substrate material and the physical location within the chamber must be included.

From Table 6.4, it can be seen that based on the experimental uncertainties, the thickness of the thin film, and to a lesser extent, its index, have the largest impact on the uncertainty in the resultant modal reflectivity.

6.3.2 AR Coated Facet

An example of the amplified spontaneous emission obtained from an InGaAsP/GaAs laser described in Chapter 5, before and after coating is provided in Fig. 6.6. These spectra were obtained at the same current and temperature. Application of both the HP and DTC methods described above yielded essentially identical reflectivity profiles. The results from the HP analysis are illustrated in Fig. 6.7, demonstrating that very low facet reflectivities can be achieved by the application of a single SiO_xN_y layer deposited by ECR-PECVD.

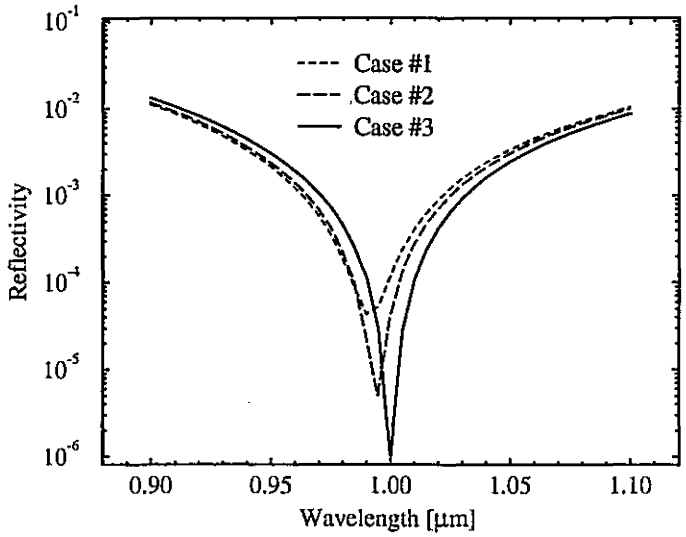

Figure 6.5: Modal reflectivity of the three filters given in Table 6.3, when deposited on the facet of the waveguide structure in Case #3.

constants, to the differences in the waveguide modeling approach parameters, and the resultant optimal AR coating parameters. The experimental uncertainties, and the impact of these uncertainties on the calculated modal reflectivities, are provided in Table 6.4. The

Parameter	Uncertainty	R $\times 10^{-5}$
n_A	± 0.01	2.5
n_C	± 0.01	1.5
n_f	± 0.01	8
t_f	± 25	35

Table 6.4: Effect of experimental uncertainty on modal reflectivity.

uncertainties for each parameter are provided in the table. It should be noted that the uncertainties for the thin film parameters are different from those given previously in Chapter 3. The values provided previously were those based on the ellipsometer measurements. In the deposition of facet coatings, the ellipsometer measurement is performed on a silicon

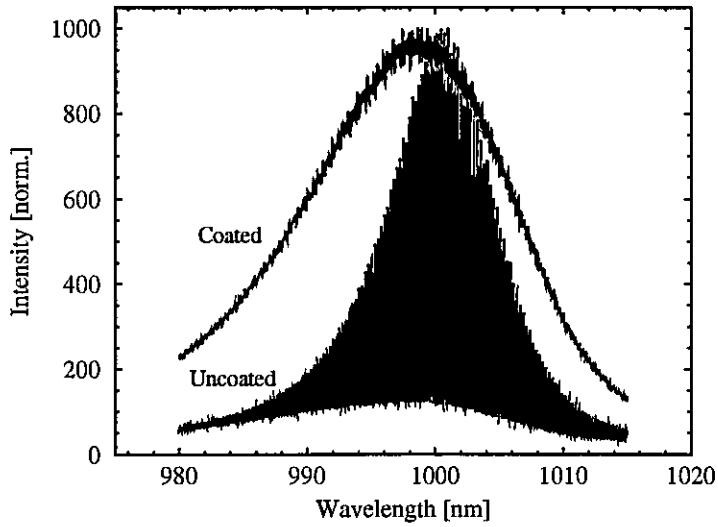

Figure 6.6: Amplified spontaneous emission before and after the application of an antireflection coating.

witness sample. As a result, an added uncertainty based on both the different substrate material and the physical location within the chamber must be included.

From Table 6.4, it can be seen that based on the experimental uncertainties, the thickness of the thin film, and to a lesser extent, its index, have the largest impact on the uncertainty in the resultant modal reflectivity.

6.3.2 AR Coated Facet

An example of the amplified spontaneous emission obtained from an InGaAsP/GaAs laser described in Chapter 5, before and after coating is provided in Fig. 6.6. These spectra were obtained at the same current and temperature. Application of both the HP and DTC methods described above yielded essentially identical reflectivity profiles. The results from the HP analysis are illustrated in Fig. 6.7, demonstrating that very low facet reflectivities can be achieved by the application of a single SiO_xN_y layer deposited by ECR-PECVD.

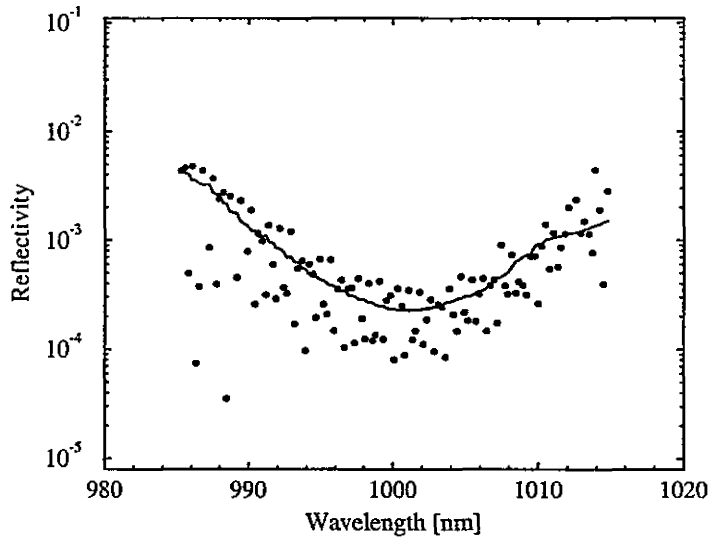

Figure 6.7: Calculated reflectivity profile obtained from analysis of the ASE in Fig. 6.6.

6.3.3 Practical Limitations

Extremely low reflectivities on the order of 10^{-6} have been reported [78], without a realistic assessment of the relevant uncertainties, and their impact on the determination of such a low reflectivity. To obtain reflectivities in the low 10^{-4} range, control over the index of refraction to within ± 0.02 and thickness to within ± 20 Å is required. Obtaining this control is non-trivial from a practical perspective, however, it is achievable.

Using only the plane wave reflectivity model, and assuming that the substrate index is known exactly, a reflectivity in the order of 10^{-6} requires a precision of better than ± 0.002 in the index of refraction, and ± 5 Å for the film thickness. This clearly demonstrates that achieving reflectivities of 10^{-6}, even for plane wave illumination, is extremely difficult.

The discussion on practical reflectivities becomes more complicated for deposition on laser facets, where the index of the laser materials must also be known precisely to achieve such low reflectivities. In the cold cavity approximation (no gain), absolute accuracy of the laser material's index of refraction on the order of ± 0.01 is realistic. Determination of the

appropriate optical constants of an operating laser is further complicated by the injection of carriers, which can have a significant effect on both the real and imaginary part of the index of refraction [49]. Current injection can result in changes of 0.01 or greater. Under some conditions, the change in index has been reported to approach 0.1. An error in the index of refraction of the waveguide core only, of a value of ± 0.02, results in a calculated reflectivity of approximately 5×10^{-5}. This suggests that reports of reflectivities into the 10^{-6} range are very likely exaggerated.

One explanation for the determination of such low reflectivities lies in the method used to evaluate the reflectivity. As described in [79, 80], a method which requires measurement of the modulation depth of the coated device only, operated at the uncoated devices threshold current, has been used. From the assumption of an infinite modulation ratio (h) of the uncoated device, the coated device's reflectivity, R', can be written as

$$R' = a^2 R \tag{6.7}$$

where R is the reflectivity of the cleaved facet, and the amplification factor for the coated device, a, is related to the modulation depth, h', by Eq. 6.8.

$$\frac{h'-1}{h'+1} = \frac{2|a|}{1+|a|^2} \tag{6.8}$$

Analysis of our AR coatings using the above technique results in reflectivities as much as 5 times lower than those calculated using the HP and DTC methods.

Based on the above discussion, it is the author's opinion that the practical limit for the minimum obtainable facet reflectivity is in the low to mid 10^{-5} range. This view is supported by others [72].

6.4 Chapter Summary

In summary, antireflection coatings have been deposited on the facets of InGaAsP/GaAs based diode lasers, resulting in residual reflectivities of approximately 1-2$\times$ 10^{-4}. The facet

coating designs were based on the approximate modal reflectivity calculations described in [71], where the modal reflectivity is dependent on the waveguide parameters, including the optical constants. The optical constants of the laser structure, which are required inputs for the modal reflectivity model, were based on the data provided in Chapter 4.

Chapter 7

External Cavity Short Pulse Operation

The focus of this chapter is the operation of AR coated diode lasers in an external cavity, particularly when operated in a regime where the output consists of a train of ultra-short optical pulses. The design and implementation of such a laser system is made possible by the ground work described in the previous chapters. In particular, the design and fabrication of the InGaAsP/GaAs diode lasers and the demonstration of high quality antireflection facet coatings have made this part of the project feasible.

Prior to a discussion on the laser system, the tunability of a number of AR coated diode lasers and in particular, the use of an asymmetric multiple quantum well structure will be described. In the context of a novel combination of the above two phenomena (short pulses and wavelength tunability via the use of an asymmetric quantum well structure) wavelength-tunable short-optical-pulses [81], and the excellent future prospects of such systems, will be described.

7.1 Wavelength Tunable External Cavity Operation

It is well known, and has been demonstrated in a number of different laboratories [82, 83] that diode lasers, when operated in an external cavity, can be forced to operate over a large

wavelength range. This is a direct result of the large gain bandwidth inherent to diode lasers. This wavelength tuning is most often achieved through the use of a wavelength selective feedback element, such as a diffraction grating. The absolute maximum tuning range of an uncoated diode laser is determined by the gain bandwidth. The application of an antireflection coating, however, can result in an increase in the wavelength range over which the laser can be operated in practice. This is due to an increase in the ratio of the feedback from the wavelength selective diffraction grating, to the cleaved facet feedback, which is inherently non-wavelength selective. A standard [1], uncoated, two-quantum-well laser with feedback from a 1200 line/mm diffraction grating was tuned over a wavelength range of approximately 17 nm. The application of an antireflection coating with a reflectivity in the low 10^{-4} range provided a tuning range in excess of 60 nm [84].

The maximum tuning range can be further enhanced by proper design of the laser's active region, to achieve a larger gain bandwidth. This can be accomplished through the use of an asymmetric quantum well structure [85, 86], which contains at least two quantum wells with different transition energies. In such a structure, the two quantum wells can be made from materials with different compositions [84], or the two wells may be of different thicknesses [87]. Each of these approaches results in a broadened gain spectrum because of the two different quantum well transition energies.

An example of the PL spectra (which is related to the gain) of an asymmetric quantum well structure is illustrated in Fig. 7.1. This structure consisted of two quantum wells with slightly different compositions. The individual contribution from each of these wells is clearly distinguishable. When a laser containing such an asymmetric two quantum well structure was placed in the same external cavity as that of the standard quantum well laser, it was found that a tuning range of 36 nm and 82 nm, for the uncoated and coated

[1] A standard laser refers to a typical diode laser as described in Chapter 5, which contains two identical quantum wells.

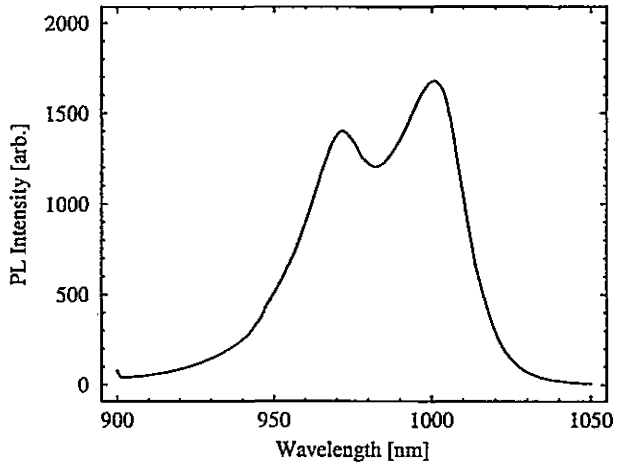

Figure 7.1: Photoluminescence from an asymmetric dual quantum well laser's active region.

devices, was achieved [84]. This represents a significant improvement in the tunability as a result of the enhanced gain bandwidth. The additional tuning ranging provided by the AR coating is also quite dramatic.

With respect to short pulse generation, the minimum pulse duration that can be achieved is inversely proportional to the bandwidth of the pulse. As such, asymmetric quantum well structures would appear to be advantageous in this application as well. Unfortunately, the full gain bandwidth available from a standard diode laser has not yet been fully utilized to achieve the shortest possible pulse width. However, provided appropriate conditions are met, asymmetric quantum wells can provide a substantial increase in the wavelength tunability of short optical pulses. Thus, asymmetric quantum well lasers may still provide an advantage with respect to ultrashort-pulse generation.

7.2 Short Pulse Generation Techniques

Three different techniques, as outlined below, can be employed to generate short optical laser pulses.

7.2.1 Q Switching

The first technique, which is referred to as Q switching, derives its name from modification of the quality, or Q, of the laser resonator [2]. The term Q switching refers to the process by which the cavity loss is abruptly switched from a low Q state to a high Q state. During the low Q state, lasing does not occur due to the high cavity loss. This condition allows the gain to become large, since it will not be saturated as it is under lasing conditions. However, when the loss is suddenly reduced (Q is increased) the gain is significantly higher than the threshold gain. As a result, the intensity in the cavity rapidly builds up to a large value (due to stimulated emission) in an attempt to reduce the gain to that of the threshold condition. This results in the formation of a short and intense optical pulse. Q switching is a common technique used to generate short optical pulses from gas and solid state lasers.

This technique can also be applied to diode lasers, either by the use of an external cavity or through integration of an absorbing region with the laser. If the diode laser is placed in an external cavity, then an external element may be used to modify the Q of the cavity, and as such, can be used to Q switch the laser. However, the most common implementation of Q switching for a diode laser utilizes an integrated absorber section. This absorber section can be created through ion or proton bombardment [88, 89] of a selected part of the laser, or through the use of a multi-electrode diode, in which one of the sections is biased below threshold. In the case of ion or proton bombardment, the Q switching is said to be passive, since the properties of the absorber cannot be directly controlled. In a multi-electrode configuration, both active [90] and passive [91] Q switching can be employed. Typical pulse widths from Q switched diode lasers lie in the few tens of picoseconds range (30-80 ps), however, with a specially designed three contact device [92, 93], 2 ps pulses have been demonstrated.

[2] A high Q cavity is one with low loss, whereas a low Q cavity is very lossy.

7.2.2 Gain Switching

The second and most common technique used to generate short optical pulses from diode lasers is known as gain switching. Gain switching may be considered a variant of Q switching; however, for the purpose of discussion in this thesis, gain switching will be treated separately.

Gain switching, as its name implies, refers to switching the gain from a low to a high and back to a low state, which results in the emission of a short optical pulse. In the context of a diode laser, this is most often achieved by the application of either a sinusoidal electrical input or a series of short electrical pulses. The resultant optical pulse can be significantly shorter than the applied electrical pulse, due to the internal dynamics of the diode laser. Pulses as short as a few picoseconds have been produced via gain switching [94], however, typical pulse widths are in the few tens of picoseconds [95, 96]. Highly chirped gain switched pulses emitted from a fast-tuned three section tunable distributed feedback (DFB) laser have been compressed down to approximately 600 fs [97]. These pulses were then amplified in an erbium-doped fibre amplifier and further compressed down to 230 fs [97].

7.2.3 Mode-locking

The third technique which can be used to generate short optical pulses is known as 'mode-locking'. The process of mode-locking is best explained through a re-analysis of the Fabry-Perot nature of the diode laser.

7.3 The Fabry-Perot Nature of a Laser Cavity

The cleaved facets of a diode laser act as a Fabry-Perot resonator which, in the frequency domain, produces evenly spaced cavity modes as illustrated in Fig. 6.1. These modes, which are known as longitudinal cavity modes satisfy the condition that the electric field

vanish at the boundaries of the cavity. This condition is met for wavelengths, λ, satisfying $m\lambda/2$=nL, where n is the index of refraction (group index) of the cavity medium, L is the cavity length, and m is an integer. The above relationship is more commonly expressed in frequency units, as the Fabry-Perot mode spacing, $\Delta\nu$, which is given by Eq. 7.1.

$$\Delta\nu = \frac{c}{2nL} \tag{7.1}$$

Under normal conditions, most lasers oscillate on many longitudinal modes, each with a random phase [3]. The result of this regime of operation is a continuous wave (CW) output. However, if a mechanism exists which can fix the phase of each of the modes, the resultant interference will produce a time varying optical output (i.e. a train of short optical pulses). The period, T, of these pulses is given by

$$T = \frac{2nL}{c} \tag{7.2}$$

which is simply the cavity round trip time. This phenomenon is illustrated in Fig. 7.2.

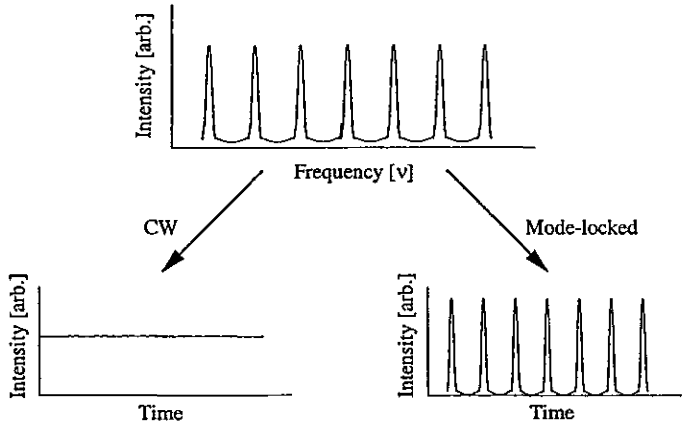

Figure 7.2: An illustration of mode-locking.

In the case of diode lasers, which are typically of the order of a few hundred microns in length, this mode spacing corresponds to a frequency in the hundreds of gigahertz. To reduce the mode spacing and hence reduce the pulse repetition rate, diode lasers can be

[3]On the following page, the mathematical formalism describing this phenomenon will be presented.

placed in an external cavity, whereby feedback from one of the laser's facets is eliminated by the application of an AR coating, and is replaced by an external optical element. Through Eq. 7.1, an increase in L directly results in a decrease in $\Delta\nu$.

7.3.1 Electric Field

Under steady state conditions, the electric field in the laser cavity can be described by

$$E(z,t) = \sum_m \varepsilon_m \sin(k_m z)\sin(\omega_m t + \phi_m) \tag{7.3}$$

where ε is the amplitude, ω_m is the frequency, and ϕ_m is the phase, all of which correspond to the m^{th} mode. k_m=mπ/L, where L is the length of the laser cavity. As discussed previously, under normal operating conditions, the phase of the individual modes is random, which results in a cw output. However, for the special case where ϕ_m=ϕ_{m+1}+2π, the absolute phase of each mode can be neglected and, after some mathematical manipulation Eq. 7.4 is obtained.

$$E(z^+,t) \propto \frac{\sin(N\pi[(z-ct)/2L])}{\sin(\pi[(z-ct)/2L])} \tag{7.4}$$

This equation describes a series of pulses spaced in z by 2L and in time by 2L/c, as a result of the interference of N modes. This is the basic description of mode-locking.

7.3.2 Time Bandwidth Product

The shortest pulse that can be produced from a mode-locked laser is determined by the gain bandwidth of the laser. This can be expressed as $\Delta\tau_p \propto 1/\Delta\nu_g$, where $\Delta\tau_p$ and $\Delta\nu_g$ are the pulse width and gain bandwidth, respectively. Obviously, lasers with large gain bandwidths are excellent candidates for the generation of short optical pulses via mode-locking. Diode lasers, whose gain bandwidths are typically on the order of 10 THz, should therefore be capable of generating pulses of 100 fs. Pulses of this duration have not yet been achieved directly from diode lasers.

7.4 Mode-locked Diode Lasers

A diode laser can be made to operate mode-locked by two very different techniques. The first technique, which relies on saturable absorption, is known as passive mode-locking. The saturable absorber can either be incorporated into the diode, or can be provided by a separate element located external to the diode. The second technique, in which some property of either the diode or an external element is varied at a frequency equal to that of the Fabry-Perot mode spacing, is known as active mode-locking. Active mode-locking can be achieved by the application of a time varying current/carrier injection to the laser, or by modulating the gain/loss of an external element. Hybrid mode-locking, which could be considered a third technique, is simply a combination of both passive and active.

7.4.1 Passive Mode-locking

A diode laser is passively mode-locked when the method which locks the modes in phase is provided by saturable absorption [4]. A saturable absorber can be integrated into a diode laser by the fabrication of a multi-electrode device (Chapter 5), or through the intentional introduction of damage to a specific section of the diode laser. Alternatively, for an external cavity passive mode-locked laser, an external element can be used to provide the saturable absorption.

Multi-electrode Saturable Absorption

In the multi-electrode configuration, a waveguide saturable absorber is achieved by controlling the bias to the absorber section such that threshold gain is not achieved. Under such conditions, light of the appropriate wavelength will be absorbed, resulting in the transition of an electron from an initial state in the valence band to a final state in the conduction band. This process will occur provided an electron exists in the lower energy state, E_1

[4] A detailed description of the theory of passive mode-locking can be found in [98, 99].

and an empty state at energy E_2 exists which satisfies $E_p = E_2 - E_1$. For a sufficiently high photon flux, a condition will be created whereby the upward transition is equally as probable as the downward transition. At this point, the absorption is said to be saturated and the semiconductor becomes transparent.

Multi-electrode devices have been passively mode-locked resulting in pulses as short as 1 ps [88]. However, the short pulses were followed by trailing pulses, which contained a significant amount of the total output power. The shortest 'single' pulses obtained are of the order of a few picoseconds [100].

Implantation Induced Saturable Absorption

Saturable absorption associated with intentional damage has been created by both ion and proton implantation. It is believed that the implantation process results in the formation of non-radiative recombination centers, which provide the necessary absorption. As in the case of the band gap transitions, a situation can be created such that the states responsible for absorption are filled, and as a result, the absorption is saturated. As a result of the intentional damage, decreased device lifetimes are often associated with such a device, making the multi-electrode device advantageous. Also, external control of the absorber is provided by the integrated waveguide absorber.

Pulses as short as 0.65 ps have been generated in a passively mode-locked external cavity laser, where the saturable absorption was created by proton bombardment [101].

External Element Saturable Absorption

In the external cavity configuration, multiple quantum well structures, with excitonic resonances at the laser's operating wavelength, are fabricated and placed in the external cavity to provide the necessary saturable absorption. These structures are usually proton or ion implanted after growth to introduce damage and hence reduce the absorption recovery times. Such structures are often mounted to one of the output couplers of the external

cavity, resulting in the generation of ultrashort optical pulses of duration of approximately 2 ps [88].

Saturable Absorption: Observable Phenomena

The presence of saturable absorption in a diode laser, be it monolithic or in an external cavity, can manifest itself in rather unique phenomena, one of which can be observed in the LI characteristics. L refers to the light (optical) output power, and I is the applied current. A laser with no or very little saturable absorption will have an LI curve as illustrated in Fig. 7.3a). A continuous yet significant change in the output intensity as a function of current is indicative of the onset of lasing.

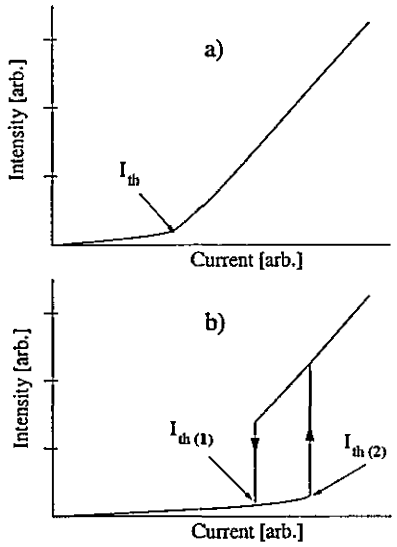

Figure 7.3: LI characteristics of a laser with a) no or very little saturable absorption and b) significant saturable absorption.

In the case of a laser that contains saturable absorption, the 'threshold' current may be exceeded, without the onset of lasing, as is indicated in Fig. 7.3b. However, at a higher current, an abrupt change in the output intensity may be observed, indicating the current at which the absorber saturates. As the current is further increased, the LI characteristic may be similar to that of the laser without saturable absorption. If the current is then

reduced, the transition from a high intensity output to a very low output state may not occur until a current below the turn-on current has been reached. This hysteresis in the LI curve is a signature of saturable absorption.

Another phenomenon that has been observed in multi-electrode lasers is that of self pulsations. As a result of this saturable absorption, and the interaction of the gain and loss dynamics in the two sections, the laser can operate in a regime where it emits a continuous train of optical pulses, the frequency of which is dependent on operating parameters as well as the physical structure of the laser. Self pulsations have been observed under a range of operating conditions with a number of different split contact devices used in this work. It was also found that a transition from mode-locking to self pulsations could occur when one of the operating parameters (such as gain current or absorber bias) was altered. The transition back to mode-locking could be induced by a slight re-adjustment of operating parameters, or sometimes, more simply by interruption of feedback from the external cavity. This type of behavior is common in other types of mode-locked lasers.

7.4.2 Active Mode-locking

Active mode-locking can be achieved in a diode laser by the application of an appropriate time varying (radio frequency or microwave) current to the diode, or by the modulation of the loss of an element in the external cavity. Due to the ease with which the diode laser gain/loss can be modulated, particularly at lower frequencies, active mode-locking can be achieved through direct diode modulation. The applied rf current provides a modulation of the gain/loss of the laser which can result in the modes of the laser being locked in phase, provided the excitation frequency corresponds to that of the Fabry-Perot mode spacing. As mentioned above, a monolithic diode laser has a typical length of 500 μm. This results in a mode spacing on the order of 100 GHz. Efficient coupling of such a high frequency signal into a diode laser is a difficult task, and is limited by parasitics as well as fundamental diode

limitations.

Extended cavity diode lasers[5] have been fabricated in order to reduce the Fabry-Perot mode spacing, resulting in pulses as short as 1.4 ps at a frequency of 15 GHz [102]. Colliding pulse mode-locking, which occurs when the absorber section is located in the middle of the cavity such that counter-propagating pulses interact with each other in the absorber, has also been demonstrated in a long three section monolithic device, which produced pulses as short as 0.64 ps [103]. research, both from a the fabrication of quantum well laser

As a result of the disadvantages associated with active mode-locking of monolithic devices, external cavity mode-locking was determined to be the better technique in our case, particularly when considering the goals of the project and our intended applications of the short pulses. Although modulation at the lower frequencies associated with an external cavity is simplified, the requirement of an external cavity places a significant increase on the demands for the design and realization of such a system. However, along with the reduced complexity in the rf driving network, one gains added flexibility on selection (and reduction) of the pulse repetition rate. Active mode-locking of diode lasers has been achieved over a wide range of frequencies, from the low MHz to greater than one GHz, with typical pulse durations in the range of a few picoseconds to tens of picoseconds [104, 105].

7.4.3 External Cavity Mode-Locking

The modulation frequency required to achieve active mode-locking in a diode laser can be modified by placement of the diode in an external cavity. In this configuration, feedback from one of the laser facets is reduced (ideally eliminated) by the application of an antireflection facet coating. The required feedback is then provided by an external optical element,

[5]An extended cavity diode laser is one which contains an added section which provides neither gain nor absorption. Typically, the active region of the extended cavity has been altered such that it is transparent to the lasers operating wavelength.

such as a diffraction grating or mirror. The length of the cavity, and hence the Fabry-Perot mode spacing, can then be tailored, providing another degree of freedom in the system design. It has also been shown that, within limits, a higher excitation frequency produces shorter optical pulses [100], as a result of the enhanced pulse shaping induced by the time varying gain. This tradeoff raises an interesting question with respect to optimization of the cavity length and hence repetition rate for the intended application of the mode-locked diode laser system.

7.4.4 Pulse Width Limiting Phenomena

As discussed briefly in a previous section, pulses equivalent to the theoretical limit imposed by the gain bandwidth of the diode laser have not yet been achieved. The time-bandwidth product of a Gaussian pulse is given by;

$$(\Delta\nu)(\Delta t) \leq 0.4413 \tag{7.5}$$

Therefore, for a 15 nm bandwidth 980 nm laser ($\Delta\nu$=4.7 THz), the theoretical pulse width is 95 fs. A number of different phenomena have been used to explain the pulse width limitations that have been observed experimentally. Research in this area is ongoing.

7.5 Ultrafast Pulse Diagnostic Techniques

Currently, the fastest commercially available detectors operating in the 1 micron wavelength range have a FWHM response time of approximately 15 ps.[6] As a result, the accurate determination of pulse widths in the low picosecond regime requires an indirect method. In the following section, the standard autocorrelation technique will be described, along with details of the system used in this work. The interested reader is referred to references [106-109] for a more complete description of short pulse correlation techniques.

[6]New Focus high speed photodiode, model 1554.

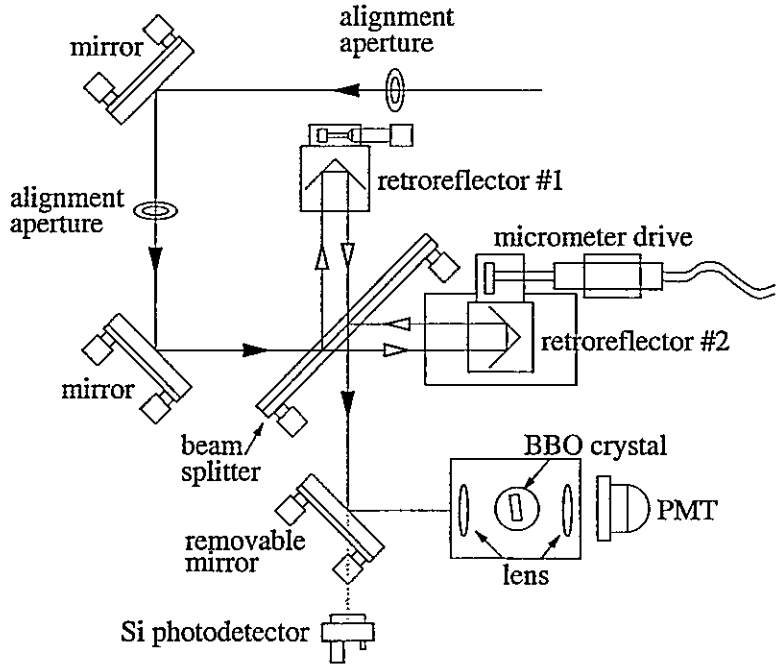

Figure 7.4: Schematic of the autocorrelator used in this work.

In a standard autocorrelator, an input pulse of fixed duration is separated into two identical pulses by a broadband beam splitter. Each of these pulses is allowed to propagate in free space along different paths, after which they are recombined. By varying the length of one of the paths with respect to the other, one of the pulses can be swept through the other, providing a mechanism to determine the pulse width.

A schematic of the autocorrelator that was designed and built for use in our laboratory is illustrated in Fig. 7.4. This autocorrelator was designed to provide the flexibility to measure both the first and second order interferometric (collinear) autocorrelations, as well as background-free (second order, non-collinear) autocorrelations.

For implementation of the first order correlation, the output of the autocorrelator is focussed onto a slow detector (silicon photodiode) whose signal is monitored by a computer data acquisition system. Retroreflector #1 of the autocorrelator is translated by an Oriel Instruments encoder 'mic' with 2.5 cm of travel. This manipulator is capable of slow scans

required for the interferometric measurements. The resultant intensity at the detector is a function of the position of the second arm relative to the first. This difference is called the delay and is given by $\tau=\Delta d/c$. The detected intensity is thus a function of τ, as a result of two different 'pulse' properties: pulse length and coherence length. If the coherence length of the pulse is less than the pulse duration, the measured pulse length will be underestimated. For this reason, a first order autocorrelation does not provide an unequivocal measurement of the pulse duration.

The second order interferometric autocorrelation is obtained by measuring the second harmonic of input pulse, which is generated by the interaction of the pulse with nonlinear material. In our autocorrelator, this measurement is obtained by focusing the output of the autocorrelator onto a 2 mm thick BBO (Beta Barium Borate) crystal. An identical lens is used to collect both the second harmonic (at 2ω) and the signal (ω), and focus them onto a photomultiplier tube (PMT). A glass filter is used to absorb the longer wavelength signal, such that only the second harmonic is detected.

As in the case of the first order autocorrelation, the output of the PMT is a function of τ, as a result of the pulse width and the pulse phase. However, due to the second order nature of this interaction, the coherence and duration of the pulse can be determined separately, thus making an accurate assessment of the pulse duration independent of its coherence.

As a result of the low output intensities of mode-locked diode lasers, the generated second harmonic intensity is weak. To improve the signal to noise ratio, the input intensity is modulated at a low frequency by an optical chopper. This allows the PMT signal to be monitored using a lock in amplifier (Stanford SR510), greatly improving the signal to noise ratio. In our measurements, the integration times were such that only the slowly varying envelope component of the correlation function was measured, the higher frequency compo-

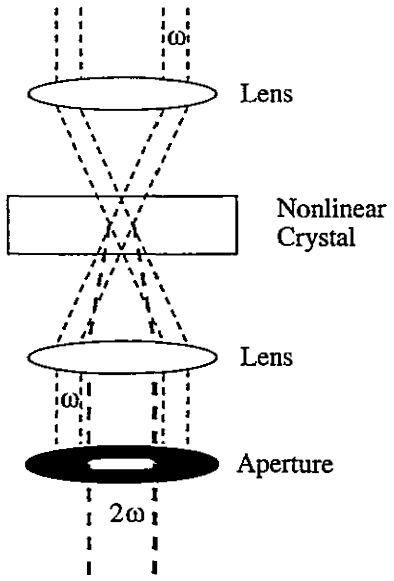

Figure 7.5: Experimental arrangement used to obtain background free intensity autocorrelation.

nents (corresponding to constructive/destructive interference of the field) being effectively filtered. This produces the well known collinear intensity autocorrelation with background, which provides an accurate assessment of the pulse duration.

Another type of second order autocorrelation, known as the background free autocorrelation, can be obtained with the above autocorrelator. By translating retroreflector 1, the output from the two arms of the interferometer can be separated into two parallel traveling beams. As such, they can be focussed in a nonlinear crystal as illustrated in Fig. 7.5. As a result of the phase matching conditions within the crystal, the second harmonic will only be generated when the pulses from the two different arms overlap within the crystal, both spatially and temporally. As such, when the delay (τ) is larger than the pulse duration, zero signal will be measured, making this technique 'background free.'

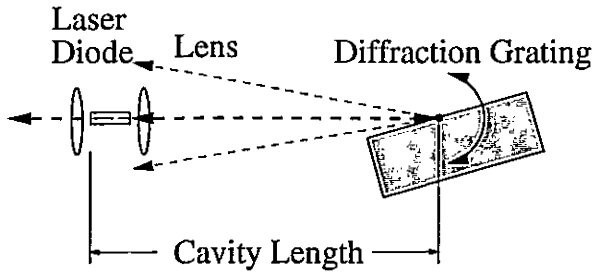

Figure 7.6: External cavity configuration used for mode-locking.

7.6 Experimental Results: Mode-locking

In the following sections, the experimental results obtained from the short-pulse external-cavity diode laser system will be presented.

7.6.1 External Cavity Configuration

The external cavity configuration used in all of the work described in this thesis is illustrated in Fig. 7.6. The smaller contact section of the split contact laser, which was used as the saturable absorber, was placed at the end of the diode from which the pulse output was taken. The other section, which is referred to as the gain section, was placed with the AR coating facing the external cavity. The distance between the coated diode facet and the grating was fully adjustable through the use of a translation stage. A picture of the diode laser external cavity configuration is provided in Fig. 7.7.

For flexibility, all of the diode lasers were tested in the external cavity in bar format. This allowed numerous devices to be tested with ease, without the need for lengthy pre-test preparations. However, it should be noted that mounting the laser chip on the appropriate carrier will provide substantially better temperature control and stability, as well as mechanical stability. Proper mounting of the laser will also improve coupling of the high frequency signal to the diode. This should improve all aspects of device performance. The added requirement of free access to both facets, however, places a substantial demand on the carrier design, rendering most commercially available carriers useless.

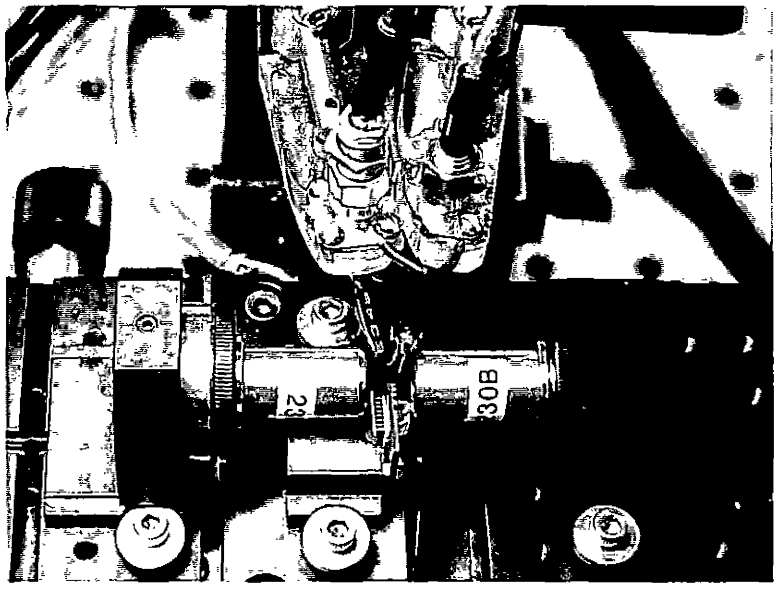

Figure 7.7: External-cavity laser mounting configuration.

In Fig. 7.7, a laser bar can be seen mounted on the copper block. This bar contains split contact devices, therefore requiring two probes, as illustrated. Two identical lenses are used to collect the output from the two laser facets. The copper block is mounted on an aluminum holder using teflon screws. Between the copper and aluminum blocks is a thermoelectric cooler, which provides temperature control of the operating laser. The temperature is monitored by a thermistor, which is used by the ILX LDC 3724 laser driver to control the current to the cooler, and hence the laser temperature. All experiments described here were performed at 20 °C.

A schematic of the mode-locked split contact diode laser bias control is illustrated in Fig. 7.8, and a schematic of the optical diagnostics system is provided in Fig. 7.9.

To achieve hybrid mode-locking, both an RF and a dc current are applied to the gain section of the device. The dc bias is provided by a laser driver (ILX LDC 3724) and the rf is provided by an HP 83732B synthesized signal generator, capable of providing up to 18 dBm of power. The absorber section's voltage was controlled by a Keithly 238

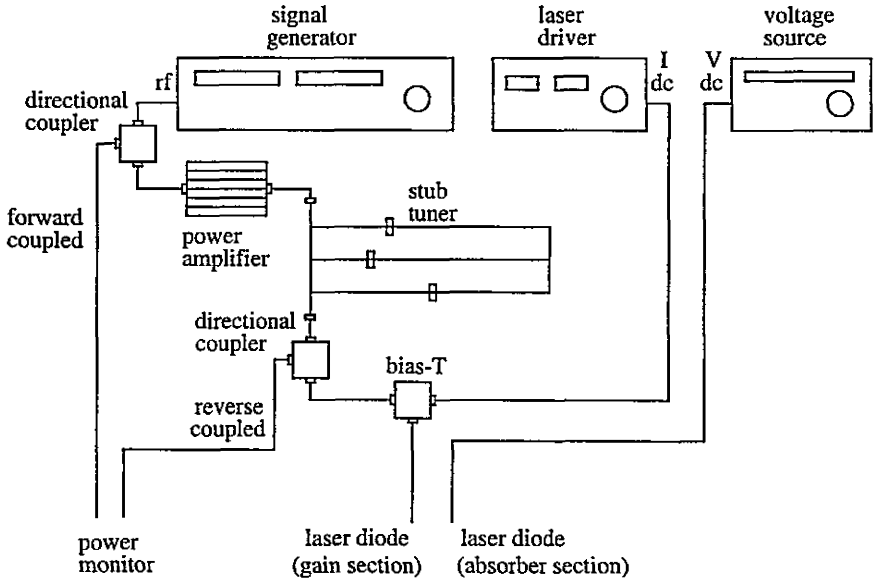

Figure 7.8: Schematic of the electronics used in the mode-locking of a split contact diode laser.

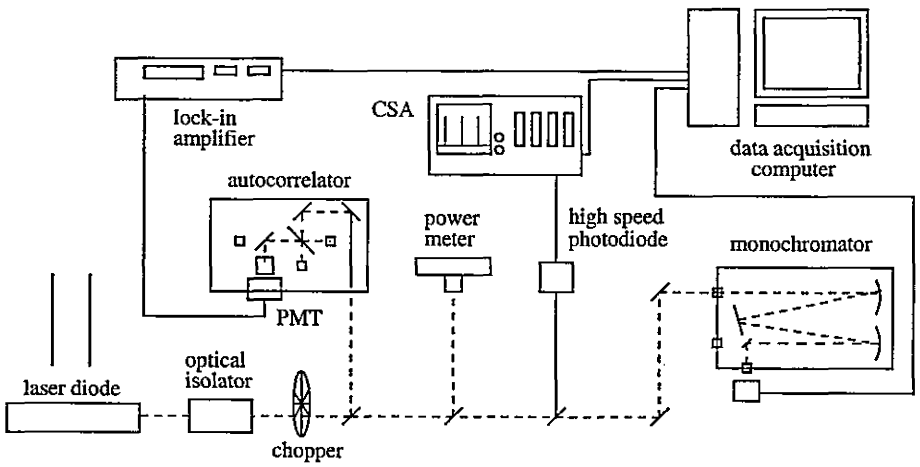

Figure 7.9: Detailed schematic of the optical diagnostics used in the evaluation of the short pulses diode lasers.

Source Measurement Unit (SMU) which fixed the absorber bias and measured the resultant absorber current. For purely passive mode-locking, only dc biasing was applied.

The output of the HP synthesizer is coupled to a directional coupler, which transmits 90% of the input power to the power amplifier (Minicircuits ZHL-2), which provides a maximum output power of 1 Watt. The remaining input power is extracted from the third port of the directional coupler and is used to monitor the power delivered to the amplifier. The amplifier output power is directed through another directional coupler to a three stub tuner (Microlab/FXR S3-02N) which provides impedance matching to the diode laser. Reflected power (from the diode) is coupled to the remaining port of the directional coupler. This allows the stub tuner to be optimized to deliver the maximum power to the diode. The output of the tuner is combined with the dc output from the laser driver using a bias-T. The combined rf-dc signal was then sent directly to the diode laser as illustrated in Fig. 7.7.

Coupling of the laser diode output to the external cavity is controlled by a three axis flexture stage with piezoelectric actuators, capable of a position resolution and stability better than 0.05 μm. It was found that alignment of the laser in the external cavity was extremely critical, both with respect to tunability and stability, as well as mode-locking and pulse duration. The output coupling is provided by an identical flexture stage without piezoelectric actuators. Aspheric lenses with a numerical aperture of 0.55 are used to collect the emission from both facets.

7.6.2 Ultrashort Pulses

Ultrashort optical pulses, in the range of 2 to 15 ps were obtained from the InGaAs quantum well laser described in Chapter 5. This represents, to the best of the author's knowledge, the first report of mode-locking with an 'aluminum free', InGaAsP/GaAs laser. All three variations of mode-locking (passive, active and hybrid) were achieved, at frequencies from

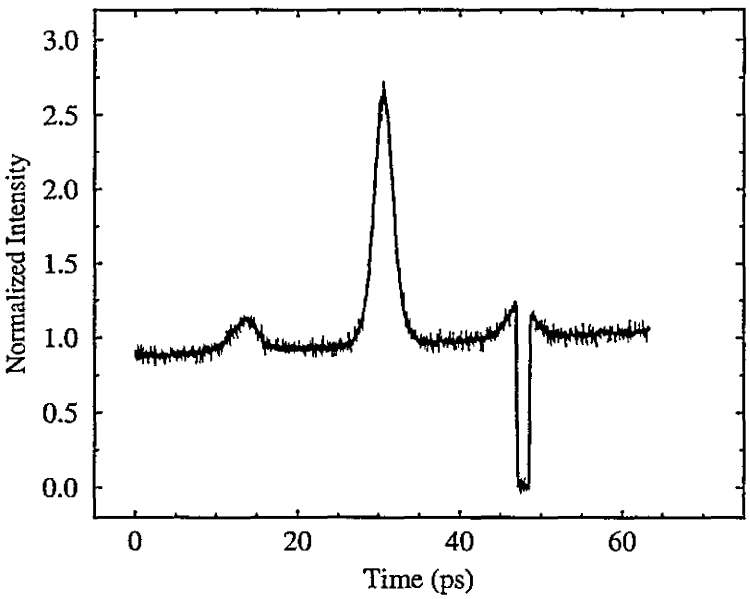

Figure 7.10: Second order collinear intensity autocorrelation trace of a 2.7 ps pulse.

about 300 MHz to 800 MHz. To date, the shortest pulses were obtained from hybrid mode-locking with feedback from a 1200 line/mm diffraction grating, at a repetition rate of approximately 700 MHz. These pulses had a 2^{nd} order autocorrelation FWHM of 2.7 ps, which, for a hyperbolic secant pulse, corresponds to a pulse duration of 1.9 ps. The average output power was 1 mW. The 2^{nd} autocorrelation trace of this pulse is provided in Fig. 7.10. The low intensity 'dip' at approximately 50 ps is a result of intentional blocking of the input beam, to allow normalization of the autocorrelation intensity. The gentle slope of the background is a result of imperfect optical alignment of the autocorrelator.

As can be seen in the above figure, the autocorrelation trace does not correspond to that of a single pulse, but rather multiple pulses. A second pulse is observed on each side of the main pulse, located approximately 17 ps away. This time corresponds to the round trip time in the diode laser chip, which indicates that the pulses are a result of residual reflection from the AR coated facet. The requirement on the AR coating to eliminate the

secondary pulses has been studied theoretically, indicating that a reflectivity as low as 10^{-4} is insufficient [104, 100] to entirely eliminate such trailing pulses, as is consistent with our experimental observations.

Both the intensity and the total number of trailing pulses are strongly dependent on the time rate of change of the gain and loss within the cavity. Obviously, if the net gain has been reduced significantly in one round trip time of the pulse in the diode, the secondary pulse intensity will be significantly reduced. As such, higher frequency mode-locking, for a given facet reflectivity, normally results in a reduction of the trailing pulses. Also, in the case of a split contact device with one of the sections being operated in a saturable absorption regime, trailing pulse reduction can be significantly improved, particularly for a saturable absorber whose recovery time is shorter than that of the round trip time in the internal cavity. In the same context, increasing the diode length can also reduce the trailing pulses, since the extra delay associated with a longer cavity provides more time for the absorber to recover, or the gain to be reduced. Such device parameters can be optimized to realize the shortest optical pulses.

The peak to background ratio (3:1) of the autocorrelator signal corresponds to that generated by a short coherent optical pulse [110, 111]. The spectrum of such a pulse, acquired by a slow scan of the grating of a 3/4 meter monochromator, is provided in Fig. 7.11. The best fit to the second order intensity autocorrelation corresponds to that of a hyperbolic secant pulse duration, although the fit is by no means unambiguous. This fitting function implies a pulse duration of 1.9 ps. The minimum bandwidth required to obtain such a pulse is 0.6 nm. From Fig. 7.11 a bandwidth of approximately 0.6 nm was determined, implying that these pulses are approximately transform limited.

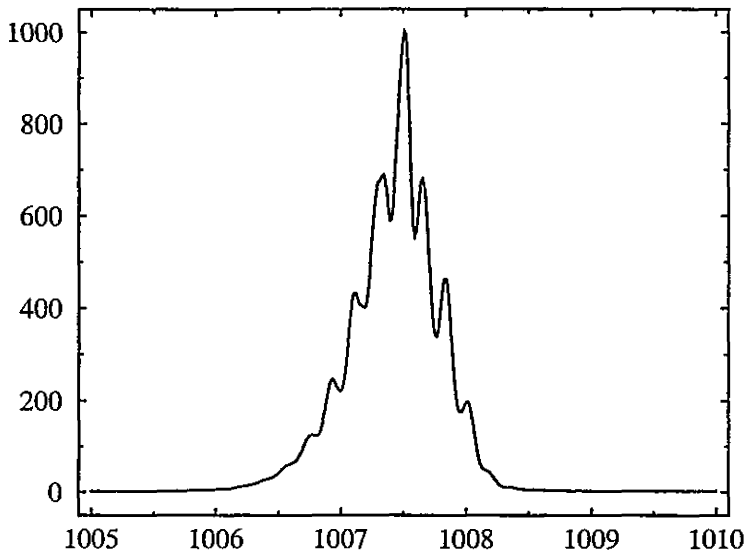

Figure 7.11: Optical spectrum of the 2.7 ps pulse illustrated above.

Grating Feedback vs Mirror Feedback

The use of a 1200 line/mm grating, as above, significantly reduces the optical bandwidth that is fed back into the diode laser. As in the case of CW operation, the peak wavelength of the pulses can also be tuned. From the perspective of two-photon fluorescence microscopy, tunable short pulses are advantageous. The hybrid mode-locked diode lasers described above could be mode-locked over a range of about 17 nm, provided appropriate adjustment of operating parameters such as bias current, rf frequency and absorber voltage, was performed. As will be discussed in Chapter 8, extension of this tuning range is possible, and will be studied in great detail in the future.

By replacing the diffraction grating with a planar dielectric mirror, both the operating wavelength selectivity and the bandwidth limitation of the external cavity are removed. As a result, the spectra of the pulses are significantly broadened, with a FWHM significantly greater than 1 nm. Passively mode-locked pulses using mirror feedback have been

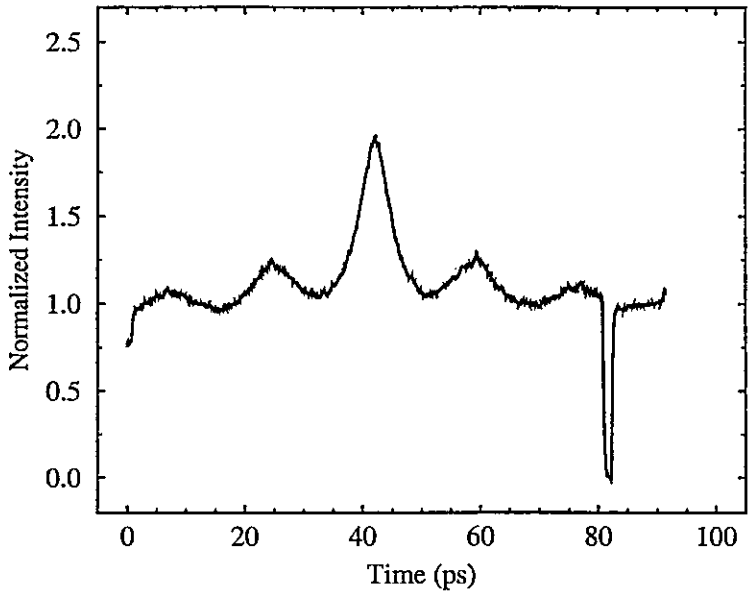

Figure 7.12: Measured autocorrelation trace for an excitation frequency of 699.5 MHz.

produced with this laser, having bandwidths in excess of 2 nm. From the perspective of post amplification and compression, this enhanced bandwidth could be utilized to generate even shorter pulses.

7.6.3 Impact of Operating Conditions

Under mode-locked operation, the effect of the driving frequency on the pulse width was measured to determine the optimal operating conditions of the laser for a given cavity length and operating wavelength. This analysis was performed on a hybrid mode-locked diode laser with grating feedback, operating at a wavelength of approximately 1 μm. Figures 7.12 and 7.13 illustrate the second order autocorrelation traces for drive frequencies of 699.5 and 698.9 MHz, respectively. The optimal frequency was determined to be 699.3 MHz, with the corresponding autocorrelation in Fig. 7.14.

As can be seen by comparison of the three figures referenced above, the output pulses are very sensitive to the driving frequency. For the detuned pulses, the ratio of the

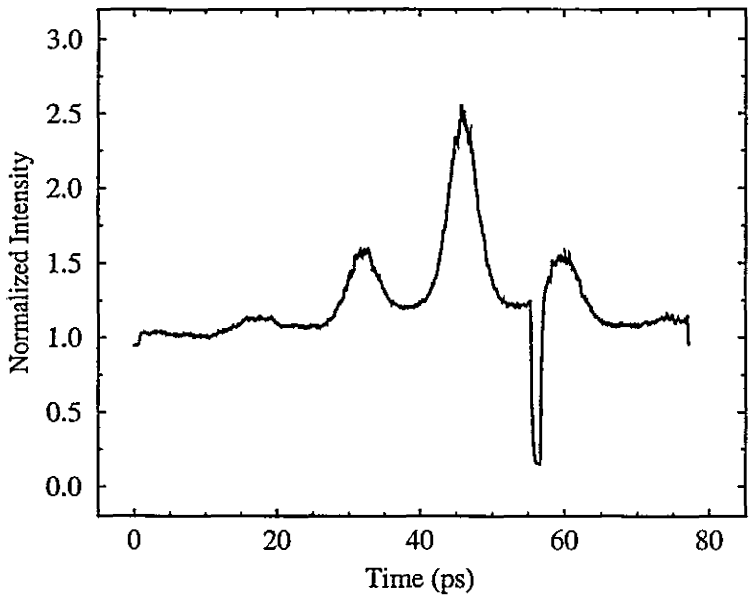

Figure 7.13: Measured autocorrelation trace for an excitation frequency of 698.9 MHz.

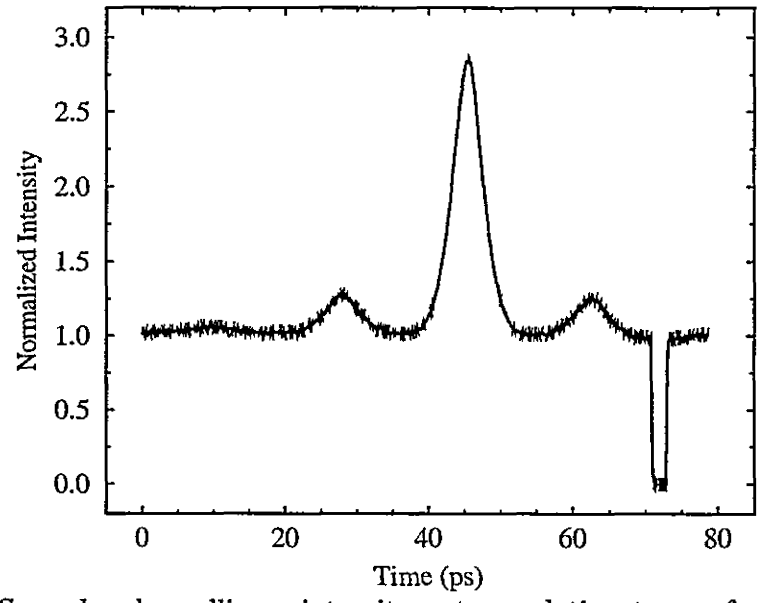

Figure 7.14: Second order collinear intensity autocorrelation trace of a sub 5 ps pulse, operated at the optimal drive frequency.

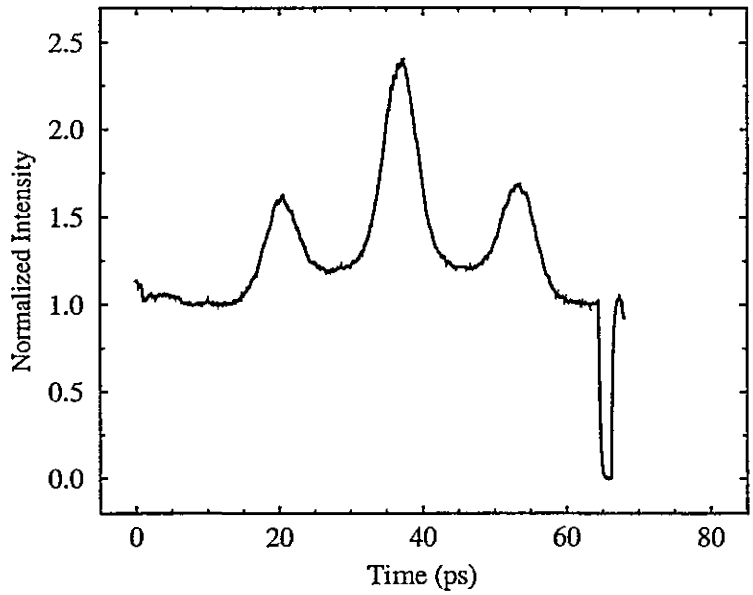

Figure 7.15: Measured autocorrelation trace for an excitation frequency of 698 MHz.

peak to background is reduced, which is an indication of a poorer quality pulse. Also, the main and the trailing pulses are seen to ride on a much wider pulse envelope, which is indicative of incomplete mode-locking. Further detuning of the frequency results in a much poorer output pulse, as illustrated in Fig. 7.15, which corresponds to a driving frequency of 698 MHz. This pulse has significantly larger trailing pulses, as well as a much more severely modulated background.

From the observations above, it is clear that a stable rf source with a well defined frequency is required to achieve active mode-locking. Experiments in our lab utilizing a voltage controlled oscillator without a phase-locked loop were unsuccessful, in that mode-locked operation could not be achieved. This was due to the spectral width of the rf source and its frequency instability.

A study similar to that carried out on the drive frequency was performed to determine the sensitivity of the mode-locked diode laser to the applied bias voltage. Figure 7.16

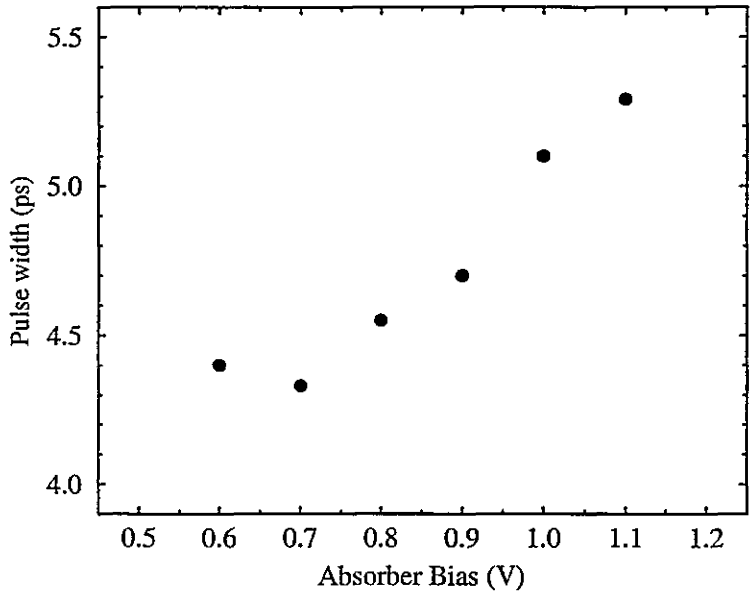

Figure 7.16: Effect of absorber bias on pulse width.

illustrates the pulse width as a function of absorber section bias. Absorber biases outside of the data range provided resulted in significantly larger pulses.

Similar to the phenomena observed above, good quality pulses could be obtained over a moderate range of applied rf power, with a reduction in rf power being associated with a reduction in total pulse energy (power). Figure 7.17 illustrates the measured pulse width as a function of applied rf power. Powers in the range of 25-30 dBm (Power[dBm]=10log(Power[mW])) resulted in pulses of similar quality, without a noticeable reduction in pulse shape quality being observed until approximately 22 dBm, at which point a large percentage of the total energy began to appear in the trailing pulse, as well as in the underlying background.

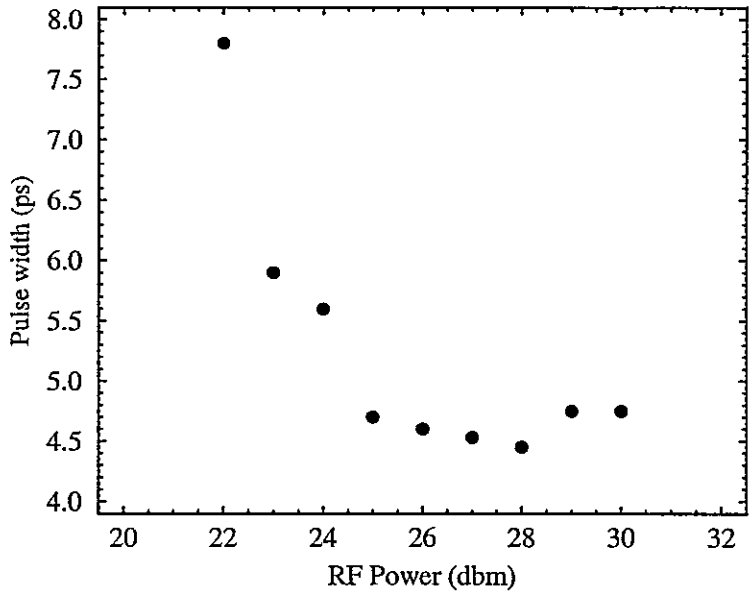

Figure 7.17: Impact of applied rf power.

7.7 Two-photon Fluorescence Microscopy

As was described in the Introduction, one of the potential applications for the ultrashort-pulse laser system, is that of two-photon fluorescence (TPF) microscopy. In the following section, a preliminary evaluation of this potential application is described.

The technique of TPF microscopy has a number of advantages over conventional fluorescence microscopy, some of which will be briefly discussed after a short description of the technique has been provided.

The use of fluorescent dyes as biological markers allows a rapid and detailed study of the structure and organization of a particular biological specimen to be performed. Standard fluorescence techniques, as well as the application of confocal microscopy [112] have become well established in recent years. As a result of a number of disadvantages associated with standard fluorescence techniques, two-photon induced fluorescent techniques are being investigated [113] and applied to the analysis of biological samples [114, 115]. Most of

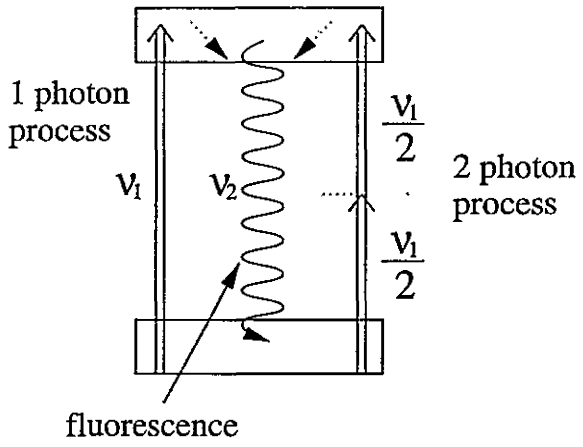

Figure 7.18: Principle of single and two-photon fluorescence.

the two-photon fluorescent investigations have used large, expensive and relatively complex Titanium:sapphire lasers. As a result of the complexity, cost, and large 'footprint' of such laser systems, alternative sources of short optical pulses in the near IR wavelength range would be extremely beneficial.

7.7.1 TPF: The Technique

In TPF microscopy, the emitted fluorescence is generated by the simultaneous absorption of two photons, whose combined energy is approximately equal to the typically utilized single photon energy. As a result of this absorption, the excited dye undergoes a relaxation process, which results in the emission of a photon of energy slightly less than that of the excited transition. The basic process of both single and two-photon fluorescence is illustrated in Fig. 7.18. The yield of single photon fluorescence is proportional to the intensity of the excitation source. The two-photon fluorescence yield, as a result of its second order nature, is proportional to the square of the excitation intensity.

A typical TPF system would contain elements similar to those illustrated in Fig. 7.19. As a result of the difference in the wavelengths of the fluorescence ouput and the 'pump' input, a number of advantages of two-photon fluorescence are revealed. First, due

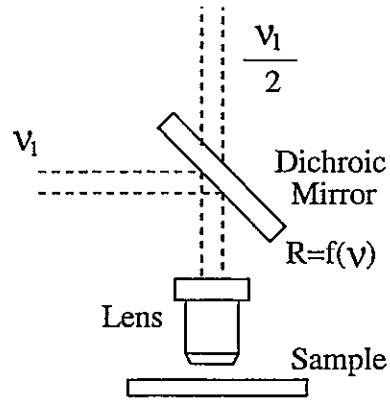

Figure 7.19: Simplified two-photon microscopy system.

to the presence of the dichroic beam splitter, TPF has an obvious advantage: it is much easier to separate two photons of wavelength 1 μm and 500 nm, than it is to separate two photons of 500 and 520 nm. Additionally, standard photomultiplier tubes have a very high sensitivity to visible photons, and a much reduced (essentially negligible) sensitivity to near IR wavelengths.

The second main advantage of TPF microscopy is related to the second order dependence of the TPF process. Because of the I^2 dependence of the fluorescence yield, the vast majority of the fluorescence will be generated from the focal point. This results in an improved resolution for the TPF system.

From the perspective of applications to biological imaging, TPF also presents an advantage as a result of the excitation wavelength. The longer wavelengths tend to produce less damage in the samples. This allows samples to be analyzed over a much longer period of time, as well as allowing a wider range of samples to be studied.

The ability of a mode-locked diode laser to be used for TPF microscopy has been investigated by the study of TPF from a mixture of a molecular dye (Rhodamine 590) with ethanol. The experimental setup used in this investigation is illustrated in Fig. 7.20. A confocal lens arrangement, which allowed for easy optical alignment, was employed to excite the dye and collect the resultant fluorescence. The collected fluorescence was measured by

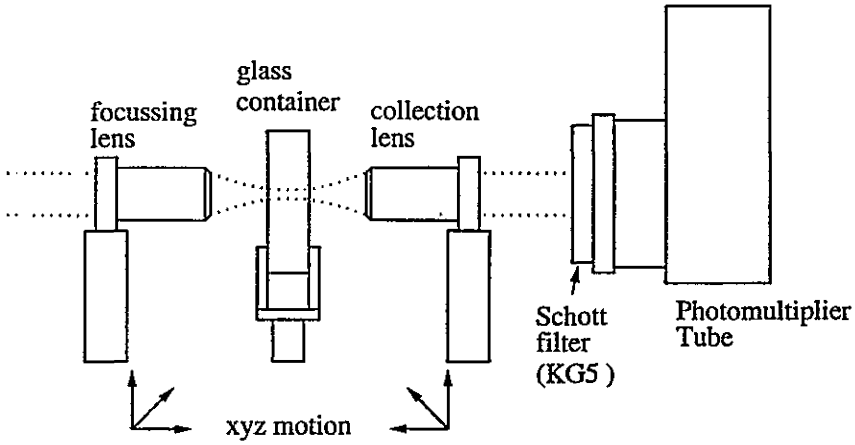

Figure 7.20: Experimental configuration used to observe TPF in a dilute molecular dye.

a photomultiplier tube, whose sensitivity to long wavelengths (> 900 nm) is negligible. A filter, which transmitted visible wavelengths and was strongly absorbing of the excitation source (T$\simeq 10^{-5}$) was also placed in front of the PMT input to eliminate essentially all of the longer wavelength light. A series of neutral density filters were then used to reduce the input pulse intensity, and observe the associated decrease in the fluorescence yield. This data is illustrated in Fig. 7.21. Plotted in this graph is the experimental fluorescence yield as a function of normalized excitation intensity. Also plotted are the theoretical fluorescence yields for both a two-photon and a single photon process, (calculated from the normalized pump intensity of 1). In the limited intensity range studied here, the experimental data closely follows that of the two-photon process, demonstrating two-photon fluorescence.

7.8 Wavelength Tunable Mode-locked Operation

As was discussed in the beginning of this chapter, diode lasers operated in an external cavity can be tuned using a simple diffraction grating. As was also illustrated in a previous section, the peak emission wavelength of short optical pulses can also be tuned, in the same manner as described above. However, the tuning range over which mode-locking can still be achieved is very likely limited by the bandwidth of the antireflection coating, as opposed to

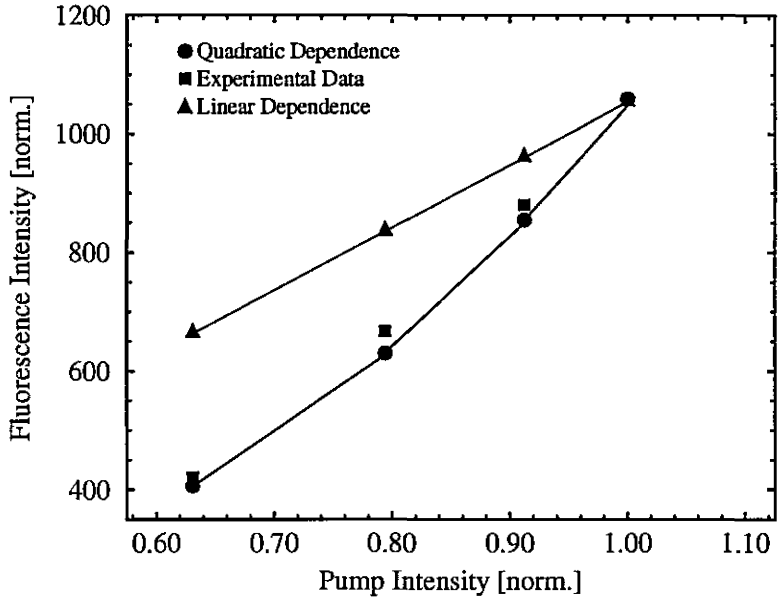

Figure 7.21: Two-photon fluorescence.

the bandwidth of the gain peak. A number of different approaches can be taken to further increase this short-pulse tuning range.

7.8.1 Multilayer Antireflection Coatings

Although single layer antireflection coatings are the easiest to fabricate, for many applications the bandwidth over which a very low reflectivity is achieved is insufficient. As such, multiple layers can be used to increase the low reflectivity bandwidth. A comparison of the performance of a single layer and a double layer AR coating is provided in Fig. 7.22. As is clearly illustrated in Fig. 7.22, a significant increase in the low reflectivity bandwidth can be achieved in a two layer coating. The single layer AR coating has an index and thickness of 1.8 and 1389 Å respectively. The two layer coating properties, starting from the layer adjacent to the substrate are 2.628 and 1.46 for the index, and 951 Å and 1712 Å for the thickness.

From the practical perspective, however, the two layer AR coating is difficult to fab-

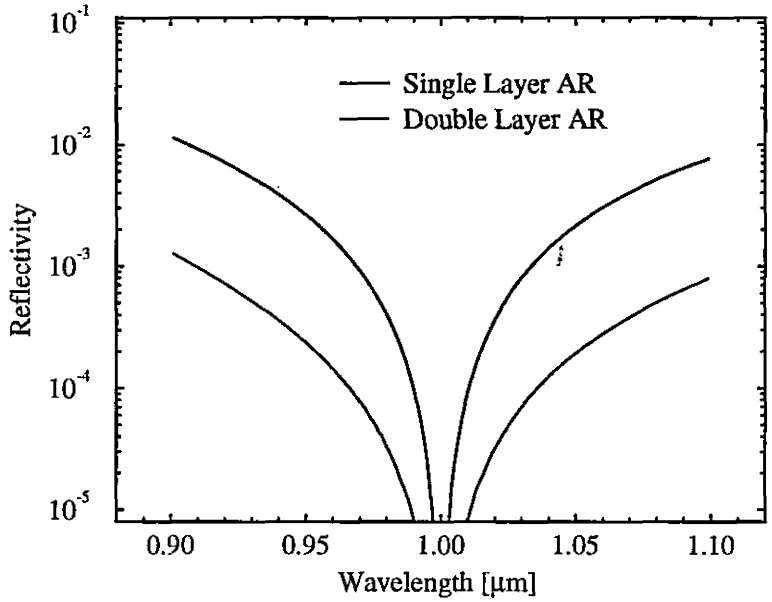

Figure 7.22: Comparison of the reflectivity profile of a single and a double layer antireflection coating.

ricate with both layers satisfying the tolerances described in Chapter 6. As such, although two layer AR coatings with significantly increased bandwidths have been deposited [21], it is at the expense of the absolute minimum in reflectivity. This tradeoff can be understood as follows: To a first approximation, for a single layer AR coating, the index of refraction of the film determines the absolute minimum in the reflectivity profile. The thickness of the coating determines the wavelength at which this minimum occurs. This implies that the index of refraction must be controlled to obtain a very low reflectivity, and the thickness must be controlled to have the minimum in the reflectivity occur at the desired wavelength.

The situation is more complicated for the two layer coating. As in the case of the single layer coating, the index of the layers will influence the minimum reflectivity. However, the thicknesses of the two layers will not only determine the wavelength at which the minimum in the reflectivity profile occurs, but they will also significantly influence the absolute value of this reflectivity minimum. From the perspective of a quarter wave

analysis, a higher reflectivity minimum will occur when the quarter-wave wavelengths of the two layers are different. As a result of the requirements imposed on the two layer AR coating, use of multilayer AR facet coatings may not be ideal, particularly when the coating is the only reflectivity reducing element.

7.8.2 Angled Facet Lasers

The wavelength range over which a diode laser can be forced to operate, as well as the ultrashort pulse duration, can be limited by both the laser gain bandwidth and the wavelength dependence of the facet reflectivity. The gain bandwidth and hence the tuning range, as described above, have been increased by the use of asymmetric quantum wells. The low reflectivity bandwidth limitations imposed by antireflection facet coatings, however, must be addressed to take full advantage of the added gain bandwidth.

The second technique which has been studied to reduce the facet reflectivity involves an entirely different device structure, known as an angled facet laser. In an angled facet laser, the cleaved facet is not perpendicular to the ridge, as it is for a standard diode lasers, but rather is oriented at an angle to reduce the amount of reflected light coupled into the waveguide. Angled facet devices can be easily fabricated with existing processing tools by simply misorienting the ridge waveguide with respect to the appropriate wafer crystal direction. This approach results in both facets being angled.

One facet of an angled ridge waveguide structure is illustrated in Fig. 7.23. With the aid of this figure, the impact of the angle on the modal reflectivity becomes very clear.

The propagation direction of the guided mode and the reflected mode, as well as the laser output, are illustrated. As is clear, the amount of light that can be captured by the waveguide from the reflected mode is greatly reduced for such a structure. As a result, and as has been demonstrated in our laboratory, as well as elsewhere [116, 117], such structures have greatly reduced modal reflectivities. Modal reflectivities in the 10^{-4} range [116, 117]

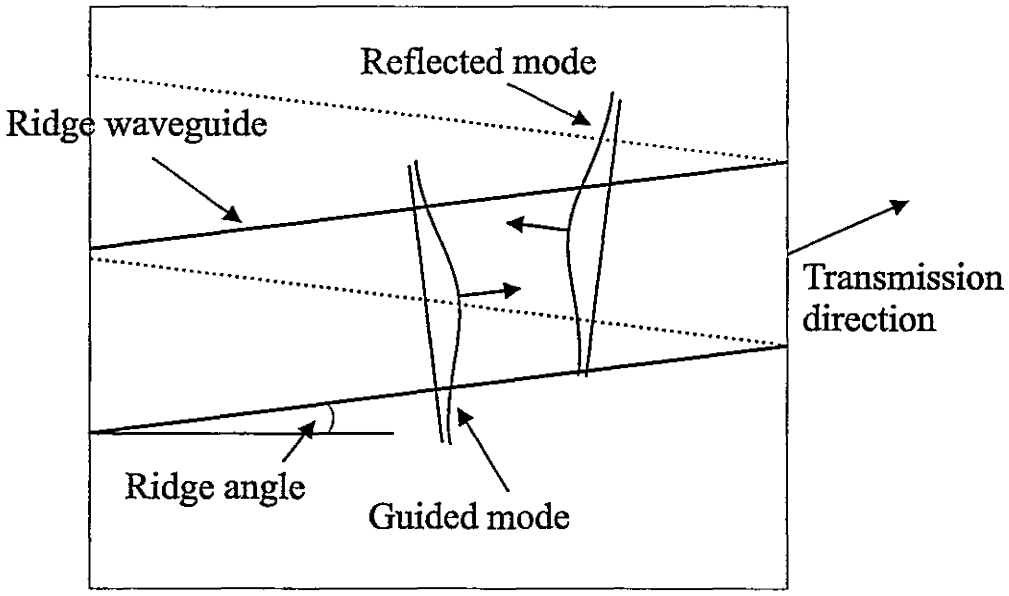

Figure 7.23: Illustration of a simple angled facet ridge waveguide.

have been achieved for angled facet devices with angles in the range of 5° to 10°.

Perhaps the most attractive aspect of angled facet devices is not the low reflectivity that they provide, but the insensitivity of the reflectivity to wavelength. Further reduction of the modal reflectivity can then be provided by a multiple layer AR coating, where the absolute minimum achievable reflectivity is not as critical as in the non-angled facet laser.

Laser devices utilizing angled facets, with an angle of approximately 5°, are currently being explored in our laboratory, to improve both the pulse properties from a mode-locked diode laser, as well as, more importantly, the tunability of the short pulses. The asymmetric quantum well structure described previously [84] may then be utilized to its full extent, as a result of the reduced feedback from the facets in the angled facet configuration. A similar device was very recently reported [118], for which mode-locked pulses were generated over a wavelength range of 60 nm, centered at about 820 nm.

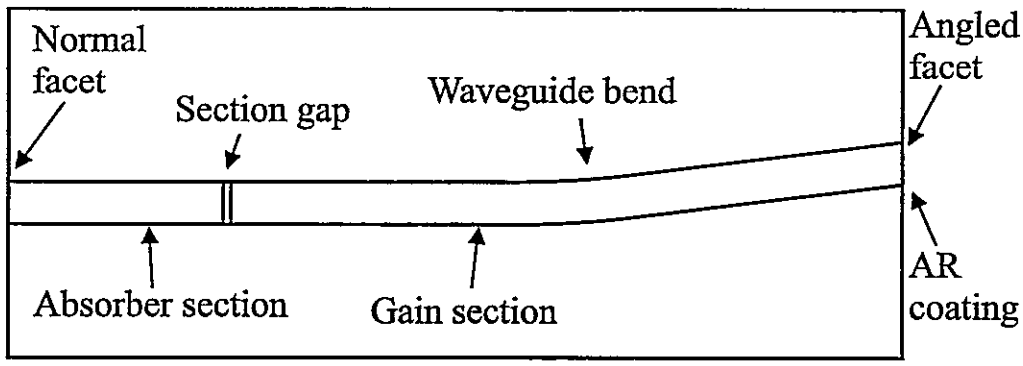

Figure 7.24: Illustration of an improved angled facet device for the generation of ultra-short pulses.

7.8.3 An Improved Angled Facet Design

One of the main drawbacks of simple angled-facet devices such as that illustrated in Figure 7.23, for the application of short-pulse generation, is the need for two external feedback elements. In order to obtain efficient laser operation, feedback must be provided at both ends of the device, requiring the formation of two separate external cavities. Such a requirement adds complexity to the ultrashort-pulsed laser system.

The most effective way to utilize an angled facet in a laser diode *intended for the application of short optical pulses*, is to introduce a bend into the waveguide, allowing the incorporation of both an angled and a normal incidence facet in the same structure. An example of such a device, which is currently being explored in our laboratory, is illustrated in Fig. 7.24. The normal incidence facet is located on the absorber section of the laser. The gain section, as identified, contains the large radius bend, providing a change in orientation of the waveguide with respect to the output facet. To further reduce the modal reflectivity, an AR coating would be applied to the angled facet, the optimal design of which is currently under investigation [119].

7.9 Chapter Summary

In this Chapter, the ultrashort-pulsed external-cavity laser system was described. This system utilized the lasers that were designed and fabricated from the InGaAsP/GaAs system, as described in Chapters 2, 4 and 5. An antireflection coating, as described in Chapters 3 and 6 was applied to one of the laser facets to allow efficient coupling of the laser to the external cavity. In combination with the appropriate electrical bias conditions, the above AR coated diode lasers were successfully mode-locked, resulting in the generation of 2 ps pulses with an average power of approximately 1 mW. The tunability of these short pulses was studied, and methods to increase the tunability were proposed and are currently being evaluated.

Chapter 8

Conclusions and Future Work

8.1 Conclusion

In this thesis, the development of a short pulsed external cavity diode laser system has been described. All aspects of the system development, from the MBE growth of the laser materials, to the optimal operating conditions of the laser, have been explored. As was outlined in Chapter 1, the body of this work can be separated into three different themes:

- InGaAsP/GaAs: Material characterization and laser fabrication.
- Antireflection Facet Coatings: Design and fabrication.
- Short-pulse External-cavity Diode Lasers: Design and operation.

InGaAsP/GaAs: Material characterization and laser fabrication

The optimization of the growth of InGaAsP by gas source molecular beam epitaxy has been described, with particular emphasis on the lateral composition modulation that was observed. This LCM which has been studied in detail in the InGaAsP/InP system [11, 15], as well as previously for higher temperature growth techniques of the InGaAsP/GaAs system [120, 121], has been characterized as a function of composition, growth temperature and substrate orientation [81]. In general, it was observed that a reduction in growth temperature resulted in a reduction in the LCM. This was explained by the reduction of

surface mobility which is associated with a reduction in growth temperature. The lower mobilities increased the extent to which the surface species do not reach thermal equilibrium. This effectively results in a weakening of the impact of the thermodynamic driving force which pushes the alloy to phase separation.

An initial investigation of the use of vicinal substrates to reduce the severity of the LCM was performed. This study was based on the above surface mobility discussion and the physical structure of the LCM [81]. The results indicate that growth on type-A surfaces may result in a significant reduction of the LCM, based on the observed reduction of the PL linewidth. Also very promising is the fact that, unlike the case of reduced temperature growths, the reduction in PL linewidth was not associated with a reduction in the PL intensity. As a continuation of the exploratory work described above, experiments are being planned to more thoroughly study and optimize the growth of InGaAsP on vicinal substrates.

In order to effectively design diode lasers, the optical constants (index of refraction) of the materials from which the laser is fabricated must be known at the wavelength at which the laser operates. Since no experimental data was available for the indices of InGaAsP lattice matched to GaAs, a complete characterization as a function of wavelength and material band-gap was performed over the wavelength range from 300 nm to 1600 nm, using a variable angle spectroscopic ellipsometer. The index of refraction for wavelengths where the quaternary layers are transparent was fit using a Sellmeier relationship. This was performed for all samples, ranging in composition from InGaP to GaAs, from which a semi-universal relationship was determined, with the Sellmeier coefficients expressed as a function of material band-gap. With this relationship, the index of refraction at any wavelength where the material is transparent, for a material with a given band-gap can be determined. These results represent the first comprehensive data set published [32] for the

InGaAsP/GaAs material system.

The combination of material growth optimization and the index of refraction characterization allowed the efficient design and fabrication of multiple quantum well lasers suitable for application in the short-pulse external-cavity laser system.

Antireflection Facet Coatings: Design and fabrication

In order to generate ultrashort optical pulses via mode-locking, at repetition rates below approximately 10 GHz, an external cavity is required. Implementation of an external cavity requires the development of high quality antireflection facet coatings, such that feedback from one of the facets can be significantly reduced, and replaced by an external optical element, such as a diffraction grating or a planar mirror. From the perspective of the design and fabrication of these antireflection coatings, the optical constants of the laser waveguide is also required, which provided further motivation for the variable angle spectroscopic ellipsometry analysis.

In Chapter 3, the electron cyclotron resonance chemical vapour deposition system, which was used to deposit the SiO_xN_y layers was described, and the necessary control over the film thickness and index of refraction was illustrated. In Chapters 3 and 6, the process development required for the deposition of high quality antireflection coatings was described. The technique by which the reflectivity of an AR coating is evaluated was outlined, and the method used to design the coating for the specific laser was provided. The use of the measured optical constants of both the laser materials and the SiO_xN_y layers, and the use of the approximate modal reflectivity model [71] resulted in the achievement of facet coatings with reflectivities as low as $1\text{-}2\times10^{-4}$.

Short-pulse External-cavity Diode Lasers: Design and operation

Antireflection coated single and dual electrode diode lasers have been mode-locked in an external cavity, ranging in length from approximately 20 to 40 cm, resulting in repetition

rates in the range of 375 MHz to 750 MHz. Active, passive and hybrid mode-locking has been achieved, with the shortest pulses to date being generated from the hybrid mode-locked dual electrode device. These pulses were approximately 2 ps in duration, with average powers of 1 mW. With the above diode laser system, ultrashort pulses could be achieved over a wavelength range of approximately 17 nm.

Two-photon fluorescence was demonstrated with the above system, indicating that, with further system improvement, these compact mode-locked diode lasers systems may be utilized in next generation TPF laser scanning microscopes.

8.2 Future Work

The work described in this thesis represents the initial stages of development of a compact mode-locked external cavity diode laser, with a potential application to two-photon fluorescence microscopy. With the demonstration of mode-locking and the knowledge gained, it is hoped that this work will be continued, with emphasis on a number of new and exciting possibilities, some of which have been mentioned briefly in previous chapters. In the following sections, a summary of the research areas where work should be continued will be described.

8.2.1 InGaAsP

Although the impact of growth temperature and substrate orientation on the lateral composition modulation of InGaAsP/GaAs has been studied, there is still potential for further improvement in material quality, particularly for implementation in photonic devices. The performance of lasers fabricated from this material system could be improved through the optimization of the growth of the InGaAsP layers and quantum wells, if the particular purpose of each individual layer is considered and is appropriately optimized.

Furthermore, lasers should be fabricated on the various misoriented substrates to

evaluate the potential benefits that the associated reduction in LCM provides. Successful fabrication of laser diodes on these substrates, however, requires a crystal orientation insensitive etching process to define the ridge and allow a direct comparison of device performance. An appropriate electron cyclotron resonance reactive ion etching system was recently commissioned and optimized for etching the GaAs and InGaP ridge structures [1], and will be used to fabricate lasers for this study.

8.2.2 SiO_xN_y Thin Films

With the recent use of angled facet devices for the generation of ultra-short pulses, a study of the optimal coating properties and deposition conditions is necessary. In particular, this analysis should focus on multilayer antireflection coatings with consideration of the requirements of bandwidth and minimum reflectivity, and their impact on device performance.

An additional application of ECR deposited thin films, which would make use of a high index a-Si layer, has been considered and should be explored in detail. As was described in Chapter 5, split contact laser design optimization requires consideration of the optical loss associated with the ridge gap. As has been studied using BPM [122], deposition of 3000 Å of a-Si in the gap can result in a factor of 2 reduction in the loss. The feasibility of this approach warrants investigation.

8.2.3 Laser System Design

Numerous improvements to the laser system are possible, given the flexibility available in the growth and fabrication of InGaAsP/GaAs lasers and the demonstrated facet coating capabilities. Specifically, future system designs should focus on three main areas:

1. Pulse duration

2. Pulse Energy

[1] The details of the application and optimization of an ECR-RIE system to the etching of InGaP and GaAs, as performed by the author, will not be described here.

3. Pulse Wavelength Tunability

Pulse Duration

Provided that the ultrashort pulse is not transform limited, potential exists to reduce the pulse duration through compression. The extent to which the pulse can be compressed is determined by the degree of chirp [2]. Pulse compression is achieved by the intentional introduction of an appropriate delay to the frequencies composing the leading edge of the pulse. This allows the trailing edge to "catch up" to the leading edge, resulting in a net reduction of the pulse width. Compression can be readily accomplished by either a grating or prism pair.

It has been conceived that a large chirp could be impressed on an asymmetric quantum well laser, either during mode-locking with the appropriate rf modulation, or more simply by gain switching. The resultant broad bandwidth pulse may then lend itself to substantial temporal compression, based on the time-bandwidth product. The use of short electrical pulses generated from a step recovery diode are currently being investigated, along with excitation with a sinusoidal waveform, to generate such highly chirped pulses. Compression of these pulses can be performed using a pulse compression system, described previously. The chirp of asymmetric quantum well lasers, under a wide range of bias conditions, is a research area that could be explored and may result in a better understanding of these structures as well as ultimately, shorter pulses.

Pulse Energy

One of the goals of this work is to design and develop a compact system suitable for use in a two-photon fluorescence microscope. Although two-photon fluorescence was demonstrated with the above laser system, significant system development would be necessary before commercial implementation. In particular, increased output powers would be desirable.

[2] Chirp refers to the temporal variation of the wavelength (frequency) within the pulse.

In this wavelength range (800-1000 nm), the most appropriate method to increase the output power involves the use of a semiconductor optical amplifier (SOA). The development of high quality AR coatings and angled facet structures, described in this thesis, makes introduction of an SOA to the short pulse system a very viable option. An appropriate amplifier can be fabricated from the same materials used to make the diode laser, with only minor adjustments to the waveguide configuration. Hence, development work on semiconductor optical amplifiers should be initiated to provide higher output powers from the ultrashort-pulsed external-cavity diode laser system.

Pulse Wavelength Tunability

As was discussed in the last section of Chapter 7, increasing the tunability of the ultrashort pulses can be achieved through the novel combination of the angled facet device with the asymmetric quantum well structure which was described previously [84]. For many applications, wavelength tunability may be a great asset. This experimental work will be continued in our laboratory.

8.3 Summary

In summary, an ultrashort-pulse external-cavity diode laser system has been designed and fabricated, based on an antireflection coated InGaAsP/GaAs diode laser. A number of interesting results have been reported, both on the work leading up to the final construction of such a short pulse system, as well as from operation of the laser system itself. Future research projects based on the development work described here have been discussed, and it is hoped that some of these areas are enthusiastically pursued in the future.

Appendix A

Waveguide and Far Field Analysis

In this appendix, a basic description of two of the waveguide analysis techniques used in this thesis will be described, and the far field pattern which can be determined from the above analysis will be provided.

The first method used to analyze the waveguide properties was based on the effective index method, which has been outlined in a number of different semiconductor device textbooks [123, 124]. In this method, the two dimensional waveguide problem is reduced to two separate one dimensional problems, each of which is readily solved.

In the case of a ridge waveguide laser, as illustrated in Figure A.1 the waveguide solution is first obtained for that region under the ridge, assuming that the waveguide is infinite in the direction in the plane of the epitaxial layers. The same assumption is then applied to the region on either side of the ridge. From these solutions the effective index, n_{eff}, in the three regions is provided, from the relationship

$$n_{eff1} = \frac{\beta_{eff1}}{k_0} \tag{A.1}$$

where β_{eff1} is the propagation constant in region 1, which in this example corresponds to that region under the ridge, and k_0 is the propagation constant in free space.

The solution to the guided wave condition as a result of the ridge is now solved based on an infinite waveguide with a core index of n_{eff1} and cladding index of n_{eff2}. The

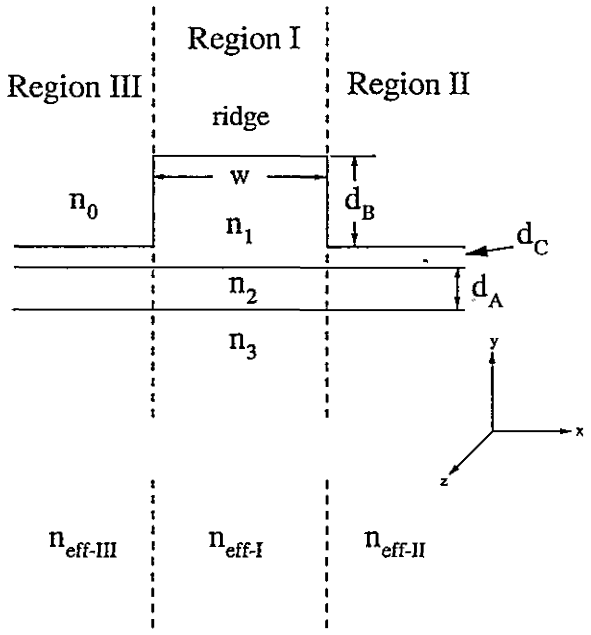

Figure A.1: Waveguide geometry description of the effective index method.

complete waveguide solution is thus obtained.

The solution of the guiding conditions under the ridge and away from the ridge can be determined directly from analytical solutions [125] available for multiple layer structures. Alternatively, a matrix method has been developed [126, 127] which provides a generalized solution to a waveguide composed of an arbitrary number of different layers.

The far field intensity pattern can be easily calculated [128] from the waveguide mode determined above.

Appendix B

Ridge Waveguide Processing Procedure

Wafer Cleaning and Oxide Removal

Trichloroethylene, methanol and deionized water (DI) are used to remove organics from the substrate surface. A mixture of hydrochloric acid (HCL) and DI, and sodium hydroxide (NH_4OH) and DI are used to remove the surface oxide.

Photolithography: Ridge Definition and Etching

Immediately following the oxide removal, a 1000 Å layer of spin on glass (SOG) is applied and is subsequently baked in an oven at approximately 250 °C for 24 hours. Positive photoresist is then applied and developed with the appropriate mask, in the contact photolithography mask aligner, such that those regions which have been exposed to the UV light may be developed and removed. This process is used to define the ridges. The SOG is then removed in a buffered HF solution. The GaAs contact layer is etched using H_2SO_4:H_2O_2:DI (1:8:160) which stops upon reaching the InGaP layer. The InGaP is etched using HCl:H_3PO_4 (1:1), which also terminates upon reaching the GaAs etch stop. The remaining photoresist is removed using acetone and methanol, and the SOG is removed in a buffered HF solution. The sample is then rinsed with DI.

Via Formation

A 1000ÅSiO_2 layer is deposited on the sample surface, which will act as the isolation dielectric. Photoresist is applied and a small stripe on the top of the ridges is exposed and the photoresist and underlying oxide are removed. This feature in the oxide layer is known as the via, and it is the region through which current will be injected into the top of the ridge.

Metallization Patterning

Photoresist is again applied and developed to form the pattern for metallization. The regions where metal is not desired are left with photoresist, which will later be removed, taking the overlying metal layer with it.

Metallization: p-contact

For the top p-contact layer, Ti:Pt:Au layers of 250:500:2400 Å respectively are deposited in an electron beam evaporation system. For the gold deposition, the sample is tilted such that both sides of the ridge receive a uniform layer, ensuring good contact from the contact pad to the ridge.

Lift-off and Thinning

The photoresist and the contact layer on top of it are removed using acetone and methanol. After liftoff, the sample is mounted on a stainless steel holder such that the substrate can be thinned, using a series of carbide paper. The substrates are thinned to approximately 120 μm's.

Metallization: n-contact

The thinned wafers are removed from the sample mount and are cleaned in a series of trichloroethylene, acetone, methanol, isopropyl alcohol and DI. The Ni:Ge:Au (250:500:1200

Å) n-type contact layers are then deposited.

Annealing and Cleaving

The quarter wafer is then annealed in a rapid thermal annealer at 400 °C for 30 s. The sample is then cleaved into the desired laser cavity lengths.

Bibliography

[1] R.N. Hall, G.E. Fenner, J.D. Kingsley, T.J. Soltys and R.O. Carlson, *Phys. Rev. Lett.* **9**, 366 (1962).

[2] N. Holonyak, Jr., S.F. Bevacqua, *Appl. Phys. Lett.* **1**, 82 (1962).

[3] M.I. Nathan, W.P. Dumke, G. Burns, F.H. Dill, Jr,. and G. Lasher, *Appl. Phys. Lett.* **1**, 62 (1962).

[4] T.M. Quist, R.H. Rediker, R.J. Keyes, W.E. Krag, B. Lax, A.L. McWhorter, H.J. Ziegler, *Appl. Phys. Lett.* **1**, 91 (1962).

[5] M.B Panish and H. Temkin, *Gas Source Molecular Beam Epitaxy* (Springer-Verlag, Berlin, Germany, 1993).

[6] K. Onabe, *Jap. J. Appl. Phys.* **21**, 797 (1982).

[7] K. Onabe, *Jap. J. Appl. Phys.* **21**, L323 (1982).

[8] G.B. Stringfellow, *J. Crystal Growth* **58**, 194 (1982).

[9] M. Pessa and H. Asonen, *Optical Engineering* **34**, 2521 (1995).

[10] R. R. LaPierre, Master's thesis, McMaster University, 1992.

[11] R.R. LaPierre, Ph.D. thesis, McMaster University, 1997.

[12] D.B. Williams and C.B. Carter, *Transmission Electron Microscopy: A textbook for materials science* (Plennum Press, New York, USA, 1996).

[13] R.R. LaPierre, D.A. Thompson and B.J. Robinson, *Semicond. Sci. Technol.* **13**, 637 (1998).

[14] H.J. Yi, J. Diaz, B. Lane and M. Razeghi, *Appl. Phys. Lett.* **69**, 2983 (1996).

[15] R.R. LaPierre, T. Okada, B.J. Robinson, D.A. Thompson and G.C. Weatherly, *J. Crystal Growth* **155**, 1 (1995).

[16] Y. Horikoshi, H. Yamaguchi, F. Briones and M. Kawashima, *J. Crystal Growth* **105**, 326 (1990).

[17] G.B. Stringfellow, *J. Crystal Growth* **137**, 212 (1994).

[18] G. Zhang and M. Pessa, *Appl. Surf. Sci.* **75**, 274 (1994).

[19] M.G. Boudreau, M. Boumerzoug, P. Mascher and P.E. Jessop, *Appl. Phys. Lett.* **63**, 3014 (1993).

[20] J.C. Barbour, M.L. Lovejoy, C.I.H. Ashby, A.J. Howard, J.S. Custer and R.J. Shul, *Mat. Res. Soc. Symp. Proc.* **316**, 899 (1994).

[21] M.G. Boudreau, S.G. Wallace, G. Balcaitis, S. Murugkar, H.K. Haugen and P. Mascher, *Appl. Opt.* **39**, 1053 (2000).

[22] S.G. Wallace, Master's thesis, McMaster University, 1996.

[23] M.G. Boudreau, Master's thesis, McMaster University, 1993.

[24] S.R. Walker, J.A. Davies, P. Mascher, S.G. Wallace W.N. Lennard, G.R. Massoumi, R.G. Elliman, T.R. Ophel and H. Timmers, Nucl. Instr. Method. B., in print.

[25] P. Mascher, M.G. Boudreau, S.G. Wallace, S. Murugkar, G. Balcaitis, C. Wettlaufer and H.K. Haugen, *Electrochem. Soc. Proc.* **98-2**, 56 (1998).

[26] R.J. Deri and M.A. Emanuel, *J. Appl. Phys.* **77**, 4667 (1995).

[27] H. Kato, S. Adachi, H. Nakanishi and K. Ohtsuka, *J. Appl. Phys.* **33**, 186 (1994).

[28] S. Adachi, *J. Appl. Phys.* **53**, 5863 (1982).

[29] S. Adachi, *J. Appl. Phys.* **66**, 6030 (1989).

[30] S. Adachi and K. Oe, *J. Appl. Phys.* **54**, 6620 (1983).

[31] H. Burkhard, H.W. Dinges and E. Kuphal, *J. Appl. Phys.* **53**, 655 (1982).

[32] S.G. Wallace, B.J. Robinson, P. Mascher, H.K. Haugen, D.A. Thompson, D. Dalacu and L. Martinu, *Appl. Phys. Lett.* **76**, 2791 (2000).

[33] R.M.A. Azzam and N.M Bashara, *Ellipsometry and Polarized Light* (North-Holland, Amsterdam, 1977).

[34] S. Adachi, *Optical Constants of Crystalline and Amorphous Semiconductors: Materials and Fundamental Principles* (Kluwer Academic, Boston, 1999).

[35] M. Erman, J.B. Theeten, P. Chambon, S.M. Kelso and D.E. Aspnes, *Appl. Phys. Lett.* **56**, 2664 (1984).

[36] G. Harbake, in *Optical Properties of Solids*, edited by F. Abelé (North-Holland, Amsterdam, 1972).

[37] D.E. Aspnes, S.M. Kelso, R.A. Logan and R. Bhat, *J. Appl. Phys.* **60**, 754 (1986).

[38] *WVASE32 User Guide*, J.A. Woolam Co.

[39] C.M. Herzinger, P.G. Snyder, B. Johs and J.A. Woollam, *J. Appl. Phys.* **77**, 1715 (1995).

[40] C.C. Kim, J.W. Garland, H. Abad and P.M. Raccah, *Phys. Rev.* **B45**, 11749 (1992).

[41] C.C. Kim, J.W. Garland and P.M. Raccah, *Phys. Rev.* **B47**, 1876 (1993).

[42] S.H. Wemple and M. DiDomenico, Jr, *Phys. Rev.* **B3**, 1338 (1971).

[43] S. Adachi, *J. Appl. Phys.* **75**, 478 (1994).

[44] B. Broberg and S. Lindgren, *J. Appl. Phys.* **55**, 3376 (1984).

[45] A.R. Forouhi and I. Bloomer, *Phys. Rev.* **B34**, 7018 (1986).

[46] Y. K. H. Tanaka and H. Asahi, *J. Appl. Phys.* **59**, 985 (1986).

[47] M.A. Afromowitz, *Solid State Comm.* **15**, 59 (1974).

[48] S. Zollner, *Appl. Phys. Lett.* **63**, 2523 (1993).

[49] B.R. Bennett, R.A. Soref and J.A. Del Alamo, *IEEE. J. Quantum Electron.* **26**, 113 (1990).

[50] K. Vedam, *Surf. Sci.* **56**, 221 (1976).

[51] M. Moser, C. Geng, E. Lach, I. Queisser, F. Sholz, H. Schweiser and A. Dörnen, *J. Crystal Growth* **124**, 333 (1992).

[52] A.N. Pihktin and A.D. Yak'kov, *Sov. Phys. Semicond.* **12**, 622 (1978).

[53] S. Adachi, *Optical Constants of Crystalline and Amorphous Semiconductors: Numerical Data and Graphical Information* (Kluwer Academic, Boston, 1999).

[54] E.D. Palik, in *Handbook of Optical Constants* (Academic Press, Orlando, 1985).

[55] J.S. Roberts, G.B. Scott and J.P Gowers, *J. Appl. Phys.* **52**, 4018 (1981).

[56] G. Zhang, A. Ovtchinnikov, J. Näappi, K. Smekalin, P. Savolainen, M. Pessa and H. Asonen, *Electron. Lett.* **33**, 89 (1997).

[57] J. Wang, B. Smith, X. Xinqiao and G.T. Burnham, *Appl. Phys. Lett.* **74**, 1525 (1999).

[58] A. Al-Muhanna, L.J. Mawst, D. Boetz, D.Z. Garbuzov, R.U. Martinelli and J.C. Connolly, *Appl. Phys. Lett.* **73**, 1182 (1998).

[59] A. Salakatve and J.L. Nightingale, *CLEO Proc.* 241 (2000).

[60] G. Zhang, J. Näppi, K. Vanttinen, H. Asonen and M. Pessa, *Appl. Phys. Lett.* **61**, 96 (1992).

[61] L.J. Mawst, A. Battacharya, J. Lopez, D. Boetz, D.Z. Garbuzov, L. DeMarco, J.C. Connolly, M. Jansen, F. Fang and R.F. Nabiev, *Appl. Phys. Lett.* **69**, 1532 (1996).

[62] T.W. Lee, P.A. Houston, R. Kumar, X.F. Yang, C. Hill, M. Hopkinson and P.A. Claxton, *Appl. Phys. Lett.* **60**, 474 (1992).

[63] Y.J. Chan, D. Pavlidis, M. Razeghi and F. Omnes, *IEEE. Trans. Electron. Dev.* **37**, 2141 (1990).

[64] C. Cai, M.I. Nathan and T.H. Lim, *Appl. Phys. Lett.* **74**, 720 (1999).

[65] G. Zhang, A. Ovtchinnikov, J. Näppi, H. Asonen and M. Pessa, *IEEE. J. Quantum Electron.* **29**, 1943 (1993).

[66] H.J. Yi, J. Diaz, L.J. Wang, I. Eliashevich, S. Kim, R. Williams, M. Erdtmann, X. He, E. Kolev and M. Razeghi, *Appl. Phys. Lett.* **66**, 3251 (1995).

[67] P. Savolainen, M. Toivonen, H. Asonen, M. Pessa and R. Murison, *IEEE. Photon. Technol. Lett.* **8**, 986 (1996).

[68] N. Matsumoto and K. Kumabe, *Jap. J. Appl. Phys.* **18**, 321 (1979).

[69] B.W. Hakki and T.L. Paoli, *J. Appl. Phys.* **46**, 1299 (1975).

[70] D.T. Cassidy, *J. Appl. Phys.* **56**, 3096 (1984).

[71] C. Vassallo, *Electron. Lett.* **21**, 333 (1985).

[72] C. Vassallo, *Electron. Lett.* **24**, 62 (1988).

[73] C. Vassallo, *J. Opt. Soc. Am. A* **5**, 1918 (1988).

[74] J. Lee, T. Tanaka, S. Sasaki, S. Uchiyama, M. Tsuchiya and T. Kamiya, *J. Light. Technol.* **16**, 884 (1998).

[75] G. Eisenstein, *ATT Bell. Lab Tech. Journ.* **63**, 357 (1984).

[76] T. Saitoh, T. Mukai and O. Mikami, *J. Light. Technol.* **3**, 288 (1985).

[77] M.G. Boudreau, Ph.D. thesis, McMaster University, 1997.

[78] D.M. Braun and R.L. Jungerman, *Optics. Lett.* **20**, 1154 (1995).

[79] G. Eisenstein and L.W. Stulz, *Appl. Opt.* **23**, 161 (1984).

[80] I.P. Kaminow, G. Eisenstein and L.W. Stulz, *IEEE. J. Quantum Electron.* **19**, 493 (1983).

[81] S.G. Wallace, B.J. Robinson, P. Mascher, H.K. Haugen, D.A. Thompson, D. Dalacu and L. Martinu, Conference on Lasers and Electro-Optics (CLEO), May 2000, paper #CWK33.

[82] J.E. Fouquet, D.M. Braun and G.R. Trott, *IEEE. J. Quantum Electron.* **32**, 1777 (1996).

[83] D. Wandt, M. Laschek and A. Tünnermann, *Optics. Lett.* **22**, 390 (1997).

[84] S.G. Wallace, M.J. Brennan, H.K. Haugen and P. Mascher, Conference on Lasers and Electro-Optics (CLEO), May 2000, paper #CTuA61.

[85] B-L Lee and C-F Lin, *IEEE. Photon. Technol. Lett.* **10**, 322 (1998).

[86] H.S. Gingrich, S.R. Chumney, S-Z. Sun, S.D. Hersee, L.F. Lester and S.R.J. Brueck, *IEEE. Photon. Technol. Lett.* **9**, 155 (1997).

[87] X. Zhu, D.T. Cassidy, M.J. Hamp, D.A Thompson, B.J. Robinson, Q.C. Zhao and M. Davies, *IEEE. Photon. Technol. Lett.* **9**, 1202 (1997).

[88] Y. Silberberg, P.W. Smith, D.J. Eilenberger, D.A.B. Miller, A.C. Gossard and W. Wiegmann, *Optics. Lett.* **9**, 507 (1984).

[89] J.P Van der Ziel, R.A. Logan and W.M. Mikulyak, *Appl. Phys. Lett.* **39**, 867 (1981).

[90] Y. Arakawa, A. Larsson, J. Paslaski and A. Yariv, *Appl. Phys. Lett.* **48**, 561 (1986).

[91] H. Ito, N. Onodera, K. Gen-Ei and H. Inaba, *Electron. Lett.* **17**, 15 (1981).

[92] P.P Vasil'ev and I.S. Goldobin, *Sov. J. Quantum Electron.* **17**, 835 (1987).

[93] P.P Vasil'ev and I.S. Goldobin, *Sov. J. Quantum Electron.* **18**, 1519 (1988).

[94] D. Bimberg, K. Ketterer, H.E. Schöll and H.P Vollmer, *Electron. Lett.* **20**, 343 (1984).

[95] K.A. Ahmed, B.J. Eggleton, H-F. Liu, P.A. Krug and F. Oullette, *IEEE. Photon. Technol. Lett.* **7**, 158 (1995).

[96] J. AuYeung, *Appl. Phys. Lett.* **38**, 308 (1981).

[97] A. Galvanauskas, P. Blixt, J.A. Tellefsen, Jr., *Appl. Phys. Lett.* **63**, 1742 (1993).

[98] H.A. Haus, *IEEE. J. Quantum Electron.* **11**, 736 (1975).

[99] H.A. Haus, *J. Appl. Phys.* **46**, 3049 (1975).

[100] D.J. Derickson, R.J. Helkey, A. Mar, J.R. Karin, J.G. Wasserbauer and J.E. Bowers, *IEEE. J. Quantum Electron.* **28**, 2186 (1992).

[101] J.P Van der Ziel, W.T. Tsang, R.A. Logan, R.M. Mikylyak and W.M. Augustyniak, *Appl. Phys. Lett.* **39**, 525 (1981).

[102] M.C. Wu, Y.K. Chen, T. Tanbun-Ek, R.A. Logan, M.A. Chin and G. Raybon, *Appl. Phys. Lett.* **57**, 759 (1990).

[103] Y.K. Chen, M.C. Wu, T. Tanbun-Ek, R.A. Logan and M.A. Chin, *Appl. Phys. Lett.* **58**, 1253 (1991).

[104] P.J. Delfyett, L.T. Florez, N. Stoffel, T. Gmitter, N.C. Andreadakis, Y. Silberberg, J.P. Heritage and G.A. Alphonse, *IEEE. J. Quantum Electron.* **28**, 2203 (1992).

[105] J.E. Bowers, P.A. Morton, A. Mar and S.W. Corzine, *IEEE. J. Quantum Electron.* **25**, 426 (1989).

[106] J.P. Curtis and J.E. Carroll, *Int. J. Electronics* **60**, 87 (1986).

[107] K. N. Choi and H.F. Taylor, *Appl. Phys. Lett.* **62**, 1875 (1993).

[108] K.L. Sala, G.A. Kenney-Wallace and G.E. Hall, *IEEE. J. Quantum Electron.* **16**, 990 (1980).

[109] D.J. Bradley and G.H.C. New, *Proc. IEEE* **62**, 313 (1974).

[110] A.G. Weber, E.H. Böttcher and D. Bimberg, *Appl. Phys. Lett.* **55**, 1600 (1989).

[111] H. Ito, H. Yokoyama, S. Murata and H. Inaba, *IEEE. J. Quantum Electron.* **17**, 663 (1981).

[112] A. Lago, A.T. Obeidat, A.E. Kaplan, J.B. Khurgin, P.L. Shkolnikov and M.D. Stern, *Optics. Lett.* **20**, 2054 (1995).

[113] C. Xu and W.W. Webb, *J. Opt. Soc. Am. B* **13**, 481 (1996).

[114] D.W. Piston, M.S. Kirby, H. CHeng, W.J. Lederer and W.W. Webb, *Appl. Opt.* **33**, 662 (1994).

[115] W. Denk, J.H. Strickler and W.W. Webb, *Science* **248**, 73 (1990).

[116] A.J. Collar, G.D. enshall, J. Farré, B. Mikkelsen, Z. Wang, L. Eskildsen, D. Olesen and K.E. Stubkjaer, *IEEE. Photon. Technol. Lett.* **2**, 553 (1990).

[117] M.C. Farries, J. Buus and D.J. Robbins, *Electron. Lett.* **26**, 381 (1990).

[118] B-L Lee and C-F Lin, *IEEE. Photon. Technol. Lett.* **12**, 618 (2000).

[119] A theoretical and experimental investigation of optimized coatings for angled facet devices is being conducted by M. Brennan as a component of his PhD research.

[120] N. Kuwano, K. Fukada, K. Oki, S. Tanaka, K. Hiramatsu and I. Akasaki, *J. Crystal Growth* **98**, 82 (1989).

[121] M. Kondo, S. Shirakata, T. Nishino and Y. Hamakawa, *J. Appl. Phys.* **60**, 3539 (1986).

[122] Matt Pearson, Personal communication.

[123] G.P. Agrawal and N.K. Dutta, *Long Wavelength Semiconductor Lasers* (Van Nostrand Reinhold, New York, 1993).

[124] S.L. Chuang, *Physics of Optoelectronic Devices* (Wiley, New York, 1995).

[125] H. Kawaguchi and T. Kawakami, *IEEE. J. Quantum Electron.* **13**, 556 (1977).

[126] L.M. Walpita, *J. Opt. Soc. Am. A* **2**, 595 (1985).

[127] M.J. Brennan, matrix method waveguide analysis code.

[128] X. Zeng and A. Nagwi, *Appl. Opt.* **32**, 4491 (1993).